University of Sheffield

High-throughput Simulations of Metal Organic Frameworks (MOFs) for CO_2 Capture

Rama Oktavian

Supervisor: Dr. Peyman Z. Moghadam

Co-Supervisor: Prof. Joan Cordiner

A thesis submitted in partial fulfilment of the requirements for the degree of Doctor of Philosophy

Department of Chemical and Biological Engineering

University of Sheffield

May 2024

Declaration

I, the author, confirm that the contents of this document are solely my own, with the exception of any jointly produced publications that may have been included. The authors' contribution to each of the works has been clearly acknowledged below. I hereby verify that the appropriate credit has been provided in this statement wherever the work of others has been referenced.

All passages or sentences quoted in this text from external sources have been explicitly acknowledged by clear cross-referencing to the author, work, and page(s). All illustrations in this report that were not created by the author have been included with clear permission from the original creator and are duly credited. I comprehend that neglecting to adhere to this requirement constitutes plagiarism and will be regarded as a basis for failure. This report has not been previously for an award at this, or any other, university. I am aware of the university guidance on the use of unfair means.

Name : Rama Oktavian

Date : 17 May 2024

Abstract

Metal-organic frameworks (MOFs), composed of metallic nodes that are linked together by organic linkers, have gained considerable attention as a type of nano-porous materials in the past three decades. MOFs are highly appealing for their potential in various applications, such as gas storage and separations owing to their high porosity and adjustable surface properties. Nevertheless, finding the most suitable MOFs for industrially relevant gas adsorption and separation processes is challenging due to the vast number of possible combinations of inorganic and organic building units, which result in hundreds of thousands of different MOFs. With this large number of structures, it is critical to develop computational protocols to rapidly and efficiently screen databases of MOFs for energy applications such as CO_2 capture or hydrogen storage.

Firstly, to validate the computational methods and models used, this thesis presents computational geometric properties and CO_2 uptake characterisation of Zirconium-based MOFs. We perform systematic periodic density functional theory (DFT) calculations comparing 25 different combinations of basis sets and functionals to calculate framework partial atomic charges. We then compare simulation results with published experimental data for CO_2 adsorption isotherms, and demonstrate the good agreement between simulated and experimental data. We then use 102 structures containing Zr-oxide secondary building units (SBUs) extracted from the Cambridge Structural Database (CSD) MOF subset to perform high-throughput adsorption simulations and identify top candidates for post-combustion CO_2 capture.

The second focus of this thesis is on the use of simulations to explain the remarkable CALF-20 properties to capture CO_2 from flue gas, while maintaining stability and resisting water. Here, we employ atomistic-level simulations and experiments to investigate the adsorptive characteristics of CALF-20 and gain insights into its flexible crystal structure. We analyse and compare CO_2 and water adsorption isotherms, and elucidate the significance of water-framework interactions and hydrogen bonding networks in CALF-20's hydrophobic properties. In addition, we conduct molecular dynamics simulations using both density-functional theory (DFT) and machine learning potentials (MLPs) trained to DFT energies and forces. The simulations reveal the impact of adsorption-induced flexibility in CALF-20.

Lastly, through a collaborative work with our industrial collaborator, a multi-scale computational strategy that includes DFT and grand canonical Monte Carlo (GCMC)

simulations is established. This strategy develops a systematic high-throughput computational screening to explore The Quantum MOF (QMOF) database and the Computation-Ready, Experimental (CoRE) MOF database for selective adsorption of CO_2 from a wet flue gas mixture. The screening protocol effectively reveal several interesting MOFs that exhibit selectivity towards CO_2 in the presence of water vapor. By establishing a tight feedback loop between simulations, and experiments performed by our industrial collaborator, we are able to effectively synthesise and evaluate several MOFs with relatively high stability in the laboratory setting. This process confirms the validity of our technique in selecting exceptional MOFs for the purpose of CO_2 capture.

Acknowledgements

I believe that all the work reported in my thesis are only made possible thanks to the help from positive and supportive people. I am grateful to everyone who has stepped into my life that helped me reach this stage of my PhD journey. Their presence has indeed always motivated me to achieve my goals and have been making my days' worth living.

First and foremost, my big gratitude and thanks goes to my principal supervisor, Dr. Peyman Z. Moghadam, for his supportive and motivating guidance throughout the last four years of my PhD journey. I would like to thank for his enthusiastic and encouraging supervisory process to my research from the big picture into technical details. His often demanding and rigorous evaluation process to my technical research and writing has molded me into the skilled and diligent writer I believe I have become. Although it was a bit painful looking at the bright red text in the document, at the end it was rewarding to me where he guided me to produce such high quality doctoral publications in some of the top and world class journals in our field. Furthermore, I had great opportunity and valuable experience to work together with industrial collaborators in some of the most challenging and yet exciting projects. Thanks for the push that could make me achieve and maintain a level of quality that he expected from me.

I must also thank Professor Joan Cordiner for taking over my PhD supervisory role at the university after Peyman moved to University College London. Her encouragement and caring makes me believe that I could end this journey with pride. Under her guidance, I feel a warm welcome and support from her. She has been a very kind-hearted and supported me to every decision I took during my final PhD year.

A special mention I should address to everyone at the Centre for Computational Materials Discovery, or as we call it the "PZM club" for always being passionate, motivated and supportive in my entire PhD studentship. From the first day of my PhD, Federica Zanca was extremely welcoming, supportive, and helpful. Special thanks to her that was always available to support me and being the greatest "partner in crime" ever for working on our collaborative projects. I believe that her presence and support made my PhD possible. Guanming Huang, with whom I spent my first year of PhD, has consistently helped me a lot to go through the most critical times supporting me a lot setting up the codes I needed in the first year of my study. I could not say more thanks to Lawson Taylor Glasby who has been always encouraging me and sat next to me to help me adapting well with the British culture. I truly enjoyed discussing both academic and non-academic matters with him including papers and English

football. I always felt so grateful when Peyman assigned me to work together with Lawson due to his hard working mindset and his dedication. Despite the fact that I may not have worked closely with Chenhao Li, simply a simple wave or hello from him had always brightened my day and brought a positive impact in my daily life.

I must thank to the entire Department of Chemical and Biological Engineering, University of Sheffield for all the supporting facilities available to me. In particular, I would like to say special thanks to Dr. Eleni Routoula for her excellent service as PGR tutor and to Nicola Basher, the former Finance Cluster Manager of Department who helped me for the financial terms in attending international conferences or workshops.

To all of my PhD mates, Maheen Rana, Ludovica Luongo, Anna Leathard, Robert Douglas, Sebastian Ross, Paul Coombes, Jack Atkinson, Matt and Rosie, thanks for your time that we spent around together at the shared office. With all of you, I feel my PhD study more colorful and joyful because you were always there when I wanted to moan and laugh.

Outside the academia, a big thanks should go to "Bapak – Bapak Broomhall club" (mas Joko Purwanto, Mas Khaerul Rijal, Mas Defari Rohandi, Pak Idham Effendi et al.) who sometimes invited me for a cup of coffee or having a chit chat time, that could drag me away from stressful situations.

It would be a big mistake from me if I did not say big thanks to Indonesian Endowment Fund (LPDP) that provided me a generous funding for my PhD study. I could not imagine how my PhD study would go without LPDP in terms of financial status. LPDP supported everything for the tuition fees for the entire study period to living allowance and other financial supports that enabled me to attend and visit countries outside the UK for academic conferences and workshops.

Finally, I would like to wrap up by saying huge thanks to my family for their ultimate and immeasurable support. For my beloved wife, Titis Dwi Aryati, thanks for her understanding and patience, and for always being there for me, and keeping our commitment and taking care of our beloved daughter, Ammara Senja Meifani Putri Rama while I was away studying. Both of you are my true motivation for undertaking and finishing my PhD. I could not have made it here successfully without you by my side.

Table of Contents

List of Tables

List of Figures

1. Introduction

1.1. Background

Carbon dioxide emission that is primarily come from the combustion of fossil fuel is one of major environmental issue has to address. The significant increase of CO_2 emission has been continually estimated to surpass 500 parts per million by 2050[1] leading to the world's issues on the massive energy requirement associated with fossil fuels. Carbon capture, utilization and storage (CCUS) scheme is a good option to address the CO_2 emission from industrial processes[2]. This technology involves capturing CO_2 at emission source and transporting for storage or conversion to other chemicals[3] and around 40 Mt of CO_2 is captured and stored today with CCUS.[4] Currently, the conventional aqueous ammonia scrubbing is the most mature and widely used technology for CO_2 capture,[5] despite a number of limitations, such as equipment corrosion, high energy loss, and thermal decay of the amine during regeneration. In contrast, adsorption using feed-specific adsorbents is considered as a viable alternative technique for CO_2 capture due to its high energy efficiency and straightforward regeneration procedure.[6] Various porous materials, such as activated carbon and zeolites have been investigated for CO_2 capture.[7–11] However, they remain limited in practical use due to several drawbacks including low CO_2 selectivity, competition adsorption with water and other contaminants, poor structural tenability, and scalability.[12]

Metal-organic frameworks (MOFs) have received significant interest from the scientific community since their emergence a few decades ago.[13–15] MOFs are porous crystalline structures consisting of metal clusters interconnected by organic linkers. Because of their hybrid crystalline and porous structure, which makes them tailorable, these materials show great potential for various applications, such as gas adsorption and separation process, including CO_2 capture.[16–20] Compared to other conventional materials, such as zeolites and activated carbon, MOFs have been extensively studied for CO_2 capture and utilization.[18,21–23] This is due to the exceptional features of MOFs, including stable open-frame structure, high porosity and their large specific surface area. The high specific surface area of MOFs exhibits selective adsorption towards some particular gas molecules, and their porosity can be finely tuned by changing the metal and organic linkers.[24,25] The number of reported MOF materials has significantly increased in the past decade owing to their synthetic flexibility. This is because it is theoretically possible to synthesize an unlimited number of MOFs by utilizing various degrees of freedom offered by different linkers, functional groups, metal nodes,

defects, and other factors.[26] To date, more than 100,000 MOFs have been experimentally synthesized and recorded by the Cambridge Crystallographic Data Centre (CCDC) which collates and curates the Cambridge Structural Database (CSD).[27]

The nature of MOFs has been a topic of intense discussion for several years due to their significant research and widespread interest. Over the years, various research groups have developed distinct MOF databases using hypothetical or experimental materials and sophisticated algorithms to explore the range of applications for MOFs.[28] Figure 1 summarizes the development of both hypothetical and experimental MOF databases.

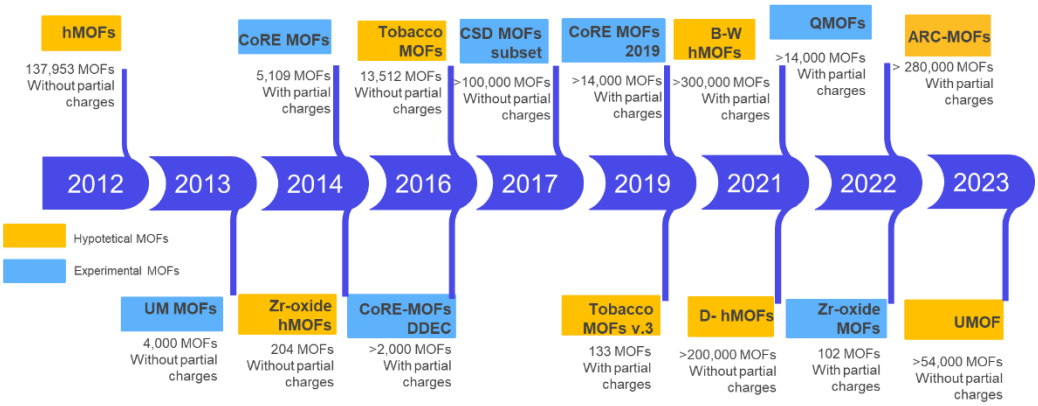

Figure 1.1. The timeline summary of MOF databases (2012 – present)

In 2012, the first hypothetical MOFs containing 137,000 MOFs was successfully developed by Wilmer and coworkers.[29] Subsequently, in 2013 Goldsmith, et al.[30] constructed 4,000 experimental MOF database with nontrivial internal porosity and surface areas between 3100 and 4800 m^2/g for hydrogen storage. Gomez-Gualdron et al.[31] performed computational study to generate Zr-MOF database for volumetric methane storage in 2014. They demonstrated that Zr-MOFs with **ftw** topology exhibited superior performance compared to Zr-MOFs with **scu** and **csq** topologies for storing methane. The Computation-Ready Experimental (CoRE) MOF database, created in 2014, is a smaller but more widely used database consisting of approximately 5000 MOFs[32]. It was then followed by Nazarian et al.[33] in 2016 creating "CoRE MOF 2014-DDEC" database where the DFT-derived partial atomic charges was calculated for ~2,900 MOFs. One notable feature of this database is the inclusion of DFT-derived charges, which enhances the accuracy of GCMC simulations when modeling the adsorption of molecules with significant electrostatic interactions, such as CO_2. The CoRE 2014 database has recently been extended to approximately 14,000 MOFs obtained from the CSD (CoRE

2019 database).[34] It currently stands as the most extensively used database of experimentally characterized porous MOF for high-throughput screening gas adsorption application.[35]

In 2017, a new computational algorithm was developed to generate MOFs with pre-defined topologies by Colon et al.[36] The software, called ToBaCCO, consists of 13,512 hypothetical MOFs with 41 different topologies. This MOF database was evaluated for hydrogen and methane storage, and the separation of xenon/krypton mixtures. The new version of the ToBaCCO code introduces a crystallographic net rescaling algorithm (ToBaCCo 3.0). This approach enables the automatic building of MOFs with any desired topology by utilizing principles from the graph theory. In 2017, CCDC compiled a distinct database known as the CSD MOF subset, which exclusively contains all MOF-like structures synthesised so far. Moghadam et al.[27] later developed an automated screening approach employing the CSD Python API to quickly detect newly synthesised MOFs added to the CSD. For the purpose of identifying high-performing materials, it is more advantageous to use databases that consist of experimentally created MOFs, such as the CoRE and the CSD MOF databases. These databases are preferable because they contain structures that can be feasibly synthesised, once they are identified on the computer. The QMOF database[38,39] was recently established, comprising a subset of 15,713 materials from the aforementioned databases which ultimately serve as a suitable "DFT-ready" dataset of MOFs.

Given the huge number of MOFs, depending solely on experimental testing to discover a novel material with exceptional performance is practically finding a needle in a haystack, which necessitates numerous cycles of experiments which incurs substantial research operational expenses. To fully exploit the potential of MOFs, it is imperative to design and synthesise MOFs with the desired structural and chemical properties. One viable approach is to employ computational methods to predict the performance of MOFs prior to experimental synthesis. In this regard, the application of high-throughput computational screening (HTCS) of MOFs at different process conditions could accelerate the discovery of MOFs that exhibit superior adsorption performances,[40–42] thereby providing guidance that is difficult or not often accessible in experimental efforts.[43] In the context of gas adsorption in MOFs, HTCS can be combined with experimental methods to provide useful information including adsorption isotherms, favourable adsorption sites, guest-host interaction energies as well as the selectivity for multicomponent gas mixtures. While a considerable number of MOFs have undergone experimental testing for CO_2 separation process,[44,45] many more have also reported computational studies to screen MOFs for CO_2 capture. For example, Snurr and co-workers conducted simulations to study the adsorption process of pure CO_2, N_2, and CH_4 for 137,953

hypothetical MOFs (hMOFs).[46] They also suggested a correlation between structural properties for evaluating the effectiveness of adsorbents in separating CO_2/CH_4 and CO_2/N_2 and identified the top-performing structures before synthesis and testing.[47] In another work, Qiao et al. screened 4,764 computation-ready experimental (CoRE)-MOFs to evaluate their effectiveness in separating CO_2/CH_4 and CO_2/N_2.[40] They developed quantitative correlations between the type of metal used and the evaluation criteria for the adsorbents studied. Additionally, they screened hydrophobic MOFs to assess their suitability for the separation of H_2S and CO_2 from natural gas.[40]

However, for industrial CO_2 capture application, H_2O usually presents causing co-adsorption and detrimental effect on the efficiency of gas separation process. Thus, developing materials with the ability to withstand with water and selectively adsorb CO_2 is becoming a topic interest for industry. Therefore, there exist a motivation for evaluating and establishing performance index or metrics for the domain of materials for CO_2 capture in the presence of water vapour, including materials stability. Assessment process for identifying top performance materials for CO_2 capture should include some industrial represented key evaluation metrics that might not be considered for common HCTS method.[49,50] Integrating the prediction of materials stability into the screening process should also be performed to successfully assess materials for industrial implementation as chemical industry is dealing with harsh condition.[51,52] While HTCS could suggest best materials for selective CO_2 capture, it sometimes fail to meet industrial criteria for synthesizability.[53] An advancement to HTCS indeed require a thorough computational screening and molecular modeling strategy for MOFs incorporating the experimental and testing at industrially relevant process condition, which remains an ongoing research area. The protocol could also include an establishment of a rigorous feedback loop between screening process and experimental testing in industry.

1.2. Thesis objectives and outlines

In this thesis, we develop systematic and efficient high throughput computational screening protocols for the discovery and identification of promising hypothetical and already-synthesised MOFs for CO_2 capture. Our protocols take into account post-combustion CO_2 capture operating conditions using grand canonical Monte Carlo (GCMC) simulations. Structure-property relationships are also derived to identify key structural and chemical features of materials that provide the optimum adsorption performance, and to guide experimental synthesis and testing of promising MOF adsorbents.

As a complement to our work, following the screening process, this thesis also provides in-depth analysis, from molecular-level point of view, the analysis of gas molecules adsorption sites and interactions with framework atoms. Structural flexibility analysis from experimental and simulation perspectives using molecular dynamics are also presented.

The thesis is organised as follows. In Chapter 2, we provide theoretical background of the computational studies used in this thesis including the geometric analysis and GCMC simulations to determine the amount of gas uptake in MOFs.

In Chapter 3, we perform high throughput computational screening for MOFs containing Zr-oxide secondary building units (SBU). These materials are shown to have great gas adsorption properties combined with high mechanical, thermal, and chemical stability. We successfully characterise CO_2 adsorption performance of this family of MOFs via high-throughput GCMC simulations, along with thorough investigations of their topological and geometrical features.

In Chapter 4, we study the adsorptive properties of CALF-20 by combining atomistic-level simulations with experiments to explore CALF-20's structural flexibility. We also report a comparison between experimentally measured and simulated CO_2 and water adsorption isotherms. This study explains CALF-20's hydrophobic behaviour by providing atomistic analysis on the role of water-framework interactions and hydrogen bonding network in CALF-20. In this Chapter, the structural flexibility analysis is also performed using regular and enhanced sampling molecular dynamics simulations with both density-functional theory (DFT) and machine learning potentials (MLPs) trained to DFT energies and forces followed by experimental PXRD analysis.

In Chapter 5, we outline computational screening protocols for post-combustion CO_2 capture in the presence of humidity for databases containing large number of MOFs. In particular, we explore The Quantum MOF (QMOF) database and the CoRE MOF database for selective adsorption of CO_2 from a wet flue gas mixture. After the screening, we identified a number of promising MOFs that exhibit high CO_2 selectivity against water. Here, we demonstrate how a tight feedback loop between simulations and experiments performed by our industrial collaborator can guide synthetic efforts towards outstanding materials.

Finally, in Chapter 6, the summary for each Chapter is presented and discussed. A research outlook and future directions for this research field are also discussed.

1.3. Publications

Part Some of the Chapters of this thesis have been already published in the following publications and conference presentations:

Publications

1. (Balzer et al., 2020) Balzer C., Oktavian R., Zandi M., Fairen-Jimenez D., Moghadam P. Z. (2020). Wiz: A web-based tool for interactive visualization of big data. Patterns, 1, 8, 100107. https://doi.org/10.1016/j.patter.2020.100107.
2. (Oktavian et al., 2022) Oktavian R., Schireman R., Glasby L. T., Huang G., Zanca F., Fairen-Jimenez D., Ruggiero M. T., & Moghadam P. Z. (2022). Computational characterization of Zr-oxide MOFs for adsorption applications. ACS Applied Materials & Interfaces, 14, 51, 56938-56947. https://doi.org/10.1021/acsami.2c13391.
3. Oktavian R., Goeminne R., Glasby L. T., Song P., Huynh R., Taheri-Qazvini O., Ghaffari-Nik O., Masoumifard N., Cordiner, J., Hovington P., Van Speybroeck V., & Moghadam P. Z. (2024). Gas adsorption and framework flexibility of CALF-20 explored via experiments and simulations. [Manuscript accepted in Nature Communications].
4. Oktavian R., Song P., Huynh. R., Qazvini O.T., Masoumifard N., Hovington, P., Moghadam P.Z. (2024). High Throughput Screening (HTS) on Metal Organic Frameworks (MOFs) for CO_2 capture with the presence of humidity: Computational and experimental work. [Manuscript in preparation for submission].
5. (Glasby et al., 2023) Glasby L. T., Oktavian R., Zhu K., Cordiner J. L., Cole J. C., & Moghadam P. Z. (2023). Augmented reality for enhanced visualisation of MOF adsorbents. Journal of Chemical Information and Modeling, 63, 19, 5950-5955. https://doi.org/10.1021/acs.jcim.3c01190.
6. (Glasby et al., 2023) Glasby L. T., Gubsch K., Bence R., Oktavian R., Isoko K., Moosavi S. M., Cordiner J. L., Cole J. C., & Moghadam P. Z. (2023). DigiMOF: A database of metal-organic framework synthesis information generated via text mining. Chemistry of Materials, 35, 11, 4510-4524. https://doi.org/10.1021/acs.chemmater.3c00788.

Conference presentations

1. 8th Conference of the Federation of European Zeolite Associations, UK, July 2021, Oral Presentation "*Computational Characterisation and Screening of Zr-Oxide Metal Organic Frameworks for CO_2 Capture*", R. Oktavian and P. Z. Moghadam.

2. Fundamental of Adsorption, 14th International Conference, Colorado, USA, May 2022, Poster Presentation "*Experimental and Computational Characterization of CALF-20+ Active Materials for CO_2 Capture from Flue Gas.*", R. Oktavian, F. Zanca, O. G. Nik, P. Song and P. Z. Moghadam.
3. 1st Mediterranean Conference on Porous Materials, Crete, Greece, May 2023, Poster Presentation "*Computational Characterisation and Screening of Metal Organic Frameworks for CO_2 Capture in the Presence of Humidity",* R. Oktavian, F. Zanca, L. T. Glasby, P. Song, O. T. Qazvini and P. Z. Moghadam.
4. 6th Annual UK Porous Materials Conference, Sheffield, UK, June 2023, Oral Presentation "*Computational Characterization of Zr-Oxide MOFs for Gas Adsorption Applications*", R. Oktavian and P. Z. Moghadam
5. 5th European Conference on Metal Organic Frameworks and Porous Polymers (EuroMOF2023), Oral Presentation "*Computational Characterisation and Screening of Metal Organic Frameworks for CO_2 Capture in the Presence of Humidity*", R. Oktavian, F. Zanca, L. T. Glasby, O. T. Qazvini, P. Song and P. Z. Moghadam.

References

(1) Agency, I. E. Carbon Capture and Storage and the London Protocol. **2011**. https://doi.org/https://doi.org/https://doi.org/10.1787/5kg3n27pfv30-en.

(2) Leung, D. Y. C.; Caramanna, G.; Maroto-Valer, M. M. An Overview of Current Status of Carbon Dioxide Capture and Storage Technologies. *Renew. Sustain. Energy Rev.* **2014**, *39*, 426–443. https://doi.org/https://doi.org/10.1016/j.rser.2014.07.093.

(3) Fu, L.; Ren, Z.; Si, W.; Ma, Q.; Huang, W.; Liao, K.; Huang, Z.; Wang, Y.; Li, J.; Xu, P. Research Progress on CO_2 Capture and Utilization Technology. *J. CO_2 Util.* **2022**, *66*, 102260. https://doi.org/https://doi.org/10.1016/j.jcou.2022.102260.

(4) Agency, I. E. *Net Zero by 2050*; Paris, 2021.

(5) Wang, F.; Zhao, J.; Miao, H.; Zhao, J.; Zhang, H.; Yuan, J.; Yan, J. Current Status and Challenges of the Ammonia Escape Inhibition Technologies in Ammonia-Based CO_2 Capture Process. *Appl. Energy* **2018**, *230*, 734–749. https://doi.org/https://doi.org/10.1016/j.apenergy.2018.08.116.

(6) Hussin, F.; Aroua, M. K. Recent Trends in the Development of Adsorption Technologies for Carbon Dioxide Capture: A Brief Literature and Patent Reviews (2014–2018). *J. Clean. Prod.* **2020**, *253*, 119707. https://doi.org/https://doi.org/10.1016/j.jclepro.2019.119707.

(7) Sneddon, G.; Greenaway, A.; Yiu, H. H. P. The Potential Applications of Nanoporous Materials for the Adsorption, Separation, and Catalytic Conversion of Carbon Dioxide. *Adv. Energy Mater.* **2014**, *4* (10), 1301873. https://doi.org/https://doi.org/10.1002/aenm.201301873.

(8) Abd, A. A.; Othman, M. R.; Kim, J. A Review on Application of Activated Carbons for Carbon Dioxide Capture: Present Performance, Preparation, and Surface Modification for Further Improvement. *Environ. Sci. Pollut. Res.* **2021**, *28* (32), 43329–43364. https://doi.org/10.1007/s11356-021-15121-9.

(9) Belmabkhout, Y.; Guillerm, V.; Eddaoudi, M. Low Concentration CO_2 Capture Using Physical Adsorbents: Are Metal–Organic Frameworks Becoming the New Benchmark Materials? *Chem. Eng. J.* **2016**, *296*, 386–397. https://doi.org/10.1016/j.cej.2016.03.124.

(10) Lee, S.-Y.; Park, S.-J. A Review on Solid Adsorbents for Carbon Dioxide Capture. *J. Ind. Eng. Chem.* **2015**, *23*, 1–11. https://doi.org/10.1016/j.jiec.2014.09.001.

(11) Li, Y.; Li, L.; Yu, J. Applications of Zeolites in Sustainable Chemistry. *Chem* **2017**, *3* (6), 928–949. https://doi.org/10.1016/j.chempr.2017.10.009.

(12) Gebremariam, S. K.; Dumée, L. F.; Llewellyn, P. L.; AlWahedi, Y. F.; Karanikolos, G. N. Metal-Organic Framework Hybrid Adsorbents for Carbon Capture – A Review. *J. Environ. Chem. Eng.* **2023**, *11* (2), 109291. https://doi.org/https://doi.org/10.1016/j.jece.2023.109291.

(13) Chakraborty, D.; Yurdusen, A.; Mouchaham, G.; Nouar, F.; Serre, C. Large-Scale Production of Metal–Organic Frameworks. *Adv. Funct. Mater.* **2023**, *n/a* (n/a), 2309089. https://doi.org/10.1002/adfm.202309089.

(14) Zhou, H.-C.; Long, J. R.; Yaghi, O. M. Introduction to Metal–Organic Frameworks. *Chem. Rev.* **2012**, *112* (2), 673–674. https://doi.org/10.1021/cr300014x.

(15) Zhou, H.-C. "Joe"; Kitagawa, S. Metal–Organic Frameworks (MOFs). *Chem. Soc. Rev.* **2014**, *43* (16), 5415–5418. https://doi.org/10.1039/C4CS90059F.

(16) Furukawa, H.; Cordova, K. E.; O'Keeffe, M.; Yaghi, O. M. The Chemistry and Applications of Metal-Organic Frameworks. *Science*. 2013. https://doi.org/10.1126/science.1230444.

(17) Lin, J.-B.; Nguyen, T. T. T.; Vaidhyanathan, R.; Burner, J.; Taylor, J. M.; Durekova, H.; Akhtar, F.; Mah, R. K.; Ghaffari-Nik, O.; Marx, S.; Fylstra, N.; Iremonger, S. S.; Dawson, K. W.; Sarkar, P.; Hovington, P.; Rajendran, A.; Woo, T. K.; Shimizu, G. K. H. A Scalable Metal-Organic Framework as a Durable Physisorbent for Carbon Dioxide Capture. *Science.* **2021**, *374* (6574), 1464–1469. https://doi.org/10.1126/science.abi7281.

(18) Trickett, C. A.; Helal, A.; Al-Maythalony, B. A.; Yamani, Z. H.; Cordova, K. E.; Yaghi, O. M. The Chemistry of Metal–Organic Frameworks for CO_2 Capture, Regeneration and Conversion. *Nat. Rev. Mater.* **2017**, *2* (8), 17045. https://doi.org/10.1038/natrevmats.2017.45.

(19) Adil, K.; Belmabkhout, Y.; Pillai, R. S.; Cadiau, A.; Bhatt, P. M.; Assen, A. H.; Maurin, G.; Eddaoudi, M. Gas/Vapour Separation Using Ultra-Microporous Metal–Organic Frameworks: Insights into the Structure/Separation Relationship. *Chem. Soc. Rev.* **2017**, *46* (11), 3402–3430. https://doi.org/10.1039/C7CS00153C.

(20) Allendorf, M. D.; Stavila, V.; Snider, J. L.; Witman, M.; Bowden, M. E.; Brooks, K.; Tran, B. L.; Autrey, T. Challenges to Developing Materials for the Transport and Storage of Hydrogen. *Nat. Chem.* **2022**, *14* (11), 1214–1223. https://doi.org/10.1038/s41557-022-01056-2.

(21) Li, L.; Jung, H. S.; Lee, J. W.; Kang, Y. T. Review on Applications of Metal–Organic Frameworks for CO_2 Capture and the Performance Enhancement Mechanisms. *Renew. Sustain. Energy Rev.* **2022**, *162*, 112441. https://doi.org/https://doi.org/10.1016/j.rser.2022.112441.

(22) Zhang, Z.; Ding, H.; Pan, W.; Ma, J.; Zhang, K.; Zhao, Y.; Song, J.; Wei, C.; Lin, F. Research Progress of Metal–Organic Frameworks (MOFs) for CO_2 Conversion in CCUS. *J. Energy Inst.* **2023**, *108*, 101226. https://doi.org/https://doi.org/10.1016/j.joei.2023.101226.

(23) Xu, X.; Wei, Q.; Xi, Z.; Zhao, D.; Chen, J.; Wang, J.; Zhang, X.; Gao, H.; Wang, G. Research Progress of Metal-Organic Frameworks-Based Materials for CO_2 Capture and CO2-to-Alcohols Conversion. *Coord. Chem. Rev.* **2023**, *495*, 215393. https://doi.org/https://doi.org/10.1016/j.ccr.2023.215393.

(24) Furukawa, H.; Ko, N.; Go, Y. B.; Aratani, N.; Choi, S. B.; Choi, E.; Yazaydin, A. Ö.; Snurr, R. Q.; O'Keeffe, M.; Kim, J.; Yaghi, O. M. Ultrahigh Porosity in Metal-Organic Frameworks. *Science.* **2010**, *329* (5990), 424–428. https://doi.org/10.1126/science.1192160.

(25) Baumann, A. E.; Burns, D. A.; Liu, B.; Thoi, V. S. Metal-Organic Framework Functionalization and Design Strategies for Advanced Electrochemical Energy Storage Devices. *Commun. Chem.* **2019**, *2* (1), 86. https://doi.org/10.1038/s42004-019-0184-6.

(26) Lee, S.; Kim, B.; Cho, H.; Lee, H.; Lee, S. Y.; Cho, E. S.; Kim, J. Computational Screening of Trillions of Metal–Organic Frameworks for High-Performance Methane Storage. *ACS Appl. Mater. Interfaces* **2021**, *13* (20), 23647–23654. https://doi.org/10.1021/acsami.1c02471.

(27) Moghadam, P. Z.; Li, A.; Wiggin, S. B.; Tao, A.; Maloney, A. G. P.; Wood, P. A.; Ward, S. C.; Fairen-Jimenez, D. Development of a Cambridge Structural Database Subset: A Collection of Metal–Organic Frameworks for Past, Present, and Future. *Chem. Mater.* **2017**, *29* (7), 2618–2625. https://doi.org/10.1021/acs.chemmater.7b00441.

(28) Moghadam, P. Z.; Li, A.; Liu, X.-W.; Bueno-Perez, R.; Wang, S.-D.; Wiggin, S. B.; Wood, P. A.; Fairen-Jimenez, D. Targeted Classification of Metal–Organic Frameworks in the Cambridge Structural Database (CSD). *Chem. Sci.* **2020**, *11* (32), 8373–8387. https://doi.org/10.1039/D0SC01297A.

(29) Wilmer, C. E.; Leaf, M.; Lee, C. Y.; Farha, O. K.; Hauser, B. G.; Hupp, J. T.; Snurr, R. Q. Large-Scale Screening of Hypothetical Metal–Organic Frameworks. *Nat. Chem.* **2012**, *4* (2), 83–89. https://doi.org/10.1038/nchem.1192.

(30) Goldsmith, J.; Wong-Foy, A. G.; Cafarella, M. J.; Siegel, D. J. Theoretical Limits of Hydrogen Storage in Metal–Organic Frameworks: Opportunities and Trade-Offs. *Chem. Mater.* **2013**, *25* (16), 3373–3382. https://doi.org/10.1021/cm401978e.

(31) Gomez-Gualdron, D. A.; Gutov, O. V; Krungleviciute, V.; Borah, B.; Mondloch, J. E.; Hupp, J. T.; Yildirim, T.; Farha, O. K.; Snurr, R. Q. Computational Design of Metal–Organic Frameworks Based on Stable Zirconium Building Units for Storage and Delivery of Methane. *Chem. Mater.* **2014**, *26* (19), 5632–5639. https://doi.org/10.1021/cm502304e.

(32) Chung, Y. G.; Camp, J.; Haranczyk, M.; Sikora, B. J.; Bury, W.; Krungleviciute, V.; Yildirim, T.; Farha, O. K.; Sholl, D. S.; Snurr, R. Q. Computation-Ready, Experimental Metal–Organic Frameworks: A Tool To Enable High-Throughput Screening of Nanoporous Crystals. *Chem. Mater.* **2014**, *26* (21), 6185–6192. https://doi.org/10.1021/cm502594j.

(33) Nazarian, D.; Camp, J. S.; Sholl, D. S. A Comprehensive Set of High-Quality Point Charges for Simulations of Metal–Organic Frameworks. *Chem. Mater.* **2016**, *28* (3), 785–793. https://doi.org/10.1021/acs.chemmater.5b03836.

(34) Chung, Y. G.; Haldoupis, E.; Bucior, B. J.; Haranczyk, M.; Lee, S.; Zhang, H.; Vogiatzis, K. D.; Milisavljevic, M.; Ling, S.; Camp, J. S.; Slater, B.; Siepmann, J. I.; Sholl, D. S.; Snurr, R. Q. Advances, Updates, and Analytics for the Computation-Ready, Experimental Metal-Organic Framework Database: CoRE MOF 2019. *J. Chem. Eng. Data* **2019**. https://doi.org/10.1021/acs.jced.9b00835.

(35) Daglar, H.; Gulbalkan, H. C.; Avci, G.; Aksu, G. O.; Altundal, O. F.; Altintas, C.; Erucar, I.; Keskin, S. Effect of Metal–Organic Framework (MOF) Database Selection on the Assessment of Gas Storage and Separation Potentials of MOFs. *Angew. Chemie Int. Ed.* **2021**, *60* (14), 7828–7837. https://doi.org/10.1002/anie.202015250.

(36) Colón, Y. J.; Gómez-Gualdrón, D. A.; Snurr, R. Q. Topologically Guided, Automated Construction of Metal–Organic Frameworks and Their Evaluation for Energy-Related Applications. *Cryst. Growth Des.* **2017**, *17* (11), 5801–5810. https://doi.org/10.1021/acs.cgd.7b00848.

(37) Anderson, R.; Gómez-Gualdrón, D. A. Increasing Topological Diversity during Computational "Synthesis" of Porous Crystals: How and Why. *CrystEngComm* **2019**, *21* (10), 1653–1665. https://doi.org/10.1039/C8CE01637B.

(38) Rosen, A. S.; Iyer, S. M.; Ray, D.; Yao, Z.; Aspuru-Guzik, A.; Gagliardi, L.; Notestein, J. M.; Snurr, R. Q. Machine Learning the Quantum-Chemical Properties of Metal-

Organic Frameworks for Accelerated Materials Discovery. *Matter* **2021**, *4* (5), 1578–1597. https://doi.org/10.1016/j.matt.2021.02.015.

(39) Rosen, A. S.; Fung, V.; Huck, P.; O'Donnell, C. T.; Horton, M. K.; Truhlar, D. G.; Persson, K. A.; Notestein, J. M.; Snurr, R. Q. High-Throughput Predictions of Metal–Organic Framework Electronic Properties: Theoretical Challenges, Graph Neural Networks, and Data Exploration. *npj Comput. Mater.* **2022**, *8* (1), 112. https://doi.org/10.1038/s41524-022-00796-6.

(40) Qiao, Z.; Xu, Q.; Jiang, J. Computational Screening of Hydrophobic Metal–Organic Frameworks for the Separation of H_2S and CO_2 from Natural Gas. *J. Mater. Chem. A* **2018**, *6* (39), 18898–18905. https://doi.org/10.1039/C8TA04939D.

(41) Yan, Y.; Zhang, L.; Li, S.; Liang, H.; Qiao, Z. Adsorption Behavior of Metal-Organic Frameworks: From Single Simulation, High-Throughput Computational Screening to Machine Learning. *Comput. Mater. Sci.* **2021**, *193*, 110383. https://doi.org/https://doi.org/10.1016/j.commatsci.2021.110383.

(42) Chung, Y. G.; Bai, P.; Haranczyk, M.; Leperi, K. T.; Li, P.; Zhang, H.; Wang, T. C.; Duerinck, T.; You, F.; Hupp, J. T.; Farha, O. K.; Siepmann, J. I.; Snurr, R. Q. Computational Screening of Nanoporous Materials for Hexane and Heptane Isomer Separation. *Chem. Mater.* **2017**, *29* (15), 6315–6328. https://doi.org/10.1021/acs.chemmater.7b01565.

(43) Demir, H.; Daglar, H.; Gulbalkan, H. C.; Aksu, G. O.; Keskin, S. Recent Advances in Computational Modeling of MOFs: From Molecular Simulations to Machine Learning. *Coord. Chem. Rev.* **2023**, *484*, 215112. https://doi.org/https://doi.org/10.1016/j.ccr.2023.215112.

(44) Al-Rowaili, F. N.; Zahid, U.; Onaizi, S.; Khaled, M.; Jamal, A.; AL-Mutairi, E. M. A Review for Metal-Organic Frameworks (MOFs) Utilization in Capture and Conversion of Carbon Dioxide into Valuable Products. *J. CO_2 Util.* **2021**, *53*, 101715. https://doi.org/https://doi.org/10.1016/j.jcou.2021.101715.

(45) Younas, M.; Rezakazemi, M.; Daud, M.; Wazir, M. B.; Ahmad, S.; Ullah, N.; Inamuddin; Ramakrishna, S. Recent Progress and Remaining Challenges in Post-Combustion CO_2 Capture Using Metal-Organic Frameworks (MOFs). *Prog. Energy Combust. Sci.* **2020**, *80*, 100849. https://doi.org/https://doi.org/10.1016/j.pecs.2020.100849.

(46) Wilmer, C. E.; Farha, O. K.; Bae, Y.-S.; Hupp, J. T.; Snurr, R. Q. Structure–Property Relationships of Porous Materials for Carbon Dioxide Separation and Capture. *Energy*

Environ. Sci. **2012**, *5* (12), 9849–9856. https://doi.org/10.1039/C2EE23201D.

(47) Chung, Y. G.; Gómez-Gualdrón, D. A.; Li, P.; Leperi, K. T.; Deria, P.; Zhang, H.; Vermeulen, N. A.; Stoddart, J. F.; You, F.; Hupp, J. T.; Farha, O. K.; Snurr, R. Q. In Silico Discovery of Metal-Organic Frameworks for Precombustion CO_2 Capture Using a Genetic Algorithm. *Sci. Adv.* **2024**, *2* (10), e1600909. https://doi.org/10.1126/sciadv.1600909.

(48) Dantas, S.; Neimark, A. V. Coupling Structural and Adsorption Properties of Metal–Organic Frameworks: From Pore Size Distribution to Pore Type Distribution. *ACS Appl. Mater. Interfaces* **2020**, *12* (13), 15595–15605. https://doi.org/10.1021/acsami.0c01682.

(49) Leperi, K. T.; Chung, Y. G.; You, F.; Snurr, R. Q. Development of a General Evaluation Metric for Rapid Screening of Adsorbent Materials for Postcombustion CO_2 Capture. *ACS Sustain. Chem. Eng.* **2019**, *7* (13), 11529–11539. https://doi.org/10.1021/acssuschemeng.9b01418.

(50) Farmahini, A. H.; Krishnamurthy, S.; Friedrich, D.; Brandani, S.; Sarkisov, L. Performance-Based Screening of Porous Materials for Carbon Capture. *Chem. Rev.* **2021**, *121* (17), 10666–10741. https://doi.org/10.1021/acs.chemrev.0c01266.

(51) Moghadam, P. Z.; Rogge, S. M. J.; Li, A.; Chow, C.-M.; Wieme, J.; Moharrami, N.; Aragones-Anglada, M.; Conduit, G.; Gomez-Gualdron, D. A.; Van Speybroeck, V.; Fairen-Jimenez, D. Structure-Mechanical Stability Relations of Metal-Organic Frameworks via Machine Learning. *Matter* **2019**, *1* (1), 219–234. https://doi.org/10.1016/j.matt.2019.03.002.

(52) Healy, C.; Patil, K. M.; Wilson, B. H.; Hermanspahn, L.; Harvey-Reid, N. C.; Howard, B. I.; Kleinjan, C.; Kolien, J.; Payet, F.; Telfer, S. G.; Kruger, P. E.; Bennett, T. D. The Thermal Stability of Metal-Organic Frameworks. *Coord. Chem. Rev.* **2020**, *419*, 213388. https://doi.org/https://doi.org/10.1016/j.ccr.2020.213388.

(53) Moghadam, P. Z.; Chung, Y. G.; Snurr, R. Q. Progress toward the Computational Discovery of New Metal–Organic Framework Adsorbents for Energy Applications. *Nat. Energy* **2024**, *9* (2), 121–133. https://doi.org/10.1038/s41560-023-01417-2.

2. Theoretical Background

2.1 Metal Organic Frameworks

Metal Organic Frameworks (MOFs) are coordination networks containing potential voids formed by metal ions or oxo-metallic clusters, termed as secondary building units (SBUs), connected by polytopic ligands. Both metal ions and polytopic ligands are connected to form a framework in an alternating fashion and producing porous materials as shown in Figure 2.1.[1] The variety of combinations between metals and organic linkers opens up the possibility of synthesising various MOFs with different pore sizes and shapes. Such geometric and surface chemistry features can also be varied and controlled by the functionalisation of organic linkers, in order to tune their properties for a desired adsorption application. These adjustable properties are not common in traditional porous materials such as zeolites and activated carbons, which have been widely used in several chemical processes, for instance gas storage[2,3] and separation[4,5] as well as catalysis.[6]

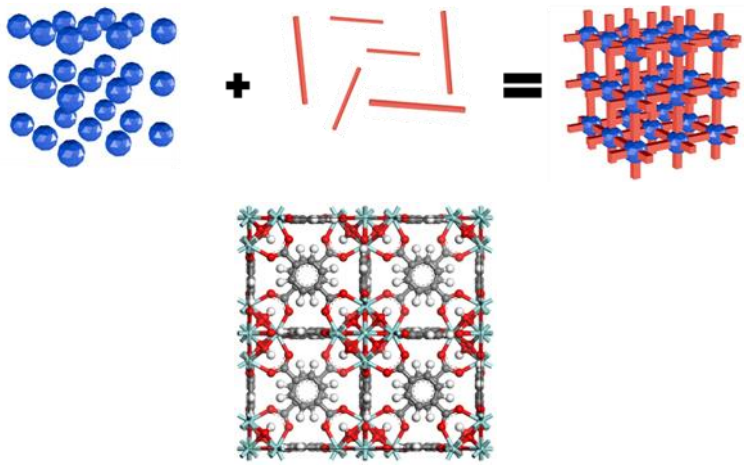

Figure 2.1. Top: MOF self-assembly process from building blocks: metal clusters (red spheres) and organic ligands (blue struts). Bottom: Example of a well-known MOF with the Zr-oxide metal nodes; UiO-66.[7] oxygen (red), carbon (grey), hydrogen (white), zirconium (light blue).

2.1.1 Categories of MOFs

MOFs can be classified into the following groups according to their structural properties:

(i) Rigid Framework MOFs

Rigid MOFs are a distinct subgroup of MOFs that exhibit unique features distinguishing them from other types of MOFs. These attributes encompass a high degree of structural rigidity, which arises from the existence of robust metal-ligand interactions and a highly interconnected

framework topology. The robust coordination bonds establish a solid framework that interconnects the metal nodes and organic linkers, thereby preventing the structure from easily collapsing or deforming. The presence of this network improves the overall rigidity of MOFs distributing mechanical stress across the entire structure. Moreover, the robust coordination connections formed between metal nodes and organic linkers effectively limit the mobility of individual components within the framework, hence increasing its overall rigidity.[8] MOFs in this group usually have a stable and robust porous framework with very high porosity. In addition, these MOFs can maintain their pore structure when there is an interaction with the adsorbate molecules in adsorption or desorption cycles.

The majority of the organic linkers employed in the synthesis of MOFs consist of molecules containing aromatic groups which gives rigidity to the MOF framework. Typical aromatic ligands in MOFs are carboxylic acid,[9–11] heterocyclic aromatic rings containing N atoms (e.g. pyridine)[12,13] or other coordinating functional groups such as sulfonates[14,15] and phosponates.[16,17] In addition, rigid MOFs frequently exhibit a significant level of porosity and surface area, which greatly enhance their ability to adsorb gases. Additional prevalent attributes of rigid MOFs include high thermal and chemical stability, making them well-suited for use in harsh environments, and the capacity to maintain their structural integrity under extreme conditions.[8] Examples of well-known MOFs without significant structural flexibility include: MOF-5 [Zn_4O (terephthalate)$_3$] with its cubic structure which has surface area of 3,800 m^2/g.[18] Other examples of MOFs of this type which have high porosity and high surface areas of 4,746 and 6,260 m^2/g, are MOF-177 [Zn_4O (btb)$_2$] and MOF-200 [Zn_4O (bbc)$_2$], respectively.[19,20] The use of chromium metal to replace the ZnO metal cluster on this type of MOF will produce MIL-101 [Cr_3F (H_2O)O(bdc)$_3$] having surface area of 4,100 m^2/g.[21]

(ii) Flexible framework MOFs for gas adsorption application

Although MOFs were originally conceived as structures composed of rigid, aromatic linkers as struts and metal clusters as nodes, it is now known that certain MOFs can exhibit flexibility when exposed to external stimuli such as pressure and temperature.[22] These particular MOFs possess flexible frameworks and lack rigidity, so they are referred to as flexible MOFs. Numerous flexible MOFs with flexible structural characteristics have been reported, specifically designed for a wide range of applications including gas adsorption and separation, catalysis, and sensing.[23,24] The ordered crystal structure of these flexible MOFs possesses the ability to undergo transformations through various mechanisms, such as phase changes or gate

opening.[24–26] The phenomenon of flexibility is frequently observed during the adsorption-desorption process, wherein the interaction between adsorbate molecules and the surface of the pore is considered to be the source of this flexibility.[27,28] Flexible frameworks have the ability to expand or contract during the incorporation or removal of guest molecules, enabling a wide range of guest interchange. This effect is apparent in the case of MIL-53(Cr), where the unit cell size is reduced compared to the as-synthesized form (MIL-53-as) when humid air is adsorbed, resulting in the formation of a contracted low-temperature form (MIL-53-lt). During the adsorption phase, the cell volume undergoes a reduction of 32%.[29]

Pressure is a thermodynamic property that is strongly linked to the flexibility of materials.[30,31] The impact of pressure on a material is directly correlated to its mechanical stability, which is crucial for various commercial applications. Flexible MOFs have the ability to spin or relax easily when subjected to external pressure. For instance, it was demonstrated that dense $Zn(im)_2$ (im = imidazolate) undergoes an irreversible cooperative bond rearrangement when pressure is applied, as observed through single crystal X-ray diffraction measurement.[32]

Another effect that can be observed in flexible MOFs is gate-opening. Gate-opening refers to the physical occurrence in which the pore or gate of a framework opens when exposed to a stimulus, particularly external adsorbate molecules.[24,25] Gate-opening refers to the transformation from a non-porous to a porous state.[32] ZIF-7 and ZIF-8, which are part of the Zeolitic Imidazolate Framework (ZIF), have shown significant gate opening when exposed to various gases, resulting in exceptional selectivity.[33,34] FMOF-2, a type of flexible MOF, consists of a zinc-based SBU (Secondary Building Unit) and a V-shaped fluorinated linker called 2,2-bis(4-carboxyphenyl)hexafluoropropane. This MOF exhibits significant expansion and contraction behavior when exposed to gases. The material exhibits stepwise adsorption for acidic gases such as SO_2 and H_2S at pressures ranging from 0 to 1 bar, while for CO_2 occurs at a higher pressure ($\geq$ 10 bar).[35]

(iii) MOFs with unsaturated metal sites (open metal sites) for gas adsorption application

MOFs sometimes have a variety of specific functionalities that is mainly controlled by pore size and the presence of free coordination sites or well-known as open metal sites. The concept of free coordination sites in organometal chemistry exists with a lower than normal coordination number of the metal atom. For example, a 3d metal atom presents in UiO-66 in which an octahedron of Zr atom with coordination number of six would be expected, but only

fivefold coordination occurs due to a missing ligand would establish a free coordination sites. In MOFs, the metal ion that is not fully coordinated is termed as open metal sites (OMS). The most well-know and first MOFs with OMS synthesized in 1999 was HKUST-1 that is commercially available as Basolite C300 by BASF.[36] A Zn-based MOF synthesized with OMS was reported by Yaghi *et al*. in 2000 named as MOF-4.[37] The presence of OMS in MOFs often offer the strongest binding sites leading to the enhancement of MOFs interaction with different sorbate molecules, compared to MOFs without OMS.[38] Hence, these OMS-MOFs are considered as a promising candidates for gas adsorption applications.

One particular application of OMS-MOFs is CO_2 capture that has been receiving much scientific attention since CO_2 is hazardous to the atmosphere alarming the greenhouse gas effect. The presence of OMS in MOFs enhance the binding affinity between CO_2 adsorbate and the OMS that is correlated with high electrostatic interactions since CO_2 is a quadropolar gas molecule.[39] MOF-74 (CPO-27-Mg, Mg_2(dobdc))[40] is currently taken as a benchmark of MOF materials in CO_2 adsorption due to its excellent CO_2 uptake and its remarkable selectivity. Extensive studies on CO_2 adsorption mechanism to this material reveal that an open Mg^{2+} site generated upon the thermal activation of the material enhance the interaction of CO_2 molecule with MOF-74-Mg.[41] Neutron powder diffraction supported by *in situ* ^{13}C NMR measurements was performed to confirm that the OMS in Mg-MOF-74 becomes the most preferential sites upon adsorption of CO_2.[42–45] The CO_2 capacity of Mg-MOF-74 is 0.81 $mol.mol^{-1}$ according to the CO_2 adsorption isotherms measured at 298 K and 0.1 bar.[44]
HKUST-1 (Cu-BTC) is another example of OMS-MOFs that has been extensively investigated for its CO_2 capture performance. According to X-Ray absorption fine structure (XAFS) study conducted by Du, et al.[46], it was demonstrated that the CO_2 molecule bind with the Cu^{2+} center of Cu-BTC during CO_2 physiosorption process. This phenomenon was further confirmed by Wu, et al.[42] who conducted neutron diffraction experiment combined with theoretical calculation to explore the CO_2 interaction with HKUST-1. This study revealed that the preferential CO_2 adsorption site is the metal center of HKUST-1 containing Cu^{2+} due to the strong electrostatic energy interaction between quadrupole moment of CO_2 and Cu^{2+}. A new Co-based MOFs synthesized by Zhu, et al.,[47] decorated by μ_3–OH groups, indicated that the presence of accessible OMS in $\{[Co_2(tzpa)(OH)(H_2O)_2]\cdot DMF\}_n$ (H_3tzpa = 5-(4-(tetrazol-5-yl)phenyl)isophthalic acid) generated by the removal of coordinated water molecule led to high CO_2 adsorption capacity at the temperature range of 298 – 333 K.

(iv) Functionalized MOFs for gas adsorption application

MOFs can be modified by grafting specific functional groups on their organic linker or metal nodes. The addition of such functional groups can enhance the adsorption capacity of MOFs for certain gases. For example, the addition of an arylamine group, hydroxyl or alkylamine can increase the affinity of MOFs to CO_2 leading to an increase in adsorption capacity and selectivity. The addition of functional groups to MOFs can be performed by modifying the linkers or appropriate coordination sites with the unsaturated metal clusters. An example of surface functionalization of MOFs is the amine functionalised aluminium-based MOF, MIL-53. By adding an amine group, this MOF exhibits a separation factor of 60 for CO_2 uptake in the adsorption process of a mixture of methane and CO_2 gas surpassing the pristine MIL-53 which only has a separation factor of 5.[48]

The same trend was shown by USO-2-Ni and USO-3-In-A which experienced a significant increase in their adsorption power when compared to their pristine framework.[49] Tetraethylenepentamine (TEPA) was impregnated during post-synthetic functionalization to magnesium 2,5-dihydroxyterephthalate (Mg-MOF-74), which resulted an improvement for CO_2 uptake capacity as high as 26.9 wt% compared to 23.4 wt% for the original Mg-MOF-74.[50] A tetra-amide functionalized metal-organic framework, MFM-188, revealed its exceptional high uptake of CO_2 and acetylene c.a. 232 $cm^3.g^{-1}$ at 295 K and 1 bar. This trend was mainly due to the combination of polyamide groups, open metal sites, appropriate pore geometry, and cooperative binding between guest molecules.[51]

(v) Defective MOFs for gas adsorption application

Defects in MOFs is always correlated with missing linker or metal cluster defect, thus creating more pore spaces and providing an additional active sites for enhancing the guest molecule diffusion and mass transfer in MOFs. Defects in porous coordination network compounds, such as MOFs are defined as “sites that locally break the regular periodic arrangement of atoms or ions of the static crystalline parent framework because of dislocated atoms or ions”.[52]

Structural defects in MOFs is currently considered as a useful tool for tailoring both physical and chemical properties of MOFs to optimize the acidity/basicity. Hence, this could possibly give a positive effect in gas adsorption capacity for MOFs.[53–55] The chemical environment of pore due to defects may affect the interaction between adsorbate molecule and the host framework, and subsequently, the adsorption properties of MOFs.[56] HKUST-1 with an acetic acid-fragmented linker strategy was developed by Kim, *et al.*[54] could create a mesoporous

defect. This defect could enhance the methane uptake up to 16% of higher deliverable capacity between 5 bar and 65 bar than the parent HKUST-1. The enhancement is due to the increased pore volume and surface area in the prepared acetic-acid fragmented HKUST-1. The introduction of boronic acid moieties as functional defects in UiO-66 by Erkartal, et al.[57] could enhance the CO_2 selectivity over N_2 and CH_4 attributed from the quadropolar interaction between CO_2 and modified UiO-66. CAU-1 with rich aluminium defect reported by Jiao, *et al.*[58] exhibits a significant increased CO_2 uptake at low pressure due to the presence of metal defects that creates more active binding site.

2.1.2 MOFs characterisation

BET area

One of the key characteristics of MOFs is their large surface area. In experiments, the surface area is usually measured from N_2 or Ar gas adsorption isotherms at temperatures of 77 K and 87 K, respectively. The main reason for using N_2 and Ar for surface area characterisation is that they are inert and non-toxic. Figure 2.2 shows an example of a N_2 adsorption isotherm for NU-901 and NU-1000.[59] The amount of adsorbed N_2 gas is typically expressed in units of cm^3/g which is normalised under standard temperature and pressure conditions. The x-axis on the graph does not represent the measured pressure but it is expressed in relative pressure, P/P_0 where P_0 is the pressure of N_2 or Ar gas at saturation conditions.

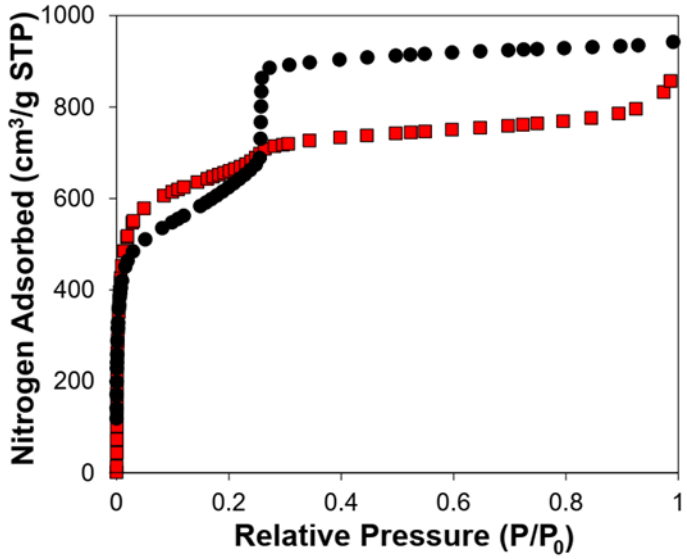

Figure 2.2. N_2 adsorption isotherms at 77 K for NU-901 (red square) and NU-1000 (black circle). Reprint from Teplensky, et al.[59] Copyright © 2017 American Chemical Society.

The adsorption isotherms data can be converted to surface area by using the most commonly Brunauer – Emmett – Teller (BET) model. This BET model was first developed in 1938 which

is an extension of the Langmuir model.[60] BET model assumes that the adsorption process that occurs on the adsorbent surface is multi-layer, meaning that the second layer and so on can be formed in the first layer of the adsorbate molecule.[60] Other assumption used for the implementation of the BET theory for calculating the surface area are mentioned below:

a. Adsorption consists of a regular array of adsorption sites equal in energy, with a constant enthalpy of adsorption in the monolayer, ΔH_A
b. Adsorption is localized to these sites
c. Neighboring adsorbed molecules do not interact
d. Multilayer formation is unlimited
e. Enthalpy of adsorption in second and subsequent multilayers is equal to the enthalpy of liquefaction, ΔH_L

Adsorption and desorption may only occur on or from exposed sites

This model uses equation (2.1) to calculate the monolayer capacity

$$\frac{1}{X\left[\left(P_0/P\right)-1\right]} = \frac{1}{X_m C} + \frac{C-1}{X_m}\left(\frac{P}{P_0}\right) \tag{2.1}$$

where X is the weight of nitrogen adsorbed at a given relative pressure (P/P_0), X_m is the monolayer capacity - the volume of gas adsorbed at standard pressure and temperature (STP) in cc/g unit, and C is constant, dimensionless quantity and related to the adsorption energy, expressed as:

$$C = \left[\left(\Delta H_A - \Delta H_L / RT\right)\right]$$

where ΔH_A = the heat of adsorption of the first adsorbed layer in kJ/mol

ΔH_L = the heat of adsorption of the second and subsequent multilayers in kJ/mol

From equation (2.1), we can plot several data points, usually in the range of relative pressure, P/P_0 of 0.025 to 0.30 to generate a linear plot. From the plotting, we will be able to obtain the slope and intercept using the least-square method where the slope value must be positive. The value of X_m can be calculated using an equation (2.2)

$$X_m = \frac{1}{s+i} \tag{2.2}$$

where s is the slope and i is the intercept. When the value of X_m is known, the BET surface area can be calculated directly using equation (2.3)

$$S = \frac{X_m L_{av} A_m}{M_v} \tag{2.3}$$

where L_{av} is Avogadro's number, A_m is the cross sectional area of the adsorbate which equals to an adsorbed nitrogen molecule (0.162 nm^2), and M_v is the molar volume and equals 22.414 L.

In calculating the surface area of MOFs, the BET value of this area is often sensitive to the selection of the P/P_0 range.[61] Selecting the different P/P_0 range will result in a different BET area calculation value. To overcome this problem, there are four consistency criteria proposed by Rouquerrol, et al.[62] and these four consistency criteria are very important to be applied in each BET area calculation for MOFs as emphasized by previous studies.[63] The four consistency criteria can be described as follows:

1. The plotting results and the P/P_0 range selected in equation (2.1) must produce a linear graph with $R^2 > 0.995$ and should increase monotonically.
2. The C value generated from linear regression in equation (2.1) must give a positive value.
3. Monolayer loading, X_m must be at the N_2 gas adsorption value within the selected P/P_0 range. To determine the value of P/P_0 which represents the value of X_m, linear interpolation method can be used.

The relative pressure P/P_0 which represents the Xm value calculated by the equation $(1/\sqrt{C} + 1)$ according to the BET theory must be equal to the P/P_0 value in criterion 3. (for this criterion a maximum tolerance value of 20% can be used as suggested by Rouquerrol, *et al*.[62]

2.2. MOF Applications

MOFs have emerged as a significant advancement in the field of porous materials science. MOFs have been extensively investigated across various domains, including but not limited to gas storage and separation,[3,5,64,65] bioimaging,[66] catalysis,[67] batteries,[68] supercapacitors,[69] and drug delivery.[70] These materials have then garnered considerable attention due to their emerging integration into industrial applications, particularly in the domains of gas storage and separation. MOFs for H_2 storage was first reported by Yaghi, et al. in 2003 (MOF-5) with the storage capacity of 7.1 excess wt % at 77 K and 40 bar.[18] Subsequently, extensive research efforts have been dedicated to the exploration of numerous MOFs, with the aim of assessing their viability for H_2 storage applications. These includes the investigation on NOTT-112, NU-111, and NU-100/PCN-610 with the total gravimetric H_2 uptakes at 77 K and 70 bar are 10.0, 13.6, and 16.4 wt%, respectively.[71–74] In a recent study conducted by Kapelewski et al.,[75] an assessment was made on the usable volumetric H_2 capacities of Ni_2(*m*-dobdc) (where *m*-

dobdc^{4-} refers to 4,6-dioxido-1,3-benzenedicarboxylate). This particular compound was chosen due to its high density of coordinatively unsaturated metal sites, which exhibit a strong interaction with H_2. Ni_2(*m*-dobdc) exhibited a volumetric capacity within the range of 100 to 5 bar, measuring 11.0 g/L at a temperature of 25°C. Furthermore, it demonstrated a volumetric capacity of 23.0 g/L when subjected to a temperature swing from -75 to 25°C. These results establish Ni_2(*m*-dobdc) as the most effective physisorptive storage material discovered thus far.

MOFs has been also intensively studied for storing natural gas / methane. Given the moderate nature of the interactions between MOFs and CH_4, it is feasible to store CH_4 in MOFs under ambient conditions and reasonably high pressures. This approach holds significant potential and practicability. Significant advancements have been achieved in the field of CH_4 storage subsequent to the independent discoveries by Kitagawa[76] and Yaghi,[77] who pioneered the development of the initial two instances of MOFs for this application. The analysis of extensive experimental data reveals a strong linear correlation between the gravimetric CH_4 storage capacities of MOFs under high pressure conditions and their respective pore volumes or surface areas.[78]

The study performed by Peng et al.[79] examined the CH_4 storage properties of six prototypical MOFs (HKUST-1, NiMOF-74, PCN-14, UTSA-20, NU-111, and NU-125) which possess diverse structural characteristics. The findings of their study demonstrated a linear relationship between the BET surface area and various parameters, including the total gravimetric CH_4 uptake (at 298 K and 65 bar), pore volume, and inverse density of the MOFs. One of the series, NU-111, exhibits a measured BET surface area of 4930 m^2/g and demonstrates the highest gravimetric uptake of 0.36 g/g. This research finding also indicated that HKUST-1 demonstrates an exceptional total volumetric CH_4 capacity of 267 cm^3 (STP)/cm^3 at a temperature of 298 K and a pressure of 65 bar where this value complies with the target set by the U.S. Department of Energy (DOE).

One potential approach to enhance the gravimetric CH_4 capacity in MOFs involves the exploration or creation of MOFs characterised by elevated levels of porosity. Alezi et al.[64] introduced a new aluminium MOF called Al-soc-MOF-1 with notable characteristics. This MOF exhibits an unusually high pore volume of 2.3 cm^3/g and a BET surface area of 5585 m^2/g. This MOF demonstrates the most significant recorded total gravimetric CH_4 uptake of approximately 580 cm^3 (STP)/g (0.42 g/g) at a temperature of 298 K and pressure of 65 bar. Furthermore, it accomplishes 83% of the gravimetric target set by DOE.

In addition to the development of MOFs with appropriate pore sizes, the integration of functional groups/sites into MOFs represents an alternative strategy for augmenting their volumetric capacities for CH_4 storage. The implementation of a dual approach involving the extension of organic linkers and the incorporation of functional sites into MOFs was discovered to be successful in enhancing the CH_4 storage capacities. In 2018, Wen et al.[80] successfully synthesised a novel MOF referred to as UTSA-110a. This MOF was created using an extended linker that possessed a greater concentration of functional nitrogen sites in comparison to the previously developed UTSA-76. As expected, the UTSA-110a material demonstrated notable gravimetric (402 cm^3 (STP)/g) and volumetric (241 cm^3 (STP)/cm^3) total CH_4 capacities when measured at a temperature of 298 K and a pressure of 65 bar. This is due to the enhanced porosity caused by higher content of functional N sites than UTSA-76. UTSA-110a exhibited a comparatively low CH_4 uptake at a pressure of 5.8 bar. However, it demonstrated superior performance in terms of both gravimetric and volumetric working capacities, achieving values of 317 cm^3 (STP)/g and 190 cm^3 (STP)/cm^3, respectively. These results indicate that UTSA-110a outperformed both HKUST-1 and UTSA-76 in terms of its ability to store methane.

Another interesting application MOFs is their excellent performance as CO_2 capture solid sorbent.[81] Yaghi's group in 1998, first reported CO_2 capture utilizing a MOF.[82] They measured CO_2 adsorption isotherm in MOF-2 at a relatively low temperature of 195 K. Their findings indicated that the material exhibits a significant level of CO_2 adsorption at low pressures, followed by a saturation point at higher pressures. Motivated by this finding, Yaghi's team again measured a series of MOFs from ultrahigh porosity frameworks, e.g IRMOF-1 and MOF-177 to MOFs with open metal sites such as MOF-505 and $Cu_3(BTC)_2$, as well as functionalised IRMOF (IRMOF-3 and IRMOF-6).[83] The adsorption isotherms demonstrated that the IRMOFs with the $Zn_4O(O_2C)^{6-}$ type framework, specifically IRMOFs (-3, -6, -11), exhibit higher capacities for CO_2 uptake compared to other MOFs. MOF-177 material, known for its exceptional porosity, demonstrates a significantly higher CO_2 storage capacity of 33.5 mmol/g at 3.2 MPa compared to the widely recognised commercial absorbent Zeolite 13 X, which has a maximum CO_2 uptake capacity of 7.4 mmol/g. Consequently, an increased number of investigations have been undertaken to explore the phenomenon of high-pressure gravimetric carbon dioxide adsorption in diverse MOFs characterised by their substantial porosity and surface area. In their study, Llewellyn et al.[84] conducted measurements to assess the adsorption of CO_2 in mesoporous MOFs, specifically focusing on MIL-100 and MIL-101. The experimental results revealed that MIL-101 demonstrated an impressive CO_2 loading capacity,

achieving a record value of 40 mmol/g under conditions of 5 MPa pressure and a temperature of 303 K. In their study, Yuan et al.[74] examined the CO_2 uptake capacities of a series of isoreticular PCN-6X materials. Their findings revealed that PCN-68 exhibited the most significant gravimetric CO_2 uptake capacity, measuring 30.4 mmol/g at a temperature of 298 K and a pressure of 35 bar.

Nevertheless, it is commonly anticipated that the practical adsorption of CO_2 will occur under moderate conditions, specifically at room temperature and atmospheric pressure. MOFs exhibiting substantial CO_2 adsorption capacity under elevated pressures do not exhibit a favourable affinity for CO_2 at lower pressures. Some research has now been focused on the enhancement of CO_2 uptake at low pressures. A notable study[85] reported the efficacy of Mg-MOF-74, a material with abundant open magnesium sites, in capturing CO_2. The material achieved a remarkable CO_2 capture capacity of 8.9 wt % (8.48 mmol/g) at 1 bar. As the research progressed, a novel category of MOFs called Zeolitic Imidazolate Frameworks (ZIFs) emerged, demonstrating exceptional potential as highly efficient porous materials for the selective adsorption and separation of pure CO_2 from complex mixtures. ZIF-69, possessing a surface area of 1970 m^2/g, exhibits a notable capacity to adsorb CO_2 at 273 K and ambient pressure, surpassing the performance of numerous contemporary materials regarded as state-of-the-art. This adsorption capability allows ZIF-69 to accommodate a substantial quantity of CO_2, measuring 83 L (162 g).[86]

2.3. Molecular Simulation

2.3.1 Grand Canonical Monte Carlo

With the development of the number of MOFs that are significant in the last three decades, molecular simulation methods can be considered a prospective method to predict the amount of fluid adsorbed in porous materials. Gas adsorption in MOFs is typically studied via grand canonical Monte Carlo (GCMC) and molecular dynamics simulations.[87] In the adsorption process, GCMC is, in principle, used to determine the amount of fluid adsorbed in porous materials at equilibrium conditions, namely, at a constant temperature, pressure, and chemical potential. In contrast, the number of molecules adsorbed (the adsorbate) fluctuates similar to experimental conditions in the adsorption process where the phase adsorbed is in equilibrium with its bulk phase.

The theory of the fluctuation configuration of the adsorbate amount that is adsorbed in the adsorbent until reaching the equilibrium at GCMC can be explained as follows:

1. Building initial configuration of the system where one adsorbate molecule already placed in the adsorbent framework is randomly picked and the potential of old energy, U_{old} is evaluated
2. The adsorbate molecule coordinates are randomly perturbed via a Monte Carlo trial move.
3. Evaluating the potential energy of the new configuration, U_{new}.
4. Accepting the trial if U_{new} is lower than U_{old}. If U_{new} is higher than U_{old}, then the new configuration will be accepted with a certain probability < 1 which is given by the Boltzmann factor:

$$P_{acc} = \begin{cases} \exp\left[-\beta\left(U_{new} - U_{old}\right)\right] & \Leftarrow U_{NEW} > U_{OLD} \\ 1 & \Leftarrow U_{NEW} \le U_{OLD} \end{cases}$$

5. Changing to new configuration (if rejected, keep the old configuration.

When the equilibrium condition is reached, the thermodynamic property is calculated as the average of all the configurations in the simulation as shown in equation (2.4)

$$\langle A \rangle_{\mu VT} = \frac{1}{\Xi_{\mu VT}} \sum_N \frac{1}{N!} \frac{V^N}{\Lambda^{3N}} \int dr^N A\left(r^N\right) e^{\beta(N\mu - U)} \tag{2.4}$$

where $\langle \ldots \rangle$ denotes the ensemble average with $\beta = \frac{1}{k_B T}$ where k_B is the Boltzmann constant, A is the macroscopic observable property. Λ is the De Broglie wave length given in the equation (2.5)

$$\Lambda = \sqrt{\beta h^2 / 2\pi m} \tag{2.5}$$

where h is Planck's constant and m is the mass of the molecule.

$\Xi \mu VT$ is defined as the total of all possible microstates and is expressed by equation (2.6)

$$\Xi_{\mu VT} = \sum_N Q_{NVT} e^{\beta N \mu} \tag{2.6}$$

μ is the chemical potential associated with the fugacity of the bulk fluid phase and is usually one of the input parameters of the GCMC simulation formulated by equation (2.7)

$$\mu = \frac{1}{\beta} \ln\left(\beta f \Lambda^3\right) \tag{2.7}$$

In the GCMC simulation, a constant chemical potential value is desired, so it is necessary to fluctuate the configuration of the number of N molecules. This process can be achieved if

there is a random movement of particle insertion and deletion. When a particle is introduced into the system, the number of molecules originally N will become $N + 1$. This configuration will be accepted if it meets the acceptance probability as

$$Acc_{N+1} = \min\left[1, \frac{V}{\Lambda^3(N+1)} e^{\beta\mu} e^{-\beta\Delta U}\right] \qquad (2.8)$$

Similar with particle insertion, if any particles are removed from the system, the number of molecules initially N will become N-1 and this configuration will be accepted if it meets the criteria in equation (2.9).

$$Acc_{N-1} = \min\left[1, \frac{\Lambda^3 N}{V} e^{-\beta\mu} e^{-\beta\Delta U}\right] \qquad (2.9)$$

2.3.2 GCMC simulation for gas adsorption predictions

Simulations of gas adsorption using GCMC requires several input parameters. These parameters will be used to calculate the interaction energy between the adsorbate molecules, the gas, and all the atoms contained in the porous material. The first input parameters that must be set are the target temperature and pressure. These parameters will relate to the gas and porous materials' fugacity to calculate the chemical potential value in the equation (2.4). The adsorption process is a fluid phase equilibrium problem with the adsorbent, as shown in Figure 2.3. Where in equilibrium conditions, several requirements must be met according to the equation (2.10)

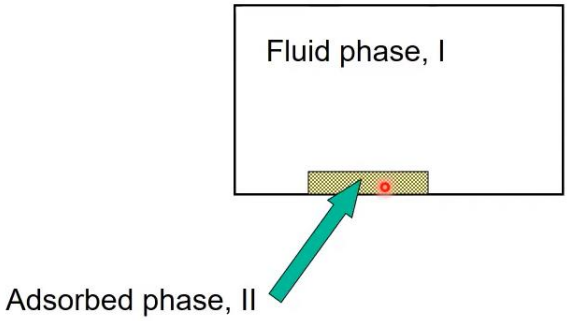

Figure 2.3. Schematic diagram of phase equilibrium between fluid phase and adsorbed phase

At equilibrium:

$$\begin{aligned} f^I &= f^{II} \\ T^I &= T^{II} \\ \mu^I &= \mu^{II} \end{aligned} \qquad (2.10)$$

where f is the fugacity in atm, T is the temperature in Kelvin, and μ is chemical potential.

The second and most important input parameter is the selection of a force field to describe adsorbate-adsorbate and adsorbate-adsorbent interactions. Generally, general-purpose force fields such as the Universal force field[88] and the Dreiding force field[89] are the most commonly used to represent these interactions. Typically, force field parameters are divided into bonded and non-bonded parameters. Here we focus mainly on the non-bonded parameters, since the adsorbates and the MOF adsorbents in our studies were considered as rigid molecules.

Non-bonded parameters describe interaction between non-bonded species. Such interactions can be of van der Waals (vdW) and/or Columbic interactions. Figure 2.4 schematically illustrates both vdW and Columbic interactions. Equation (2.11) can be used to determine the vdW interactions using the Lennard-Jones (L-J) potential.

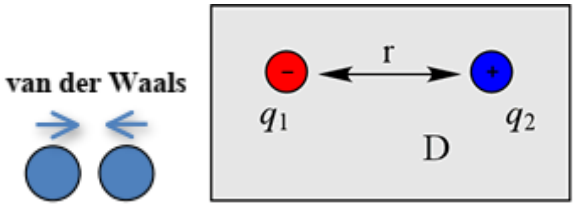

Columbic

Figure 2.4. Illustration of vdW and Columbic interaction between two atoms; D is the dielectric constant, q_1 and q_2 are point charges of two atoms separated by the distance r

$$U\left(r_{ij}\right)=4\varepsilon_{ij}\left[\left(\frac{\sigma_{ij}}{r_{ij}}\right)^{12}-\left(\frac{\sigma_{ij}}{r_{ij}}\right)^{6}\right] \qquad (2.11)$$

where *U(rij)* is the intermolecular energy, r_{ij} is the distance between molecules *i* and *j* , ε_{ij} is the depth of potential well and σ_{ij} is the hard sphere diameter.

The L-J potential is a model that accurately describes the fundamental characteristics of interactions between atoms and molecules. Two particles exhibit repulsive forces when they are in close distance, attractive forces when they are at a moderate distance, and no interactions when they are at infinite distance.[90] When we revisit equation (2.11), the vdW interaction is strongly dependent on the distance between the *i* and *j* molecules. In this case, *i* can be considered an atom in the adsorbate molecule, and *j* an atom in the MOF crystalline structure. If the distance between the atoms is too far away, the interaction energy will be small close to zero, as shown in Figure 2.5. In GCMC, it is necessary to set the energy cut-off radius and make the assumption that if the distance between two interacting sites exceeds this cut-off radius, the interaction energy is simply negligible.

Adsorbate molecules can be modelled as a single interaction site, for example, methane in which each carbon and its bonded hydrogens can be treated as a united-atom model. A quadrupolar molecule that has a charge such as CO_2 is treated as two atoms, namely C and O. This model has three L-J sites that model the overlap and dispersion forces. The C-O bond length and O-C-O bond angle are fixed at the experimental value of 1.16 Å and at 180°, respectively.[72] For CO2 and water, we used the TraPPE[91] or TiP4P[92] models. To calculate the L-J cross interactions, in general, the Lorentz-Berthelot mixing rules are often used, which are shown in equations (2.12) and (2.13).

$$\sigma_{ij} = 0.5\left(\sigma_i + \sigma_j\right) \tag{2.12}$$

$$\varepsilon_{ij} = \sqrt{\varepsilon_i \varepsilon_j} \tag{2.13}$$

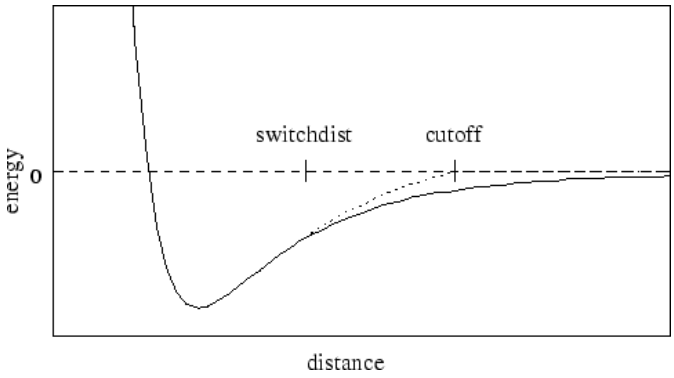

Figure 2.5. Potential energy interactions as a function of the distance between two interacting atoms.

It is important to take into account the Columbic interactions between adsorbate molecules that are polar or quadrupolar. This can be achieved using equation (2.14). To calculate point charges on the atoms contained in MOFs, density functional theory (DFT)[93] methods can be applied to calculate the electrostatic potential energy of the entire MOF before partial atomic charge assignment.

$$U_{Coul} = \sum_{i=1}^{N} \sum_{j=i+1}^{N} \frac{q_i q_j}{4\pi\varepsilon_0 r_{ij}} \tag{2.14}$$

In the equation above, ε_0 is the permittivity in vacuum, q_i and q_k are the charges on atoms *i* and *j*, respectively, and r_{ij} is the interatomic distance between atoms *i* and *j*.

GCMC simulations have been widely used to predict gas adsorption isotherms in MOFs including successful application in high-throughput calculations for gas separation,[94] gas storage,[95] and catalysis.[96] Recently, MOFs were computational screened for CO/N_2 separation using GCMC simulations.[97] This screening process identified Ni-MOF-74 and Co-MOF-74 as

the most promising adsorbent for CO/N_2 separation due to their strong metal-CO interactions. GCMC simulations have also been applied in identifying MOFs for membrane technologies in H_2 purification and CO_2 capture in syngas production.[98]

2.3.2 Periodic Boundary Condition (PBC)

In GCMC simulations, we predict macroscopic properties of a system i.e. critical properties of a fluid[99] or predicting the adsorption capacity.[100] In such simulations, the entire system can be assumed as a simulation box containing thousands of molecules as illustrated in in Figure 2.6.

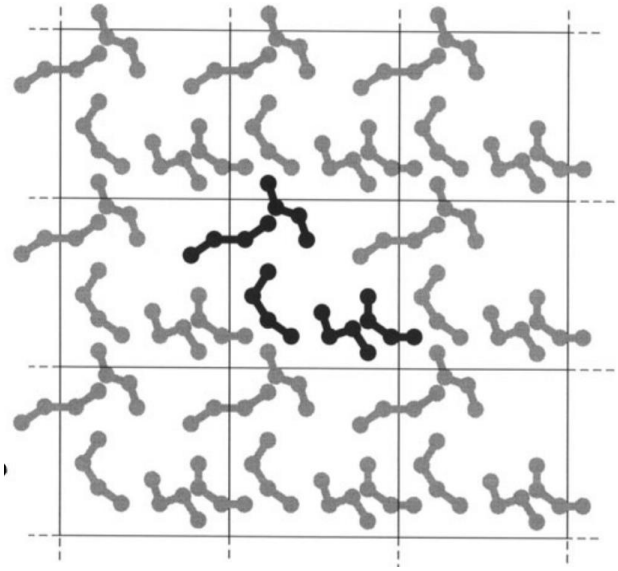

Figure 2.6. Simulation box to illustrate periodic boundary conditions in GCMC simulation. Reprint from [81]

Figure 2.6 represents a simulation box of 1 gram of water in a specific volume. It will have 3×10^{22} molecules. The key question that arises here is that how all such interactions between this many atoms are handled in the simulation box. If the simulation box is enlarged so that the system boundary includes all molecules, it will be impractical in terms of computation time and resources.

The classical way to solve the problem is to use the principle of periodic boundary conditions (PBC). In principle, PBC imposed the system in which an infinite number of unit cells are placed around the main simulation cell. PBC allows this by replicating the simulation cell throughout the phase space to form an infinite system. Here in Figure 2.6, for each unit cell, particles are free to move, not only interacting with particles in one-unit cell but with neighboring cells with identical movements during the interaction within their cut-off distance. The periodic image motion of a particle in the adjacent unit cell will be identical, which is known as the "minimum image convention" condition. According to the “minimum image convention”, particles only interact with the closest image of other particles. Using PBC

principles in combination with the "minimum image convention" requires us to determine several things in running the GCMC simulation. The first is to determine the cut-off distance to calculate the interactions between particles in the simulation box. The second is setting the simulation box dimensions at least twice the cut-off distance. This ensures that particles in a unit cell only interact with the nearest particles in the neighboring image.

2.4. High Throughput Screening (HTS) of MOFs for gas adsorption

The growing number of MOFs presents a significant prospect for the discovery of novel adsorbent materials capable of achieving gas adsorption and separation with exceptional performance. However, the extensive quantity of reported MOFs presents a significant obstacle for researchers, as it is impractical to readily identify MOFs with exceptional gas adsorption and separation capabilities for specific applications. In the context of investigating a specific gas separation application, it is necessary to consider the time-consuming nature of experimental testing and the comprehensive evaluation required to fully elucidate the performance characteristics of MOFs. Clearly, it is not feasible to evaluate the gas separation capabilities of all MOFs solely through experimental means in a time-efficient manner.

The continuous expansion of computational resources has made computations an essential tool, assuming an ever more significant role in the field of materials science and engineering. Over the course of the past twenty to twenty-five years, there has been significant computational investigations focused on the screening of MOFs for gas adsorption and separation.[101,102] High-throughput computational screening studies employ molecular simulations to effectively predict the gas adsorption and separation capabilities of large numbers of MOFs in a time-efficient manner by utilizing a MOF databases in conjunction with suitable force fields. These studies are of great value as they guide future experimental endeavours, enabling the allocation of time and resources towards the most promising materials for a specific gas adsorption and separation process.

Since 2012, there has been a notable rise in computational investigations aimed at screening MOFs for their potential in CO_2 adsorption and separation. For the first time, Wilmer et al.[103] conducted simulations to investigate the adsorption behavior of pure CO_2, N_2, and CH_4 in more than 130,000 hMOFs (hypothetical MOFs) and derived extensive structure-property relationships for the gases studied. Subsequently, they made predictions on the separation of CO_2 in various gas mixtures, such as flue gas, natural gas, and landfill gas. This study delineated distinct and well-defined structure-property relationships that were not readily

apparent in a limited dataset of MOFs. The examination of structure-property correlations can aid in the identification of crucial structural attributes that influence optimum CO_2 adsorption. Furthermore, such relationships can provide a valuable framework for guiding experimental endeavours in this field.

More recently, a subset including 51,163 hMOFs was subjected to analysis for the purpose of pre-combustion CO_2 separation, employing a genetic algorithm (GA).[104,105] This screening was able to identify the top-performing MOFs showing a superior CO_2 working capacity compared to all previously documented MOFs in the literature. A total of 581,278 distinct structures were computed for the purpose of assessing CO_2 adsorption at a pressure of 0.15 bar, the relevant pressure for post-combustion CO_2 capture. In this study, a total of 1035 derivatives originating from 23 distinct parent MOFs were discovered to have remarkable CO_2 adsorption capacities above 3.0 mmol/g.

It must be noted that H_2O is typically present in a gaseous mixture and can have detrimental impact on the efficiency of the separation due to its competitive adsorption with CO_2. The development of materials with the ability to selectively adsorb CO_2 in the presence of H_2O is a topic of considerable interest. In this context, Li et al.[106] screened 5109 CoRE-MOFs to evaluate their potential for CO_2 separation from a mixture containing CO_2, N_2, and H_2O. For this screening, Henry's constant calculation was calculated for each adsorbate. Fifteen MOFs were chosen based on the ratio of Henry's constants between CO_2 and H_2O and subjected to analysis in order to investigate the adsorption properties of a $CO_2/N_2/H_2O$ mixture. The study indicated that the screening methodology employed in this study demonstrates a satisfactory level of effectiveness in identifying MOFs that exhibit reasonably high selectivities for CO_2/H_2O and CO_2/N_2. Qiao et al.[107] screened 6013 CoRE-MOFs to evaluate their efficacy in separating CO_2 and H_2S from natural gas in a humid environment. A total of 45 top-performing MOFs were successfully identified, of which 39 possess organic linkers containing nitrogen. Specifically, 23 of these MOFs incorporate pyridine linkers, while the remaining 12 incorporate azolates. This implies that the utilisation of organic linkers is more advantageous in the context of CO_2 and H_2S separation owing to their high affinity. This study further highlights the important of the charge assignment approach in accurately identifying hydrophobic MOFs for the purpose of selectively adsorbing CO_2 in the presence of H_2O.

References

(1) Moghadam, P. Z.; Li, A.; Liu, X.-W.; Bueno-Perez, R.; Wang, S.-D.; Wiggin, S. B.; Wood, P. A.; Fairen-Jimenez, D. Targeted Classification of Metal–Organic Frameworks in the Cambridge Structural Database (CSD). *Chem. Sci.* **2020**, *11* (32), 8373–8387. https://doi.org/10.1039/D0SC01297A.

(2) Mason, J. A.; Veenstra, M.; Long, J. R. Evaluating Metal–Organic Frameworks for Natural Gas Storage. *Chem. Sci.* **2014**, *5* (1), 32–51. https://doi.org/10.1039/C3SC52633J.

(3) Trickett, C. A.; Helal, A.; Al-Maythalony, B. A.; Yamani, Z. H.; Cordova, K. E.; Yaghi, O. M. The Chemistry of Metal–Organic Frameworks for CO_2 Capture, Regeneration and Conversion. *Nat. Rev. Mater.* **2017**, *2* (8), 17045. https://doi.org/10.1038/natrevmats.2017.45.

(4) Fan, W.; Zhang, X.; Kang, Z.; Liu, X.; Sun, D. Isoreticular Chemistry within Metal–Organic Frameworks for Gas Storage and Separation. *Coord. Chem. Rev.* **2021**, *443*, 213968. https://doi.org/10.1016/j.ccr.2021.213968.

(5) Adil, K.; Belmabkhout, Y.; Pillai, R. S.; Cadiau, A.; Bhatt, P. M.; Assen, A. H.; Maurin, G.; Eddaoudi, M. Gas/Vapour Separation Using Ultra-Microporous Metal–Organic Frameworks: Insights into the Structure/Separation Relationship. *Chem. Soc. Rev.* **2017**, *46* (11), 3402–3430. https://doi.org/10.1039/C7CS00153C.

(6) Pascanu, V.; González Miera, G.; Inge, A. K.; Martín-Matute, B. Metal–Organic Frameworks as Catalysts for Organic Synthesis: A Critical Perspective. *J. Am. Chem. Soc.* **2019**, *141* (18), 7223–7234. https://doi.org/10.1021/jacs.9b00733.

(7) Cavka, J. H.; Jakobsen, S.; Olsbye, U.; Guillou, N.; Lamberti, C.; Bordiga, S.; Lillerud, K. P. A New Zirconium Inorganic Building Brick Forming Metal Organic Frameworks with Exceptional Stability. *J. Am. Chem. Soc.* **2008**, *130* (42), 13850–13851. https://doi.org/10.1021/ja8057953.

(8) He, Y.; Wang, Z.; Wang, H.; Wang, Z.; Zeng, G.; Xu, P.; Huang, D.; Chen, M.; Song, B.; Qin, H.; Zhao, Y. Metal-Organic Framework-Derived Nanomaterials in Environment Related Fields: Fundamentals, Properties and Applications. *Coord. Chem. Rev.* **2021**, *429*, 213618. https://doi.org/https://doi.org/10.1016/j.ccr.2020.213618.

(9) Li, H.; Eddaoudi, M.; O'Keeffe, M.; Yaghi, O. M. Design and Synthesis of an Exceptionally Stable and Highly Porous Metal-Organic Framework. *Nature* **1999**, *402* (6759), 276–279. https://doi.org/10.1038/46248.

(10) Vlad, A.; Zaltariov, M.-F.; Shova, S.; Novitchi, G.; Train, C.; Cazacu, M. Metal–Organic Frameworks Based on Tri- and Penta-Nuclear Manganese(Ii) Secondary Building Units Self-Assembled by a V-Shaped Silicon-Containing Dicarboxylate. *RSC Adv.* **2016**, *6* (44), 37412–37423. https://doi.org/10.1039/C6RA03969C.

(11) Wen, L.; Cheng, P.; Lin, W. Mixed-Motif Interpenetration and Cross-Linking of High-Connectivity Networks Led to Robust and Porous Metal–Organic Frameworks with High Gas Uptake Capacities. *Chem. Sci.* **2012**, *3* (7), 2288–2292. https://doi.org/10.1039/C2SC20172K.

(12) Mocanu, T.; Pop, L.; Hădade, N. D.; Shova, S.; Grosu, I.; Andruh, M. Coordination Polymers Constructed from Tetrahedral-Shaped Adamantane Tectons. *CrystEngComm* **2017**, *19* (1), 27–31. https://doi.org/10.1039/C6CE02146H.

(13) Chen, S.-S.; Qiao, R.; Sheng, L.-Q.; Yang, S.; Liu, Z.-D. Four Complexes with the Rigid Ligand 1,4-Bis(1H-Imidazol-4-Yl)Benzene and Varied Carboxylate Ligands. *Zeitschrift für Anorg. und Allg. Chemie* **2013**, *639* (10), 1808–1814. https://doi.org/https://doi.org/10.1002/zaac.201300189.

(14) Zhang, G.; Wei, G.; Liu, Z.; Oliver, S. R. J.; Fei, H. A Robust Sulfonate-Based Metal–Organic Framework with Permanent Porosity for Efficient CO_2 Capture and Conversion. *Chem. Mater.* **2016**, *28* (17), 6276–6281. https://doi.org/10.1021/acs.chemmater.6b02511.

(15) Desai, A. V; Joarder, B.; Roy, A.; Samanta, P.; Babarao, R.; Ghosh, S. K. Multifunctional Behavior of Sulfonate-Based Hydrolytically Stable Microporous Metal–Organic Frameworks. *ACS Appl. Mater. Interfaces* **2018**, *10* (45), 39049–39055. https://doi.org/10.1021/acsami.8b14420.

(16) Schütrumpf, A.; Kirpi, E.; Bulut, A.; Morel, F. L.; Ranocchiari, M.; Lork, E.; Zorlu, Y.; Grabowsky, S.; Yücesan, G.; Beckmann, J. Tetrahedral Tetraphosphonic Acids. New Building Blocks in Supramolecular Chemistry. *Cryst. Growth Des.* **2015**, *15* (10), 4925–4931. https://doi.org/10.1021/acs.cgd.5b00811.

(17) Firmino, A. D. G.; Figueira, F.; Tomé, J. P. C.; Paz, F. A. A.; Rocha, J. Metal–Organic Frameworks Assembled from Tetraphosphonic Ligands and Lanthanides. *Coord. Chem. Rev.* **2018**, *355*, 133–149. https://doi.org/https://doi.org/10.1016/j.ccr.2017.08.001.

(18) Kaye, S. S.; Dailly, A.; Yaghi, O. M.; Long, J. R. Impact of Preparation and Handling on the Hydrogen Storage Properties of Zn_4O(1,4-Benzenedicarboxylate)$_3$ (MOF-5). *J. Am. Chem. Soc.* **2007**, *129* (46), 14176–14177. https://doi.org/10.1021/ja076877g.

(19) Chae, H. K.; Siberio-Pérez, D. Y.; Kim, J.; Go, Y.; Eddaoudi, M.; Matzger, A. J.; O'Keeffe, M.; Yaghi, O. M.; Group, M. D. and D. A Route to High Surface Area, Porosity and Inclusion of Large Molecules in Crystals. *Nature* **2004**, *427* (6974), 523–527. https://doi.org/10.1038/nature02311.

(20) Furukawa, H.; Ko, N.; Go, Y. B.; Aratani, N.; Choi, S. B.; Choi, E.; Yazaydin, A. Ö.; Snurr, R. Q.; O'Keeffe, M.; Kim, J.; Yaghi, O. M. Ultrahigh Porosity in Metal-Organic Frameworks. *Science.* **2010**, *329* (5990), 424–428. https://doi.org/10.1126/science.1192160.

(21) Hong, D.-Y.; Hwang, Y. K.; Serre, C.; Férey, G.; Chang, J.-S. Porous Chromium Terephthalate MIL-101 with Coordinatively Unsaturated Sites: Surface Functionalization, Encapsulation, Sorption and Catalysis. *Adv. Funct. Mater.* **2009**, *19* (10), 1537–1552. https://doi.org/https://doi.org/10.1002/adfm.200801130.

(22) Schneemann, A.; Bon, V.; Schwedler, I.; Senkovska, I.; Kaskel, S.; Fischer, R. A. Flexible Metal–Organic Frameworks. *Chem. Soc. Rev.* **2014**, *43* (16), 6062–6096. https://doi.org/10.1039/C4CS00101J.

(23) Behera, N.; Duan, J.; Jin, W.; Kitagawa, S. The Chemistry and Applications of Flexible Porous Coordination Polymers. *EnergyChem* **2021**, *3* (6), 100067. https://doi.org/https://doi.org/10.1016/j.enchem.2021.100067.

(24) Chen, K.; Mousavi, S. H.; Singh, R.; Snurr, R. Q.; Li, G.; Webley, P. A. Gating Effect for Gas Adsorption in Microporous Materials—Mechanisms and Applications. *Chem. Soc. Rev.* **2022**, *51* (3), 1139–1166. https://doi.org/10.1039/D1CS00822F.

(25) Dong, Q.; Zhang, X.; Liu, S.; Lin, R.-B.; Guo, Y.; Ma, Y.; Yonezu, A.; Krishna, R.; Liu, G.; Duan, J.; Matsuda, R.; Jin, W.; Chen, B. Tuning Gate-Opening of a Flexible Metal–Organic Framework for Ternary Gas Sieving Separation. *Angew. Chemie Int. Ed.* **2020**, *59* (50), 22756–22762. https://doi.org/https://doi.org/10.1002/anie.202011802.

(26) Giacobbe, C.; Lavigna, E.; Maspero, A.; Galli, S. Elucidating the CO_2 Adsorption Mechanisms in the Triangular Channels of the Bis(Pyrazolate) MOF Fe_2(BPEB)$_3$ by in Situ Synchrotron X-Ray Diffraction and Molecular Dynamics Simulations. *J. Mater. Chem. A* **2017**, *5* (32), 16964–16975. https://doi.org/10.1039/C7TA04501H.

(27) Bönisch, N.; Maliuta, M.; Senkovska, I.; Bon, V.; Petkov, P.; Plätzer, C.; Müller, P.; Kaskel, S. Linker Expansion and Its Impact on Switchability in Pillared-Layer MOFs. *Inorg. Chem.* **2021**, *60* (3), 1726–1737. https://doi.org/10.1021/acs.inorgchem.0c03218.

(28) Kavoosi, N.; Bon, V.; Senkovska, I.; Krause, S.; Atzori, C.; Bonino, F.; Pallmann, J.; Paasch, S.; Brunner, E.; Kaskel, S. Tailoring Adsorption Induced Phase Transitions in the Pillared-Layer Type Metal–Organic Framework DUT-8(Ni). *Dalt. Trans.* **2017**, *46* (14), 4685–4695. https://doi.org/10.1039/C7DT00015D.

(29) Serre, C.; Millange, F.; Thouvenot, C.; Noguès, M.; Marsolier, G.; Louër, D.; Férey, G. Very Large Breathing Effect in the First Nanoporous Chromium(III)-Based Solids: MIL-53 or CrIII(OH)·{$O_2C-C_6H_4-CO_2$}·{$HO_2C-C_6H_4-CO_2H$}x·H_2Oy. *J. Am. Chem. Soc.* **2002**, *124* (45), 13519–13526. https://doi.org/10.1021/ja0276974.

(30) Spencer, E. C.; Kiran, M. S. R. N.; Li, W.; Ramamurty, U.; Ross, N. L.; Cheetham, A. K. Pressure-Induced Bond Rearrangement and Reversible Phase Transformation in a Metal–Organic Framework. *Angew. Chemie Int. Ed.* **2014**, *53* (22), 5583–5586. https://doi.org/https://doi.org/10.1002/anie.201310276.

(31) Ortiz, A. U.; Boutin, A.; Gagnon, K. J.; Clearfield, A.; Coudert, F.-X. Remarkable Pressure Responses of Metal–Organic Frameworks: Proton Transfer and Linker Coiling in Zinc Alkyl Gates. *J. Am. Chem. Soc.* **2014**, *136* (32), 11540–11545. https://doi.org/10.1021/ja5060059.

(32) Wharmby, M. T.; Henke, S.; Bennett, T. D.; Bajpe, S. R.; Schwedler, I.; Thompson, S. P.; Gozzo, F.; Simoncic, P.; Mellot-Draznieks, C.; Tao, H.; Yue, Y.; Cheetham, A. K. Extreme Flexibility in a Zeolitic Imidazolate Framework: Porous to Dense Phase Transition in Desolvated ZIF-4. *Angew. Chemie Int. Ed.* **2015**, *54* (22), 6447–6451. https://doi.org/https://doi.org/10.1002/anie.201410167.

(33) Gücüyener, C.; van den Bergh, J.; Gascon, J.; Kapteijn, F. Ethane/Ethene Separation Turned on Its Head: Selective Ethane Adsorption on the Metal−Organic Framework ZIF-7 through a Gate-Opening Mechanism. *J. Am. Chem. Soc.* **2010**, *132* (50), 17704–17706. https://doi.org/10.1021/ja1089765.

(34) Zhao, P.; Lampronti, G. I.; Lloyd, G. O.; Suard, E.; Redfern, S. A. T. Direct Visualisation of Carbon Dioxide Adsorption in Gate-Opening Zeolitic Imidazolate Framework ZIF-7. *J. Mater. Chem. A* **2014**, *2* (3), 620–623. https://doi.org/10.1039/C3TA13981F.

(35) Fernandez, C. A.; Thallapally, P. K.; McGrail, B. P. Insights into the Temperature-Dependent “Breathing” of a Flexible Fluorinated Metal–Organic Framework.

ChemPhysChem **2012**, *13* (14), 3275–3281. https://doi.org/https://doi.org/10.1002/cphc.201200243.

(36) Chui, S. S.-Y.; Lo, S. M.-F.; Charmant, J. P. H.; Orpen, A. G.; Williams, I. D. A Chemically Functionalizable Nanoporous Material $[Cu_3(TMA)_2(H_2O)_3]N$. *Science.* **1999**, *283* (5405), 1148–1150. https://doi.org/10.1126/science.283.5405.1148.

(37) Eddaoudi, M.; Li, H.; Yaghi, O. M. Highly Porous and Stable Metal−Organic Frameworks: Structure Design and Sorption Properties. *J. Am. Chem. Soc.* **2000**, *122* (7), 1391–1397. https://doi.org/10.1021/ja9933386.

(38) García, E. J.; Mowat, J. P. S.; Wright, P. A.; Pérez-Pellitero, J.; Jallut, C.; Pirngruber, G. D. Role of Structure and Chemistry in Controlling Separations of CO_2/CH_4 and CO_2/CH_4/CO Mixtures over Honeycomb MOFs with Coordinatively Unsaturated Metal Sites. *J. Phys. Chem. C* **2012**, *116* (50), 26636–26648. https://doi.org/10.1021/jp309526k.

(39) Zhang, Z.; Zhao, Y.; Gong, Q.; Li, Z.; Li, J. MOFs for CO_2 Capture and Separation from Flue Gas Mixtures: The Effect of Multifunctional Sites on Their Adsorption Capacity and Selectivity. *Chem. Commun.* **2013**, *49* (7), 653–661. https://doi.org/10.1039/C2CC35561B.

(40) Dietzel, P. D. C.; Blom, R.; Fjellvåg, H. Base-Induced Formation of Two Magnesium Metal-Organic Framework Compounds with a Bifunctional Tetratopic Ligand. *Eur. J. Inorg. Chem.* **2008**, *2008* (23), 3624–3632. https://doi.org/https://doi.org/10.1002/ejic.200701284.

(41) Fetisov, E. O.; Shah, M. S.; Long, J. R.; Tsapatsis, M.; Siepmann, J. I. First Principles Monte Carlo Simulations of Unary and Binary Adsorption: CO_2, N_2, and H_2O in Mg-MOF-74. *Chem. Commun.* **2018**, *54* (77), 10816–10819. https://doi.org/10.1039/C8CC06178E.

(42) Wu, H.; Simmons, J. M.; Srinivas, G.; Zhou, W.; Yildirim, T. Adsorption Sites and Binding Nature of CO_2 in Prototypical Metal−Organic Frameworks: A Combined Neutron Diffraction and First-Principles Study. *J. Phys. Chem. Lett.* **2010**, *1* (13), 1946–1951. https://doi.org/10.1021/jz100558r.

(43) Queen, W. L.; Hudson, M. R.; Bloch, E. D.; Mason, J. A.; Gonzalez, M. I.; Lee, J. S.; Gygi, D.; Howe, J. D.; Lee, K.; Darwish, T. A.; James, M.; Peterson, V. K.; Teat, S. J.; Smit, B.; Neaton, J. B.; Long, J. R.; Brown, C. M. Comprehensive Study of Carbon Dioxide Adsorption in the Metal–Organic Frameworks M_2(Dobdc) (M = Mg, Mn, Fe,

Co, Ni, Cu, Zn). *Chem. Sci.* **2014**, *5* (12), 4569–4581. https://doi.org/10.1039/C4SC02064B.

(44) Kim, H.; Sohail, M.; Yim, K.; Park, Y. C.; Chun, D. H.; Kim, H. J.; Han, S. O.; Moon, J.-H. Effective CO_2 and CO Separation Using [M_2(DOBDC)] (M = Mg, Co, Ni) with Unsaturated Metal Sites and Excavation of Their Adsorption Sites. *ACS Appl. Mater. Interfaces* **2019**, *11* (7), 7014–7021. https://doi.org/10.1021/acsami.8b20450.

(45) Kong, X.; Scott, E.; Ding, W.; Mason, J. A.; Long, J. R.; Reimer, J. A. CO_2 Dynamics in a Metal–Organic Framework with Open Metal Sites. *J. Am. Chem. Soc.* **2012**, *134* (35), 14341–14344. https://doi.org/10.1021/ja306822p.

(46) Du, M.; Li, L.; Li, M.; Si, R. Adsorption Mechanism on Metal Organic Frameworks of Cu-BTC, Fe-BTC and ZIF-8 for CO_2 Capture Investigated by X-Ray Absorption Fine Structure. *RSC Adv.* **2016**, *6* (67), 62705–62716. https://doi.org/10.1039/C6RA07582G.

(47) Wang, H.-H.; Hou, L.; Li, Y.-Z.; Jiang, C.-Y.; Wang, Y.-Y.; Zhu, Z. Porous MOF with Highly Efficient Selectivity and Chemical Conversion for CO_2. *ACS Appl. Mater. Interfaces* **2017**, *9* (21), 17969–17976. https://doi.org/10.1021/acsami.7b03835.

(48) Couck, S.; Denayer, J. F. M.; Baron, G. V; Rémy, T.; Gascon, J.; Kapteijn, F. An Amine-Functionalized MIL-53 Metal−Organic Framework with Large Separation Power for CO2 and CH4. *J. Am. Chem. Soc.* **2009**, *131* (18), 6326–6327. https://doi.org/10.1021/ja900555r.

(49) Arstad, B.; Fjellvåg, H.; Kongshaug, K. O.; Swang, O.; Blom, R. Amine Functionalised Metal Organic Frameworks (MOFs) as Adsorbents for Carbon Dioxide. *Adsorption* **2008**, *14* (6), 755–762. https://doi.org/10.1007/s10450-008-9137-6.

(50) Su, X.; Bromberg, L.; Martis, V.; Simeon, F.; Huq, A.; Hatton, T. A. Postsynthetic Functionalization of Mg-MOF-74 with Tetraethylenepentamine: Structural Characterization and Enhanced CO_2 Adsorption. *ACS Appl. Mater. Interfaces* **2017**, *9* (12), 11299–11306. https://doi.org/10.1021/acsami.7b02471.

(51) Moreau, F.; da Silva, I.; Al Smail, N. H.; Easun, T. L.; Savage, M.; Godfrey, H. G. W.; Parker, S. F.; Manuel, P.; Yang, S.; Schröder, M. Unravelling Exceptional Acetylene and Carbon Dioxide Adsorption within a Tetra-Amide Functionalized Metal-Organic Framework. *Nat. Commun.* **2017**, *8* (1), 14085. https://doi.org/10.1038/ncomms14085.

(52) Fang, Z.; Bueken, B.; De Vos, D. E.; Fischer, R. A. Defect-Engineered Metal–Organic Frameworks. *Angew. Chemie Int. Ed.* **2015**, *54* (25), 7234–7254. https://doi.org/https://doi.org/10.1002/anie.201411540.

(53) Chong, S.; Thiele, G.; Kim, J. Excavating Hidden Adsorption Sites in Metal-Organic Frameworks Using Rational Defect Engineering. *Nat. Commun.* **2017**, *8* (1), 1539. https://doi.org/10.1038/s41467-017-01478-4.

(54) Kim, S.-Y.; Kim, A.-R.; Yoon, J. W.; Kim, H.-J.; Bae, Y.-S. Creation of Mesoporous Defects in a Microporous Metal-Organic Framework by an Acetic Acid-Fragmented Linker Co-Assembly and Its Remarkable Effects on Methane Uptake. *Chem. Eng. J.* **2018**, *335*, 94–100. https://doi.org/https://doi.org/10.1016/j.cej.2017.10.078.

(55) Rodríguez-Albelo, L. M.; López-Maya, E.; Hamad, S.; Ruiz-Salvador, A. R.; Calero, S.; Navarro, J. A. R. Selective Sulfur Dioxide Adsorption on Crystal Defect Sites on an Isoreticular Metal Organic Framework Series. *Nat. Commun.* **2017**, *8* (1), 14457. https://doi.org/10.1038/ncomms14457.

(56) Ji, Z.; Wang, H.; Canossa, S.; Wuttke, S.; Yaghi, O. M. Pore Chemistry of Metal–Organic Frameworks. *Adv. Funct. Mater.* **2020**, *30* (41), 2000238. https://doi.org/https://doi.org/10.1002/adfm.202000238.

(57) Erkartal, M.; Sen, U. Boronic Acid Moiety as Functional Defect in UiO-66 and Its Effect on Hydrogen Uptake Capacity and Selective CO_2 Adsorption: A Comparative Study. *ACS Appl. Mater. Interfaces* **2018**, *10* (1), 787–795. https://doi.org/10.1021/acsami.7b16937.

(58) Jiao, C.; Majeed, Z.; Wang, G.-H.; Jiang, H. A Nanosized Metal–Organic Framework Confined inside a Functionalized Mesoporous Polymer: An Efficient CO_2 Adsorbent with Metal Defects. *J. Mater. Chem. A* **2018**, *6* (35), 17220–17226. https://doi.org/10.1039/C8TA05323E.

(59) Teplensky, M. H.; Fantham, M.; Li, P.; Wang, T. C.; Mehta, J. P.; Young, L. J.; Moghadam, P. Z.; Hupp, J. T.; Farha, O. K.; Kaminski, C. F.; Fairen-Jimenez, D. Temperature Treatment of Highly Porous Zirconium-Containing Metal–Organic Frameworks Extends Drug Delivery Release. *J. Am. Chem. Soc.* **2017**, *139* (22), 7522–7532. https://doi.org/10.1021/jacs.7b01451.

(60) Brunauer, S.; Emmett, P. H.; Teller, E. Adsorption of Gases in Multimolecular Layers. *J. Am. Chem. Soc.* **1938**, *60* (2), 309–319. https://doi.org/10.1021/ja01269a023.

(61) Gómez-Gualdrón, D. A.; Moghadam, P. Z.; Hupp, J. T.; Farha, O. K.; Snurr, R. Q. Application of Consistency Criteria To Calculate BET Areas of Micro- And Mesoporous Metal–Organic Frameworks. *J. Am. Chem. Soc.* **2016**, *138* (1), 215–224. https://doi.org/10.1021/jacs.5b10266.

(62) Rouquerol, J.; Llewellyn, P.; Rouquerol, F. Is the Bet Equation Applicable to Microporous Adsorbents? In *Characterization of Porous Solids VII*; Llewellyn, P. L., Rodriquez-Reinoso, F., Rouqerol, J., Seaton, N. B. T.-S. in S. S. and C., Eds.; Elsevier, 2007; Vol. 160, pp 49–56. https://doi.org/10.1016/S0167-2991(07)80008-5.

(63) Osterrieth, J. W. M.; Rampersad, J.; Madden, D.; Rampal, N.; Skoric, L.; Connolly, B.; Allendorf, M. D.; Stavila, V.; Snider, J. L.; Ameloot, R.; Marreiros, J.; Ania, C.; Azevedo, D.; Vilarrasa-Garcia, E.; Santos, B. F.; Bu, X.-H.; Chang, Z.; Bunzen, H.; Champness, N. R.; Griffin, S. L.; Chen, B.; Lin, R.-B.; Coasne, B.; Cohen, S.; Moreton, J. C.; Colón, Y. J.; Chen, L.; Clowes, R.; Coudert, F.-X.; Cui, Y.; Hou, B.; D'Alessandro, D. M.; Doheny, P. W.; Dincă, M.; Sun, C.; Doonan, C.; Huxley, M. T.; Evans, J. D.; Falcaro, P.; Ricco, R.; Farha, O.; Idrees, K. B.; Islamoglu, T.; Feng, P.; Yang, H.; Forgan, R. S.; Bara, D.; Furukawa, S.; Sanchez, E.; Gascon, J.; Telalović, S.; Ghosh, S. K.; Mukherjee, S.; Hill, M. R.; Sadiq, M. M.; Horcajada, P.; Salcedo-Abraira, P.; Kaneko, K.; Kukobat, R.; Kenvin, J.; Keskin, S.; Kitagawa, S.; Otake, K.; Lively, R. P.; DeWitt, S. J. A.; Llewellyn, P.; Lotsch, B. V; Emmerling, S. T.; Pütz, A. M.; Martí-Gastaldo, C.; Padial, N. M.; García-Martínez, J.; Linares, N.; Maspoch, D.; Suárez del Pino, J. A.; Moghadam, P.; Oktavian, R.; Morris, R. E.; Wheatley, P. S.; Navarro, J.; Petit, C.; Danaci, D.; Rosseinsky, M. J.; Katsoulidis, A. P.; Schröder, M.; Han, X.; Yang, S.; Serre, C.; Mouchaham, G.; Sholl, D. S.; Thyagarajan, R.; Siderius, D.; Snurr, R. Q.; Goncalves, R. B.; Telfer, S.; Lee, S. J.; Ting, V. P.; Rowlandson, J. L.; Uemura, T.; Iiyuka, T.; van der Veen, M. A.; Rega, D.; Van Speybroeck, V.; Rogge, S. M. J.; Lamaire, A.; Walton, K. S.; Bingel, L. W.; Wuttke, S.; Andreo, J.; Yaghi, O.; Zhang, B.; Yavuz, C. T.; Nguyen, T. S.; Zamora, F.; Montoro, C.; Zhou, H.; Kirchon, A.; Fairen-Jimenez, D. How Reproducible Are Surface Areas Calculated from the BET Equation? *Adv. Mater.* **2022**, *34* (27), 2201502. https://doi.org/10.1002/adma.202201502.

(64) Alezi, D.; Belmabkhout, Y.; Suyetin, M.; Bhatt, P. M.; Weseliński, Ł. J.; Solovyeva, V.; Adil, K.; Spanopoulos, I.; Trikalitis, P. N.; Emwas, A.-H.; Eddaoudi, M. MOF Crystal Chemistry Paving the Way to Gas Storage Needs: Aluminum-Based Soc-MOF for CH_4, O_2, and CO_2 Storage. *J. Am. Chem. Soc.* **2015**, *137* (41), 13308–13318. https://doi.org/10.1021/jacs.5b07053.

(65) Allendorf, M. D.; Stavila, V.; Snider, J. L.; Witman, M.; Bowden, M. E.; Brooks, K.; Tran, B. L.; Autrey, T. Challenges to Developing Materials for the Transport and Storage

of Hydrogen. *Nat. Chem.* **2022**, *14* (11), 1214–1223. https://doi.org/10.1038/s41557-022-01056-2.

(66) Park, K. M.; Kim, H.; Murray, J.; Koo, J.; Kim, K. A Facile Preparation Method for Nanosized MOFs as a Multifunctional Material for Cellular Imaging and Drug Delivery. *Supramol. Chem.* **2017**, *29* (6), 441–445. https://doi.org/10.1080/10610278.2016.1266359.

(67) Konnerth, H.; Matsagar, B. M.; Chen, S. S.; Prechtl, M. H. G.; Shieh, F.-K.; Wu, K. C.-W. Metal-Organic Framework (MOF)-Derived Catalysts for Fine Chemical Production. *Coord. Chem. Rev.* **2020**, *416*, 213319. https://doi.org/https://doi.org/10.1016/j.ccr.2020.213319.

(68) Shrivastav, V.; Sundriyal, S.; Goel, P.; Kaur, H.; Tuteja, S. K.; Vikrant, K.; Kim, K.-H.; Tiwari, U. K.; Deep, A. Metal-Organic Frameworks (MOFs) and Their Composites as Electrodes for Lithium Battery Applications: Novel Means for Alternative Energy Storage. *Coord. Chem. Rev.* **2019**, *393*, 48–78. https://doi.org/https://doi.org/10.1016/j.ccr.2019.05.006.

(69) Yan, J.; Liu, T.; Liu, X.; Yan, Y.; Huang, Y. Metal-Organic Framework-Based Materials for Flexible Supercapacitor Application. *Coord. Chem. Rev.* **2022**, *452*, 214300. https://doi.org/https://doi.org/10.1016/j.ccr.2021.214300.

(70) Lawson, H. D.; Walton, S. P.; Chan, C. Metal–Organic Frameworks for Drug Delivery: A Design Perspective. *ACS Appl. Mater. Interfaces* **2021**, *13* (6), 7004–7020. https://doi.org/10.1021/acsami.1c01089.

(71) Yan, Y.; Lin, X.; Yang, S.; Blake, A. J.; Dailly, A.; Champness, N. R.; Hubberstey, P.; Schröder, M. Exceptionally High H2storage by a Metal–Organic Polyhedral Framework. *Chem. Commun.* **2009**, No. 9, 1025–1027. https://doi.org/10.1039/B900013E.

(72) Farha, O. K.; Wilmer, C. E.; Eryazici, I.; Hauser, B. G.; Parilla, P. A.; O'Neill, K.; Sarjeant, A. A.; Nguyen, S. T.; Snurr, R. Q.; Hupp, J. T. Designing Higher Surface Area Metal–Organic Frameworks: Are Triple Bonds Better Than Phenyls? *J. Am. Chem. Soc.* **2012**, *134* (24), 9860–9863. https://doi.org/10.1021/ja302623w.

(73) Farha, O. K.; Özgür Yazaydın, A.; Eryazici, I.; Malliakas, C. D.; Hauser, B. G.; Kanatzidis, M. G.; Nguyen, S. T.; Snurr, R. Q.; Hupp, J. T. De Novo Synthesis of a Metal–Organic Framework Material Featuring Ultrahigh Surface Area and Gas Storage Capacities. *Nat. Chem.* **2010**, *2* (11), 944–948. https://doi.org/10.1038/nchem.834.

(74) Yuan, D.; Zhao, D.; Sun, D.; Zhou, H.-C. An Isoreticular Series of Metal–Organic Frameworks with Dendritic Hexacarboxylate Ligands and Exceptionally High Gas-Uptake Capacity. *Angew. Chemie Int. Ed.* **2010**, *49* (31), 5357–5361. https://doi.org/https://doi.org/10.1002/anie.201001009.

(75) Kapelewski, M. T.; Runčevski, T.; Tarver, J. D.; Jiang, H. Z. H.; Hurst, K. E.; Parilla, P. A.; Ayala, A.; Gennett, T.; FitzGerald, S. A.; Brown, C. M.; Long, J. R. Record High Hydrogen Storage Capacity in the Metal–Organic Framework Ni_2(m-Dobdc) at Near-Ambient Temperatures. *Chem. Mater.* **2018**, *30* (22), 8179–8189. https://doi.org/10.1021/acs.chemmater.8b03276.

(76) Kondo, M.; Yoshitomi, T.; Matsuzaka, H.; Kitagawa, S.; Seki, K. Three-Dimensional Framework with Channeling Cavities for Small Molecules: {[M_2(4, 4′-Bpy)$_3$(NO_3)$_4$]·xH_2O}n (M : Co, Ni, Zn). *Angew. Chemie Int. Ed. English* **1997**, *36* (16), 1725–1727. https://doi.org/https://doi.org/10.1002/anie.199717251.

(77) Eddaoudi, M.; Kim, J.; Rosi, N.; Vodak, D.; Wachter, J.; O'Keeffe, M.; Yaghi, O. M. Systematic Design of Pore Size and Functionality in Isoreticular MOFs and Their Application in Methane Storage. *Science.* **2002**, *295* (5554), 469–472. https://doi.org/10.1126/science.1067208.

(78) Li, B.; Wen, H.-M.; Zhou, W.; Chen, B. Porous Metal–Organic Frameworks for Gas Storage and Separation: What, How, and Why? *J. Phys. Chem. Lett.* **2014**, *5* (20), 3468–3479. https://doi.org/10.1021/jz501586e.

(79) Peng, Y.; Krungleviciute, V.; Eryazici, I.; Hupp, J. T.; Farha, O. K.; Yildirim, T. Methane Storage in Metal–Organic Frameworks: Current Records, Surprise Findings, and Challenges. *J. Am. Chem. Soc.* **2013**, *135* (32), 11887–11894. https://doi.org/10.1021/ja4045289.

(80) Wen, H.-M.; Li, B.; Li, L.; Lin, R.-B.; Zhou, W.; Qian, G.; Chen, B. A Metal–Organic Framework with Optimized Porosity and Functional Sites for High Gravimetric and Volumetric Methane Storage Working Capacities. *Adv. Mater.* **2018**, *30* (16), 1704792. https://doi.org/https://doi.org/10.1002/adma.201704792.

(81) Li, L.; Jung, H. S.; Lee, J. W.; Kang, Y. T. Review on Applications of Metal–Organic Frameworks for CO_2 Capture and the Performance Enhancement Mechanisms. *Renew. Sustain. Energy Rev.* **2022**, *162*, 112441. https://doi.org/https://doi.org/10.1016/j.rser.2022.112441.

(82) Li, H.; Eddaoudi, M.; Groy, T. L.; Yaghi, O. M. Establishing Microporosity in Open Metal−Organic Frameworks: Gas Sorption Isotherms for Zn(BDC) (BDC = 1,4-Benzenedicarboxylate). *J. Am. Chem. Soc.* **1998**, *120* (33), 8571–8572. https://doi.org/10.1021/ja981669x.

(83) Millward, A. R.; Yaghi, O. M. Metal−Organic Frameworks with Exceptionally High Capacity for Storage of Carbon Dioxide at Room Temperature. *J. Am. Chem. Soc.* **2005**, *127* (51), 17998–17999. https://doi.org/10.1021/ja0570032.

(84) Llewellyn, P. L.; Bourrelly, S.; Serre, C.; Vimont, A.; Daturi, M.; Hamon, L.; De Weireld, G.; Chang, J.-S.; Hong, D.-Y.; Kyu Hwang, Y.; Hwa Jhung, S.; Férey, G. High Uptakes of CO_2 and CH_4 in Mesoporous Metal—Organic Frameworks MIL-100 and MIL-101. *Langmuir* **2008**, *24* (14), 7245–7250. https://doi.org/10.1021/la800227x.

(85) Caskey, S. R.; Wong-Foy, A. G.; Matzger, A. J. Dramatic Tuning of Carbon Dioxide Uptake via Metal Substitution in a Coordination Polymer with Cylindrical Pores. *J. Am. Chem. Soc.* **2008**, *130* (33), 10870–10871. https://doi.org/10.1021/ja8036096.

(86) Banerjee, R.; Phan, A.; Wang, B.; Knobler, C.; Furukawa, H.; O'Keeffe, M.; Yaghi, O. M. High-Throughput Synthesis of Zeolitic Imidazolate Frameworks and Application to CO_2 Capture. *Science.* **2008**, *319* (5865), 939 LP – 943. https://doi.org/10.1126/science.1152516.

(87) Dubbeldam, D.; Calero, S.; Vlugt, T. J. H.; Snurr, R. Q. Molecular Simulations of Adsorption and Diffusion in Crystalline Nanoporous Materials. In *Handbook of Porous Materials*; Materials and Energy; WORLD SCIENTIFIC, 2021; Vol. Volume 16, pp 199–319. https://doi.org/10.1142/9789811223396_0004.

(88) Rappé, A. K.; Casewit, C. J.; Colwell, K. S.; Goddard, W. A.; Skiff, W. M. UFF, a Full Periodic Table Force Field for Molecular Mechanics and Molecular Dynamics Simulations. *J. Am. Chem. Soc.* **1992**. https://doi.org/10.1021/ja00051a040.

(89) Mayo, S. L.; Olafson, B. D.; Goddard, W. A. DREIDING: A Generic Force Field for Molecular Simulations. *J. Phys. Chem.* **1990**, *94* (26), 8897–8909. https://doi.org/10.1021/j100389a010.

(90) Schwerdtfeger, P.; Wales, D. J. 100 Years of the Lennard-Jones Potential. *J. Chem. Theory Comput.* **2024**, *20* (9), 3379–3405. https://doi.org/10.1021/acs.jctc.4c00135.

(91) Potoff, J. J.; Siepmann, J. I. Vapor–Liquid Equilibria of Mixtures Containing Alkanes, Carbon Dioxide, and Nitrogen. *AIChE J.* **2001**, *47* (7), 1676–1682. https://doi.org/10.1002/aic.690470719.

(92) Jorgensen, W. L.; Chandrasekhar, J.; Madura, J. D.; Impey, R. W.; Klein, M. L. Comparison of Simple Potential Functions for Simulating Liquid Water. *J. Chem. Phys.* **1983**, *79* (2), 926–935. https://doi.org/10.1063/1.445869.

(93) Sholl, D. S.; Steckel, J. A. *Density Functional Theory*; John Wiley & Sons, Inc.: Hoboken, NJ, USA, 2009. https://doi.org/10.1002/9780470447710.

(94) Altintas, C.; Keskin, S. Computational Screening of MOFs for C_2H_6/C_2H_4 and C2H6/CH4 Separations. *Chem. Eng. Sci.* **2016**, *139*, 49–60. https://doi.org/https://doi.org/10.1016/j.ces.2015.09.019.

(95) Bobbitt, N. S.; Snurr, R. Q. Molecular Modelling and Machine Learning for High-Throughput Screening of Metal-Organic Frameworks for Hydrogen Storage. *Mol. Simul.* **2019**, *45* (14–15), 1069–1081. https://doi.org/10.1080/08927022.2019.1597271.

(96) Rogge, S. M. J.; Bavykina, A.; Hajek, J.; Garcia, H.; Olivos-Suarez, A. I.; Sepúlveda-Escribano, A.; Vimont, A.; Clet, G.; Bazin, P.; Kapteijn, F.; Daturi, M.; Ramos-Fernandez, E. V; Llabrés i Xamena, F. X.; Van Speybroeck, V.; Gascon, J. Metal–Organic and Covalent Organic Frameworks as Single-Site Catalysts. *Chem. Soc. Rev.* **2017**, *46* (11), 3134–3184. https://doi.org/10.1039/C7CS00033B.

(97) Evans, A. D.; Cummings, M. S.; Luebke, R.; Brown, M. S.; Favero, S.; Attfield, M. P.; Siperstein, F.; Fairen-Jimenez, D.; Hellgardt, K.; Purves, R.; Law, D.; Petit, C. Screening Metal–Organic Frameworks for Dynamic CO/N_2 Separation Using Complementary Adsorption Measurement Techniques. *Ind. Eng. Chem. Res.* **2019**, *58* (39), 18336–18344. https://doi.org/10.1021/acs.iecr.9b03724.

(98) Avci, G.; Velioglu, S.; Keskin, S. High-Throughput Screening of MOF Adsorbents and Membranes for H_2 Purification and CO_2 Capture. *ACS Appl. Mater. Interfaces* **2018**, *10* (39), 33693–33706. https://doi.org/10.1021/acsami.8b12746.

(99) Chakraborti, T.; Adhikari, J. Phase Equilibria and Critical Point Predictions of Mixtures of Molecular Fluids Using Grand Canonical Transition Matrix Monte Carlo. *Ind. Eng. Chem. Res.* **2017**, *56* (22), 6520–6534. https://doi.org/10.1021/acs.iecr.7b01114.

(100) Ungerer, P.; Tavitian, B.; Boutin, A. *Applications of Molecular Simulation in the Oil and Gas Industry: Monte Carlo Methods*; IFP publications; Editions Technip, 2005.

(101) Yu, J.; Xie, L.-H.; Li, J.-R.; Ma, Y.; Seminario, J. M.; Balbuena, P. B. CO_2 Capture and Separations Using MOFs: Computational and Experimental Studies. *Chem. Rev.* **2017**, *117* (14), 9674–9754. https://doi.org/10.1021/acs.chemrev.6b00626.

(102) Daglar, H.; Keskin, S. Recent Advances, Opportunities, and Challenges in High-Throughput Computational Screening of MOFs for Gas Separations. *Coord. Chem. Rev.* **2020**, *422*, 213470. https://doi.org/https://doi.org/10.1016/j.ccr.2020.213470.

(103) Wilmer, C. E.; Farha, O. K.; Bae, Y.-S.; Hupp, J. T.; Snurr, R. Q. Structure–Property Relationships of Porous Materials for Carbon Dioxide Separation and Capture. *Energy Environ. Sci.* **2012**, *5* (12), 9849–9856. https://doi.org/10.1039/C2EE23201D.

(104) Chung, Y. G.; Gómez-Gualdrón, D. A.; Li, P.; Leperi, K. T.; Deria, P.; Zhang, H.; Vermeulen, N. A.; Stoddart, J. F.; You, F.; Hupp, J. T.; Farha, O. K.; Snurr, R. Q. In Silico Discovery of Metal-Organic Frameworks for Precombustion CO_2 Capture Using a Genetic Algorithm. *Sci. Adv.* **2023**, *2* (10), e1600909. https://doi.org/10.1126/sciadv.1600909.

(105) Collins, S. P.; Daff, T. D.; Piotrkowski, S. S.; Woo, T. K. Materials Design by Evolutionary Optimization of Functional Groups in Metal-Organic Frameworks. *Sci. Adv.* **2023**, *2* (11), e1600954. https://doi.org/10.1126/sciadv.1600954.

(106) Li, S.; Chung, Y. G.; Snurr, R. Q. High-Throughput Screening of Metal–Organic Frameworks for CO_2 Capture in the Presence of Water. *Langmuir* **2016**, *32* (40), 10368–10376. https://doi.org/10.1021/acs.langmuir.6b02803.

(107) Qiao, Z.; Xu, Q.; Jiang, J. Computational Screening of Hydrophobic Metal–Organic Frameworks for the Separation of H_2S and CO_2 from Natural Gas. *J. Mater. Chem. A* **2018**, *6* (39), 18898–18905. https://doi.org/10.1039/C8TA04939D.

ACS APPLIED MATERIALS & INTERFACES

www.acsami.org Research Article

3. Computational Characterization of Zirconium Oxide Metal Organic Frameworks (MOFs) for Adsorption Applications

Rama Oktavian[a], Raymond Schireman[b], Lawson T. Glasby[a], Guanming Huang[a], Federica Zanca[a], David Fairen-Jimenez[c], Michael T. Ruggiero[b], and Peyman Z. Moghadam[a,d]*

[a]Department of Chemical and Biological Engineering, The University of Sheffield, Sheffield S1 3JD, U.K.
[b]Department of Chemistry, University of Vermont, Burlington, Vermont 05405, United States.
[c]Department of Chemical Engineering & Biotechnology, University of Cambridge, Philippa Fawcett Drive, Cambridge CB3 0AS, U.K.
[d]Department of Chemical Engineering, University College London, London WC1E 7JE, U.K.

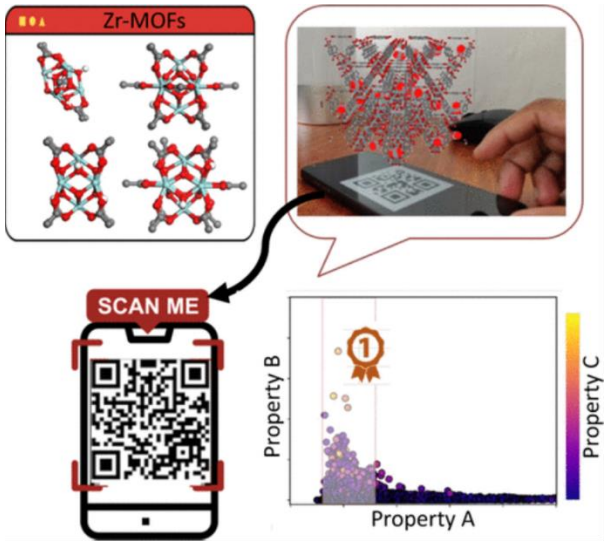

Published in ACS Appl. Mater. Interfaces 2022, 14, 51, 56938–56947

https://doi.org/10.1021/acsami.2c13391

Student's contribution: Performing simulation and calculation for geometric characterization of Zr-oxide MOFs including largest cavity diameter (LCD) and surface area. Calculating the amount of CO_2 adsorbed in Zr-oxide MOFs subset in high throughput fashion as well as the analysis of structure-property relationships.

Chapter 3

Abstract

Zr-oxide secondary building units construct metal–organic framework (MOF) materials with excellent gas adsorption properties and high mechanical, thermal, and chemical stability. These attributes have led Zr-oxide MOFs to be well-recognized for a wide range of applications, including gas storage and separation, catalysis, as well as healthcare domain. Here, we report structure search methods within the Cambridge Structural Database (CSD) to create a curated subset of 102 Zr-oxide MOFs synthesized to date, bringing a unique record for all researchers working in this area. For the identified structures, we manually corrected the proton topology of hydroxyl and water molecules on the Zr-oxide nodes and characterized their textural properties, Brunauer–Emmett–Teller (BET) area, and topology. Importantly, we performed systematic periodic density functional theory (DFT) calculations comparing 25 different combinations of basis sets and functionals to calculate framework partial atomic charges for use in gas adsorption simulations. Through experimental verification of CO_2 adsorption in selected Zr-oxide MOFs, we demonstrate the sensitivity of CO_2 adsorption predictions at the Henry's regime to the choice of the DFT method for partial charge calculations. We characterized Zr-MOFs for their CO_2 adsorption performance via high-throughput grand canonical Monte Carlo (GCMC) simulations and revealed how the chemistry of the Zr-oxide node could have a significant impact on CO_2 uptake predictions. We found that the maximum CO_2 uptake is obtained for structures with the heat of adsorption values >25 kJ/mol and the largest cavity diameters of ca. 6–7 Å. Finally, we introduced augmented reality (AR) visualizations as a means to bring adsorption phenomena alive in porous adsorbents and to dynamically explore gas adsorption sites in MOFs.

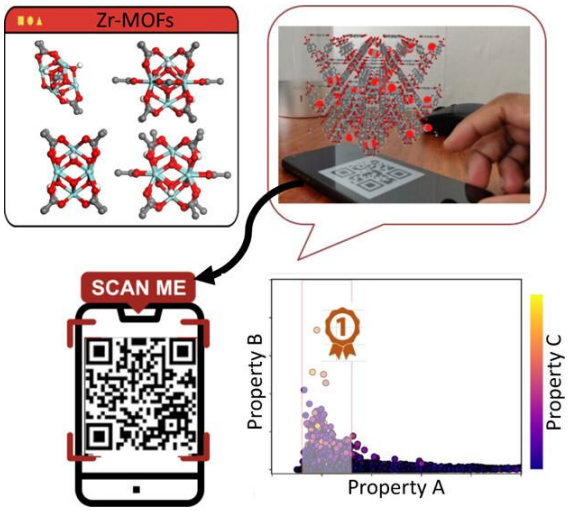

Chapter 3

3.1. Introduction

Metal–organic frameworks (MOFs) are now a well-established generation of porous materials, which are formed by extended coordination networks of metal clusters and organic building blocks. MOFs can be readily tailored to produce thousands of materials with a vast range of pore sizes, shapes, and chemistries with promise for numerous applications in specific gas storage and separation.[1–7] Indeed, we have already identified a staggering ca. 100,000 already-synthesized MOFs in the Cambridge Structural Database (CSD) as of January 2020 (2020.0 CSD release).[8–10] Of all the identified MOF materials in the CSD, ca. 10,000 are porous (i.e., materials with pore-limiting diameter (PLD) > 3.7 Å), which can be explored for adsorption applications. In our recent work, we developed an array of algorithms to classify different families of porous MOFs based on some of their most well-known metal secondary building units (SBUs).[9] Clearly, such databases and classifications create excellent opportunities for in silico screening practices for targeted exploration of MOFs for gas adsorption.[9] However, in this context, a crucial and often overlooked aspect of MOFs is their ability to withstand exposure to industrial processes for gas sorption. With this idea in mind, here, we focus on the computational characterization of one of the undoubtedly key families of stable MOFs: structures containing Zr-oxide SBUs. We expect that this study will guide experimental and theoretical researchers to carry out transformative research on this promising class of MOFs for novel adsorption technologies.

Zr-oxide MOFs have great potential for gas adsorption and separation applications owing to their porosity, regenerability, and good chemical and physical stability properties.[11–13] The high oxidation state of Zr generates strong Zr–O SBUs, and the high connectivity with the organic ligands boosts their mechanical stability.[14,15] Furthermore, most structures maintain their structural integrity at temperatures up to 450 °C and in aqueous or acidic conditions.[12,13,16–18]

Given the large number of existing MOFs, including those containing Zr-oxide nodes, quite a few high-throughput computational protocols have been developed to screen and identify top-performing materials before synthesis and experimental testing in the laboratory.[19–23] Predominantly, theoretical approaches combining density functional theory (DFT) and grand canonical Monte Carlo (GCMC) calculations have successfully predicted the gas adsorption properties of MOFs. The accuracy of such simulations relies on the force field parameters that describe adsorbate–MOF and adsorbate–adsorbate interactions. In addition to van der Waals interactions, for polar and quadrupolar adsorbates, it is essential to take into account the

electrostatic interactions between the adsorbate and the MOF atoms. Such interactions are normally described by assigning partial charges to framework atoms. Different methods have been developed to calculate MOF's atomic charges, for which significant variations in adsorption predictions could arise.[24–29] Popular methods include semi-empirical approaches, such as charge equilibration methods[30] and those based on bond connectivity[31] that require no electronic structure calculation, or charge assignment approaches based on quantum mechanical calculations, such as CHarges from ELectrostatic Potentials using a Grid-based method (ChelpG),[32] density derived electrostatic and chemical (DDEC),[33] and repeating electrostatic potential extracted atomic (REPEAT),[34] to generate electrostatic-potential-derived atomic charges. A number of studies have compared the sensitivity of gas adsorption predictions with respect to the method used to assign partial atomic charges. In an outstanding contribution, Nazarian et al.[35] compared atomic point charges derived from EQeq and the DDEC approaches for the adsorptive removal of tert-butyl mercaptan from natural gas and found a significant difference in predicted adsorption selectivity depending on the charge assignment method. In general, the DDEC approach reproduces the electrostatic interactions outside the van der Waals radius of atoms, and this is especially important for gas adsorption simulations. Similar to the conclusions of this work and others,[24] the general consensus is that DFT methods provide more accurate partial charge predictions and therefore are more reliable for gas adsorption simulations especially in the low-pressure regime-Henry's region in the isotherm, where adsorbate–MOF interactions dominantly determine the amount of the gas adsorbed and the shape of the isotherm.

Importantly, we note that none of the 2932 experimentally synthesized MOF structures in Nazarian et al.'s work are Zr-oxide MOFs, and given the importance of this class of materials, in the present work, we performed a systematic study to identify, characterize, and calculate the partial atomic charges for Zr-oxide MOFs present in the CSD MOF subset. Finally, we use this subset of structures in a high-throughput screening study to explore their capabilities for CO_2 capture in flue gas conditions.

3.2. Results and Discussion

3.2.1. Zr-Oxide MOFs: Identification and Geometric Characterization

We used ConQuest, the CCDC's primary software for searching structures, to develop seven search queries (Figure S1) to identify all MOF materials containing the Zr-oxide cluster from the CSD MOF subset. We successfully hit 102 structures among the existing ca. 100,000 MOFs (**Figure 3.1**).

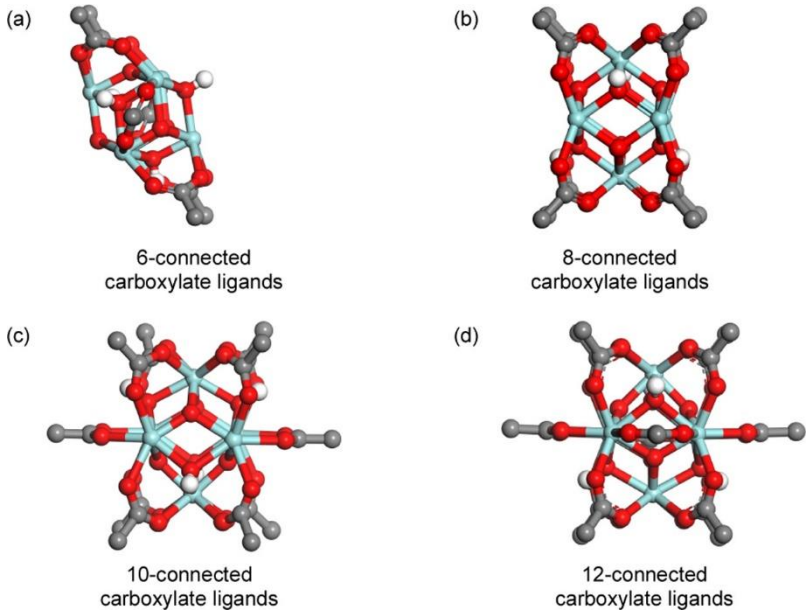

Figure 3.1. Three-dimensional (3D) representation of Zr-oxide secondary building units (SBUs) based on Zr6 clusters: (a) 6-connected carboxylates in PCN-224; (b) 8-connected carboxylates in PCN-222; (c) 10-connected carboxylates in DUT-67; (d) 12-connected carboxylates in UiO-66.

After generating the subset of Zr-MOFs and fixing the position of OH groups for each structure,[36–39] we calculated different geometric descriptors such as accessible surface area (ASA), largest cavity diameter (LCD), pore-limiting diameter (PLD), void fraction, and density using the Zeo++ software package.[40] **Figure 3.2** shows the distribution of the geometric properties. While a wide range of physical properties is achievable in Zr-oxide MOFs, most structures are concentrated in regions with micropores with LCDs < 20 Å and void fractions of 0.3–0.5, possibly due to the commercial availability of shorter linkers such as benzene–dicarboxylic acid and the popularity of this range of pore size for gas storage and separation applications. Of all, 85% of structures have gravimetric surface areas between 1500 and 4500 m^2/g, volumetric surface areas of 1500 and 2500 m^2/cm^3, and densities <1.5 g/cm^3. The geometric and physical properties of all the Zr-oxide MOFs are tabulated in the Excel file in the Supporting Information.

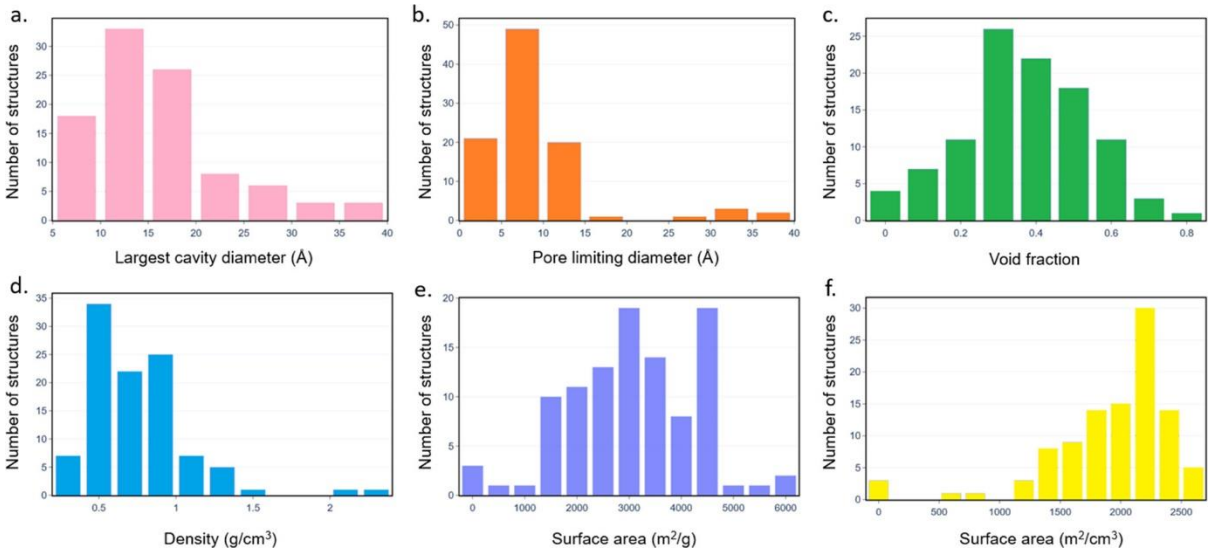

Figure 3.2. Histograms showing the calculated geometric properties of 102 Zr-oxide MOFs in the CSD MOF subset. (a) Largest cavity diameter, (b) pore-limiting diameter, (c) void fraction, (d) density, (e) gravimetric surface area, and (f) volumetric surface area.

The description of MOF topology is important as it provides the underlying connectivity of their building units.[41] Different topologies can result in variations in the pore size and shape, as well as mechanical stability.[15,42] We used CrystalNets[43] to assign topologies to each structure using a single-node simplification approach. Of the total 102 materials, we assigned Reticular Chemistry Structural Resource (RCSR)[41] topology identifiers to 100 structures, with one unknown topology and one topological type database (TTD) topology, which was obtained using ToposPro[44] from the Samara Topological Data Center. **Figure 3.3.a** shows the frequency of topologies for the structures in the subset with 17 unique three-character RCSR identifiers and one unique TTD identifier. A number of materials were assigned with two topologies; in cases where metal nodes are linked by porphyrins or derivatives thereof, the consequence of changing the ring size parameter in Topos' cluster simplification method results in an alternative allocation of the connectivity of nonmetal nodes. The central porphyrin ring can be simplified into either four 3-connected nodes about the edges of the porphyrin structure or a single 4-connected node, resulting in the possible allocation of both **xxw** and **ftw** topologies, respectively. The result is subjective, but these structure types have been previously reported as **ftw** maintaining a single node at the center of the porphyrin linker. Additionally, the set contains 10 structures that consist of layers of interpenetrating material represented by two-dimensional (2D) kgd and 3D fcu nets. The five most frequently reported 3D periodic nets in this set are **fcu** with 49 structures followed by five structures for each **bcu**, **csq**, **she**, and **ftw** topology. Finally, a single 2D sql net was reported for the GOXZAW structure, which consists of layers of nonconnected 2D metal–organic sheets. **Figure 3.3.b** shows the range of LCD

values for the five most common topologies and shows that certain topologies may impose limits for structural descriptors including the pore size. LCDs range from 6.4 Å (**fcu**) to 37.9 Å (**csq**), varying dramatically from micropores to mesopores. Zr-oxide MOFs with **fcu** and **bcu** topologies exhibit micropores with LCDs < 20 Å. The structures with **ftw**, **she**, and **csq** topologies lie within the mesoporous region with LCD > 20 Å, where materials with **csq** topology contain the largest cavity diameter among all Zr-oxide MOFs.

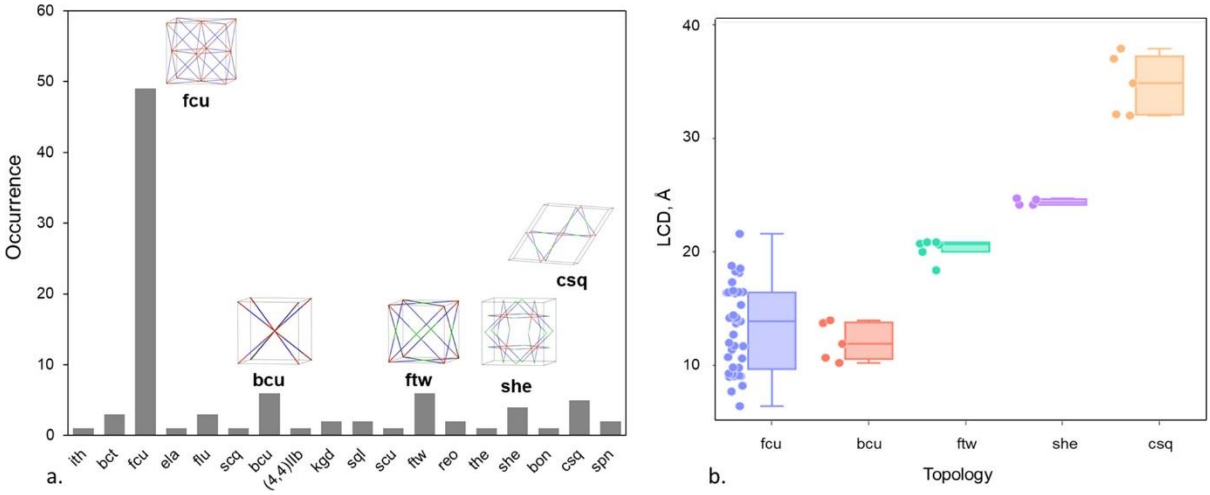

Figure 3.3. ***(a)*** *Histogram for the distribution of topologies for Zr-oxide MOFs; top-five topologies are shown in the inset: Zr-oxide node is shown in red, linkers in blue, and the green represents organic nodes.* ***(b)*** *Distribution of the largest cavity diameter (LCD) in selected topologies.*

3.2.2. N_2 Adsorption; Brunauer–Emmett–Teller (BET) Area Characterization

The surface area of MOFs is arguably their most attractive feature and is typically measured or calculated as part of MOF porosity characterization via N_2 adsorption. Here, we calculated N_2 adsorption isotherms at 77 K for all 102 Zr-oxide structures via GCMC simulations and estimated the BET area following the consistency criteria suggested by Rouquerol et al.[45] All N_2 adsorption isotherms and details of the BET area calculations are reported in the Supporting Information (Section S.3.3).

Among all structures, 85 MOFs complied with the four so-called "BET consistency criteria", while we had trouble finding the pressure range that would satisfy all four criteria for the remaining 17 structures. For these structures, after applying the first criterion, only one possible pressure range for BET calculations is eligible, meaning that the surface area calculated is insensitive to the remaining BET area criteria. **Figure 3.4.a** shows the parity plot comparing BET area values with the accessible surface area (ASA) for structures with different LCDs. The results show that, for the majority of structures, irrespective of their LCD range, ASA calculations report higher values compared to the BET area. We note that ASA is calculated using the Zeo++ software, where a spherical probe with a radius of 1.86 Å (the

kinetic radius of N_2) was used. We also note that almost all Zr-oxide MOFs have multiple pores in their structures with some as small as ca. 3.5–5 Å, i.e., their pore size is similar to the kinetic diameter of N_2 [see e.g., UiO-66, MOF-801, MOF-802, MOF-812, and PCN-702 pore size distribution (PSD) in the Supporting Information]. The presence of these small pores creates regions in the structure that may not be easily accessible to N_2 molecules in GCMC simulations and therefore underestimating the monolayer loading.

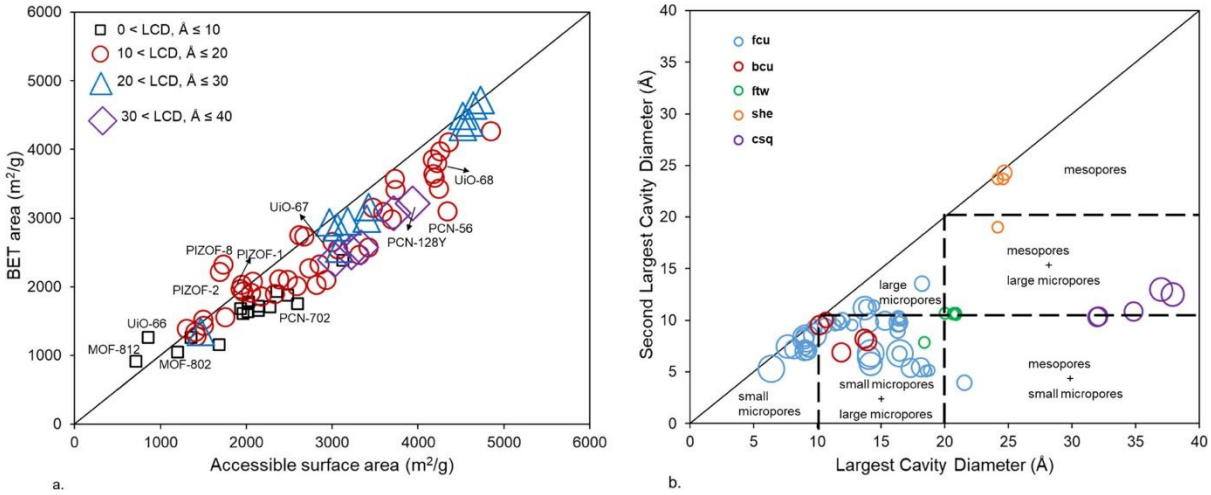

Figure 3.4. ***(a)*** *BET area vs accessible surface area calculated for 102 Zr-oxide MOFs with various ranges for the largest cavity diameter (LCD);* ***(b)*** *relationship between the largest cavity diameter and the second-largest cavity diameter for the top-five topologies in Zr-oxide MOFs. The color represents the topology; the size of the data points corresponds to the proportional absolute deviation between the BET area and ASA.*

According to the previous study performed by Gómez-Gualdrón et al.,[46] BET calculations for MOFs that fulfill all four consistency criteria can still inaccurately characterize the true monolayer loading, especially for structures combining mesopores (d ≥ 20 Å) and large micropores (d = 10–20 Å). Figure 4b presents the distribution of LCD and the second-largest cavity diameter for the top-five topologies and highlights the deviation between the BET area and ASA, represented proportionally by the size of the data points. For the **fcu** topology, large deviations were seen for structures with small micropores (pore diameter <10 Å) and those combining large micropores and small micropores. This was also observed for MOFs with the **bcu** topology (20% deviation) where there are no structures with LCD larger than 20 Å and those structures with small micropores as their LCD. Zr-oxide MOFs with **ftw** and **she** topologies show low deviation (<10%) since they mostly contain LCD > 20 Å and no micropores as their second LCD. A significant deviation (20–40%) was observed for structures with the **csq** topology. These structures combine mesopores (d ≥ 20 Å) with a higher proportion compared to the large micropores (d = 10–20 Å). Such deviations could arise from how the Voronoi nodes are sampled in Zeo++ and the accessibility of tight regions of the pore to the nitrogen's geometric probe model. We hope this analysis provides a benchmark for assessing

the quality of Zr-oxide MOFs, for example, what is the upper limit of the surface area that can be achieved if the structural integrity is maintained or if the MOF is completely activated in the solvent removal process? This will, in turn, give information about the expected experimental adsorption performance of a MOF.

3.2.3. Atomic Charge Assignment and CO_2 Adsorption Simulations

We also investigated the performance of Zr-oxide MOFs for CO_2 capture. Before running the calculations in a high-throughput manner, we first compared the calculated adsorption isotherms with experimental data available in the literature. Given that CO_2 has a high quadruple moment, its adsorption prediction highly relies on the electrostatic interactions with the framework. Therefore, it is important to take into account such interactions using electronic structure calculations such as density functional theory (DFT). DFT calculations can provide insight into the electrostatic potential energy surface, which can be tabulated as point charges on framework atoms. To study the performance of DFT calculations to predict partial atomic charges, we performed systematic periodic DFT calculations comparing 25 different combinations of basis sets and functionals. To do this, we first selected two prototypical Zr-oxide MOFs, namely, UiO-66 and UiO-67, where experimental CO_2 adsorption isotherms were available. We then investigated the sensitivity of assigned point charges and the relevant CO_2 adsorption isotherms for different DFT methods. **Figure 3.5.a,b** shows the calculated CO_2 adsorption isotherms obtained from various combinations of DFT functionals and basis sets and compares them with experiments for UiO-66 and UiO-67, respectively[47,48] (**Figures S.3.4 and S.3.5** present data for all combinations of DFT basis sets and functionals attempted). In general, the amount of CO_2 adsorbed at high pressure and the shape of the isotherms are rather similar when electrostatic interactions are taken into account through different DFT calculations. For UiO-66, at low-pressure regime (ca. 1 bar), where the framework–CO2 interactions are dominant, the amount of predicted CO_2 ranges between 1.7 and 3 mol/kg depending on the DFT method used. Such deviations are less prominent for UiO-67, a structure with larger pores, with CO_2 uptake predictions ranging between 0.8 and 1.3 mol/kg at 1 bar. For both UiO-66 and UiO-67, the combination of PBE0 functional with the def2-svp basis set provides an excellent match with the experimental data, and therefore, we selected this DFT method to calculate partial atomic charges for the rest of the Zr-oxide MOFs (37 structures). We introduce Average Absolute Deviation (AAD) as the criteria for the selection of best combinations for high throughput screening process. AAD was also defined in eq. 3.1

$$AAD(\%) = \frac{1}{N}\sum_{N=1}^{N}\frac{CO_2uptake^{sim} - CO_2uptake^{exp}}{CO_2uptake^{sim}} x\ 100\% \quad (3.1)$$

We determined the best DFT combinations according to the absolute average deviation (AAD) value between simulation and experimental data. The best combinations were chosen from its smallest value in its AAD where the AAD is defined in above equation. Those combinations give the smallest AAD of *c.a* 9% compared to other combination of basis sets and functionals that can give AAD value even larger than 10%, especially at lower pressure regimes. For the comparison we used experimental data measured by Cavka, et al.[47] The remaining calculations failed to converge to a suitable state or were too computationally expensive at this level of theory and thus were omitted.

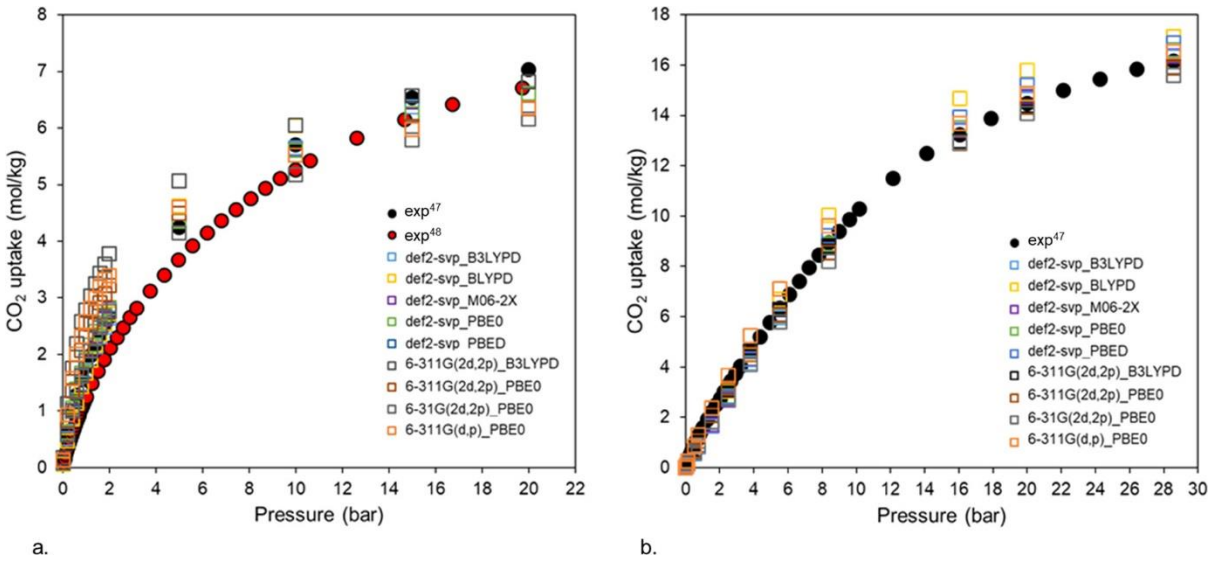

Figure 3.5. Simulated and experimental CO_2 adsorption isotherms for (a) UiO-66 and (b) UiO-67 at 298 K. The isotherms were calculated using different DFT calculations for partial atomic charge assignment.

After we calculated the partial atomic charges for the Zr-oxide MOFs, we performed high-throughput GCMC simulations to identify promising materials for CO_2 adsorption. We targeted CO_2 capture from flue gas in the post-combustion application at 298 K and 0.15 bar. Details of adsorption simulations are outlined in the Section 3.3. Similar to the adsorption of other gases, CO_2 capture in Zr-oxide MOFs likely depends on different structural descriptors, including LCD, surface area, void fraction, structure density, as well as the heat of adsorption (Qst). To maximize CO_2 capture performance, the combination of these descriptors must be optimized. **Figure 3.6** shows the relationship between the amount of CO_2 adsorbed at 0.15 bar and 298 K, the LCD, the number of node connections (size), and the CO_2 heat of adsorption (color). For the majority of MOFs with Qst < 22 kJ/mol, CO_2 adsorption capacity is very low and stays at <1 mol/kg. For the UiO family of MOFs, the amount of CO_2 adsorbed decreases as the length of a linker and therefore the pore size increases from one benzene ring in UiO-66

to two and three benzene rings in UiO-67 and UiO-68, respectively. In all three structures, the CO_2 uptake remains below 1 mol/kg. In general, the maximum CO_2 uptake is obtained for structures with Qst values >25 kJ/mol and LCD values of ca. 6–7 Å. The material with the highest predicted CO_2 adsorption capacity is MOF-812[49] with 2.5 mol/kg. This trend is also observed in some previous studies on computational screening of MOFs for CO_2 capture application.[50–53] The SBU in MOF-812 is connected to 12 tetrahedral linkers resulting in a 3D network of **ith** topology, which is different from the typical 12-connected Zr SBUs in the **fcu** series. To gain molecular-level insight into CO_2 adsorption in MOF-812 and UiO-66, we compared their simulation snapshots at 0.15 bar and 298 K and found that CO_2 molecules prefer to sit much closer to the Zr-nodes in MOF-812 (**Figure 3.7.a**). This finding is also confirmed by the analysis of the radial distribution function (RDF) of atom pairs between the framework Zr and the oxygen atom in CO_2 (**Figure 3.7.b**). In MOF-812, the first peak appears at 2.5 Å, while for UiO-66, another structure with 12-connected nodes, we observe a much larger distance between Zr and CO_2 molecules, with the first peak rising at 5 Å. Analysis of the pore size distribution (PSD) shows that MOF-812 contains smaller pores (4 and 5.5 Å) compared to those of UiO-66, whose small and large pores are 6.8 and 7.7 Å, respectively. The simulation snapshots show that in UiO-66, CO_2 molecules reside in the small tetrahedral pores, whereas in MOF-812, CO_2 molecules preferentially sit in the space between the Zr-oxide nodes in addition to the pockets in between the tetrahedral linkers: see the blue CO_2 molecules in **Figure 3.7.a**. The proximity of CO_2 molecules to the Zr-oxide nodes in MOF-812 is also explained by the dominant MOF–CO2 electrostatic interactions (Figure S8). Using our online Wiz visualization platform,[54] one can dynamically probe the effects of different textural properties on CO_2 adsorption capacity for all the Zr-oxide MOFs studied here.

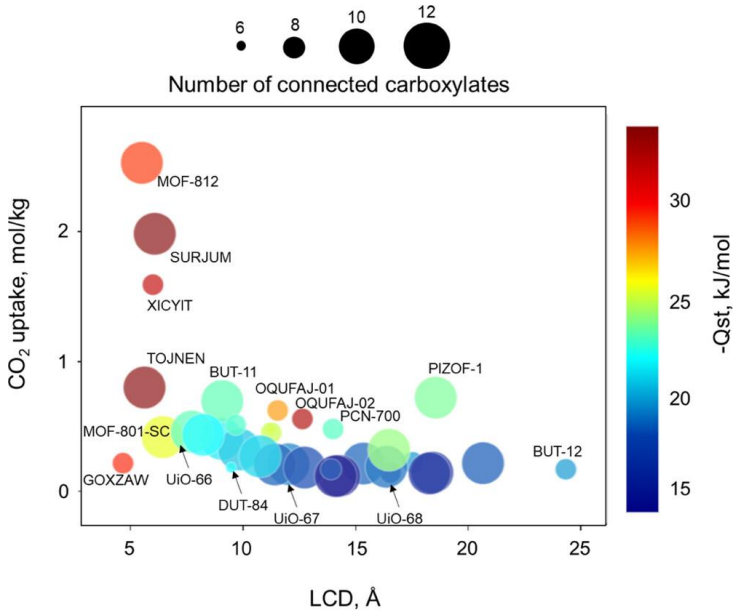

Figure 3.6. Structure–property relationships for CO_2 capture in Zr-oxide MOFs at 0.15 bar and 298 K.

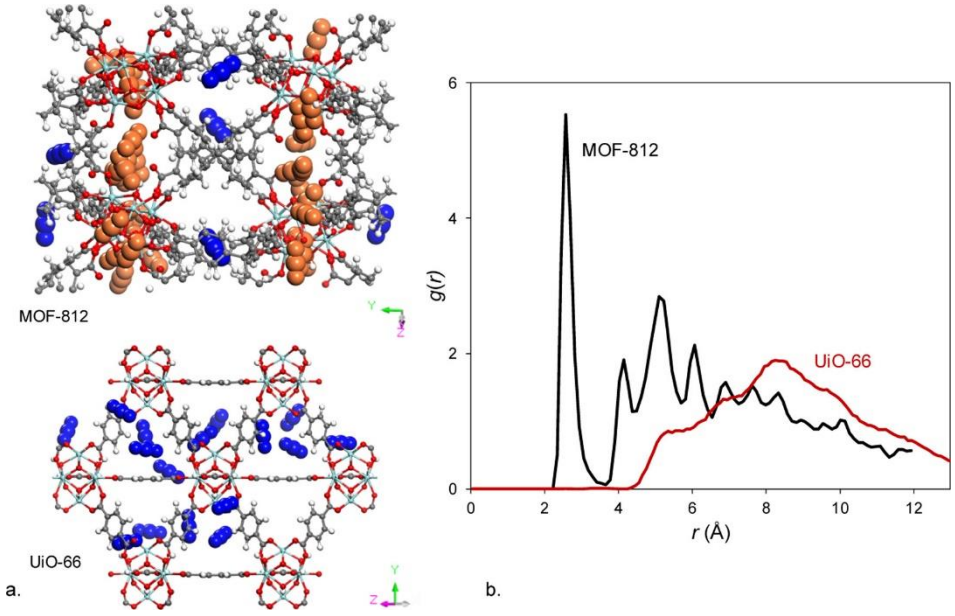

Figure 3.7. ***(a)*** *CO_2 adsorption snapshots in MOF-812 and UiO-66 simulated at 0.15 bar and 298 K. In UiO-66, CO_2 molecules are adsorbed in small tetrahedral pores. In MOF-812, CO_2 molecules sit preferentially in the space between the Zr-oxide nodes (orange vdW representation) in addition to the pockets created by the tetrahedral linkers (blue vdW representation).* ***(b)*** *Radial distribution functions between the Zr atom of the MOF and the O atom in CO_2 molecules in MOF-812 and UiO-66.*

To probe the sensitivity of CO_2 uptake predictions to the chemistry of Zr-oxide nodes with less than 12 connections, we took one of the 8-connected structures (BOSZEQ[55]) and removed the water and hydroxyl groups from the Zr-oxide node before running CO_2 adsorption simulations (**Figure S.3.7**). In other words, the newly constructed structure ($Zr_6O_4(OH)_4(RCO_2)_8$) differs in its SBU chemistry compared to the staggered mixed node proton topology[39] where water and hydroxyl groups are connected to Zr atoms ($Zr_6O_4(OH)_4(OH)_4(OH_2)_4(RCO_2)_8$). The CO_2 adsorption predictions for these two seemingly

similar structures are significantly different (**Figure S.3.6**). At 0.15 bar and 298 K, the staggered protonated coordination gives substantially lower CO_2 uptake (0.16 mol/kg) than the structure with no water or hydroxyl groups (5.3 mol/kg). Such a significant increase in the CO_2 uptake prediction is driven by the enhanced MOF–CO_2 electrostatic interactions (**Figure S.3.8**) and reveals the importance of the Zr-oxide node chemistry when dealing with MOFs with site defects (e.g., Zr-oxide SBUs with fewer than 12 connections). This suggests that care must be taken when conducting adsorption simulations for these systems.

3.2.4. Augmented Reality (AR) Visualization of Gas Adsorption Sites

Provision of detailed information about MOF's structural network, pores, surface chemistry, and preferential adsorption sites has been crucial in helping us to better understand the adsorption phenomena. Such information can be more useful and interactive if one can convey it in three-dimensional (3D) perspectives as more and more complex structures are designed and synthesized every day. A new emerging visualization technology that is widely used in other areas is augmented reality (AR). AR offers a seamless interface combining real and virtual worlds and has been employed as a teaching medium in the science field[56,57] and used in the visualization of 3D molecular structures.[58] In the present study, we use AR to not only visualize MOF structures but, more importantly, for the detection of favorable adsorption sites for gas molecules enabling experimental and computational MOF scientists to better understand the pore environment. To the best of our knowledge, this is the first AR visualization of gas adsorption in MOFs. Figure 8 demonstrates the application of AR for CO_2 adsorption in UiO-66. GCMC simulation snapshots obtained at different CO_2 loadings are used as input files for AR engine (Vuforia platform)[59,60] to analyze CO_2 adsorption sites at different loadings. At low pressures up to 1 bar (**Figure 3.8.b**), CO_2 molecules mainly occupy the tetrahedral cage and only start filling the octahedral cages when the pressure exceeds 10 bar. By creating different bar codes for each configuration, one can flick through different simulation snapshots and analyze the adsorption sites at different pressures. The AR visualization procedure, explained thoroughly in the methods section, can be applied to any MOF for detailed structural analysis and for the identification of adsorption sites in a more realistic way.

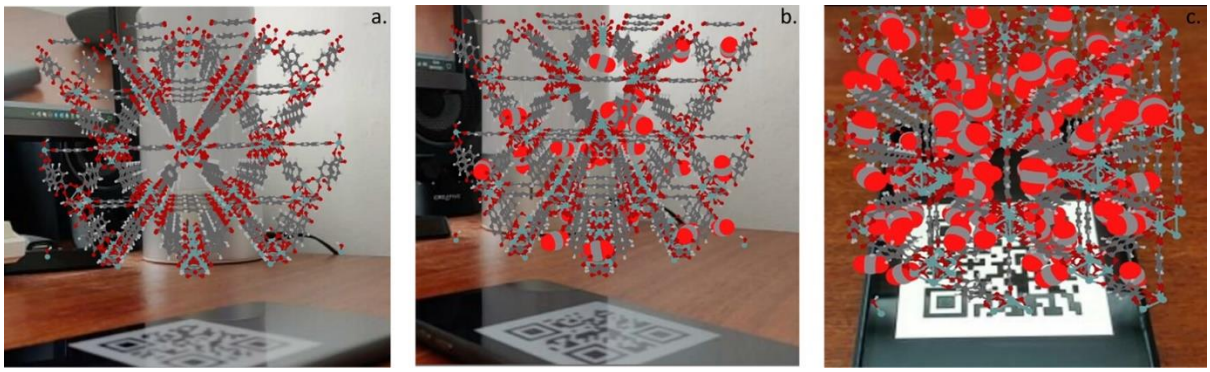

Figure 3.8. Augmented reality (AR) screenshots of (a) UiO-66 with CO_2 molecules preferential adsorption sites at (b) at low pressure (1 bar) and (c) high pressure (10 bar).

3.3. Methods

3.3.1. DFT Partial Atomic Charges Calculations

DFT simulations were performed with the fully periodic CRYSTAL17 software package.[61] Simulations were initialized from previously reported single-crystal X-ray structures, which were obtained from the CCDC. Initially, five representative Zr-MOFs (BOGNES, BOSZEQ, MAFWEY, MUBZOA, and UiO-66) were selected for a comprehensive investigation into the influence of choice of density functional and basis set on the calculated partial charges. The five basis set were 6-31G(d,p), 6-31G(2d,2p), 6-311G(d,p), 6-311G(2d,2p), and def2-SVP. The five different functionals tested were PBE, PBE0, BLYP, B3LYP, and M06-2X. The convergence on the energy was set to $\Delta E \leq 10^{-8}$ hartree, and a 2 × 2 × 2 Monkhorst–Pack grid was used to sample the reciprocal space lattice. Partial charges were calculated by subtracting the total atomic charge determined by the SCF electronic structure method from the atomic number using DDEC method. To evaluate if fully optimizing the geometries of the structures influenced the calculation of partial charges, we allowed the six structures to fully relax (atomic positions and lattice vectors) with an energy convergence criterion of $\Delta E \leq 10^{-8}$ hartree. Ultimately, it was found that the differences in partial charges between the optimized and unoptimized structures were minimal, and thus, for the final simulations, the structures were used without optimization of the geometry. All of the chosen basis sets and potentials were then verified by comparing CO_2 adsorption isotherms with published experimental data,[47,48] focused on the UiO MOFs family as a benchmark.

3.3.2. Gas Adsorption Calculations

The adsorption isotherms were calculated using grand canonical Monte Carlo (GCMC) simulations. We used 5000 cycles for equilibration and 5000 cycles to average properties for each pressure point, where a cycle is defined as the maximum of 20 or the number of molecules in the system. The interactions between CO_2–MOF and N_2–MOF were modeled by Lennard-Jones (LJ) plus Coulomb potentials. LJ parameters for all atoms in MOFs were taken from the Dreiding force field[62] except for the Zr atoms, for which we used the Universal force field (UFF) parameters. CO_2 and N_2 were modeled using the TraPPE force field.[63] The details of the force field parameters are presented in Table S1 in the Supporting Information. The Lorentz–Berthelot mixing rules were employed to calculate fluid/solid LJ parameters, and LJ potential was cut-off at 12.8 Å. The Ewald summation technique was used to calculate all electrostatic interactions.

All frameworks were considered rigid during the simulations. Insertion, deletion, and translation moves were attempted in the simulations with equal probabilities. All of the simulations were carried out using the RASPA molecular simulation software[64] and validated by comparison with published experimental data.

3.3.3. 5D Visualization Platform and Data Analytics

All data sets plotted here can be reproduced online using the Wiz visualization dashboard:[54] step-by-step instructions are provided at https://wiz.shef.ac.uk. Adsorption data as well as geometric properties are provided in the Supporting Information in a.csv file, which can be directly uploaded to Wiz for data visualization and analysis. Visitors to Wiz can generate structure–property relationships interactively by plotting variables into each of the five axes according to their interests. Users can also explore and search for MOFs by their name and geometric/adsorptive properties.

3.3.4. Augmented Reality Visualization

For AR visualization, two software packages (Jmol[65] and Unity[66]) and the Vuforia platform (Augmented Reality engine)[59] were used. Jmol was used to convert molecular structure files (.mol and.cif) into object files (.obj and.mtl), which can be imported to Unity. Unity was then used to set up the application and the Vuforia AR Engine and to assign the molecule objects to specific target images, which are set up through a Vuforia's online platform. A step-by-step guide for AR visualization of MOFs has been provided in https://doi.org/10.1021/acsami.2c13391 along with the supported screenshots and video link.

3.4. Conclusion

In this work, we generated a subset of 102 Zr-oxide MOFs deposited in the Cambridge Structural Database. For all structures, we characterized full geometric properties and successfully assigned their topologies. We also simulated full N_2 adsorption isotherms and calculated the surface area by rigorously applying the consistency criteria from the BET theory. When compared with geometrically calculated accessible surface area (ASA), in general, BET area calculations are lower than ASA for most Zr-oxide MOFs, especially those with micropores, as well as structures with the **csq** topology. The BET area characterization performed here offers experimentalists a benchmark for the quality assessment of the Zr-oxide MOFs: ensuring the BET consistency criteria are met, we suggest that the experimental BET area is compared with the simulated BET area and not ASA.

We also calculated and assigned partial atomic charges for 37 Zr-oxide MOFs using systematic periodic DFT calculations comparing 25 different combinations of basis sets and functionals. We validated the DFT calculations by comparing simulated CO_2 adsorption isotherms with published experimental data for UiO-66 and UiO-67. We found that the combination of PBE0 functional with the def2-svp basis set provides an excellent match with the experimental data. To determine the best combination, we introduce the deviation value in which the selected combination give the smallest deviation of *c.*a 9%. We then performed high-throughput GCMC simulations and derived structure–property relationships for CO_2 adsorption in Zr-oxide MOFs. We found that the maximum CO_2 uptake is obtained for structures with the heat of adsorption values >25 kJ/mol and the largest cavity diameters of ca. 6–7 Å. Importantly, we found that slight changes in the chemistry of Zr-oxide nodes result in significant changes in CO_2 adsorption predictions. For example, in BOSZEQ, when the proton topology of staggered water/hydroxyl is present on the Zr-node, substantially lower CO_2 uptake is predicted (0.16 mol/kg) compared to the case where water and hydroxyl groups are removed (5.3 mol/kg). Therefore, when comparing adsorption simulations and experiments, care must be taken when defining the chemistry of defective Zr-MOFs. All data presented in this paper can be uploaded and reproduced in Wiz, our web-based data analytics/visualization platform, allowing users to interactively explore structure–property correlations and search for structures with optimal structural and adsorptive properties.

In addition, we applied augmented reality (AR) to not only visualize and understand the complexity of Zr-oxide nodes but also introduced it as an educational tool to bring alive adsorption phenomena in porous materials, revealing both favorable adsorption sites and gas

capture interactions. It is our hope that such tools will ultimately augment material scientists' expertise to design functional materials using atomic- and molecular-level insights.

References

(1) Furukawa, H.; Cordova, K. E.; O'Keeffe, M.; Yaghi, O. M. The Chemistry and Applications of Metal-Organic Frameworks. *Science*. 2013. https://doi.org/10.1126/science.1230444.

(2) Freund, R.; Zaremba, O.; Arnauts, G.; Ameloot, R.; Skorupskii, G.; Dincă, M.; Bavykina, A.; Gascon, J.; Ejsmont, A.; Goscianska, J.; Kalmutzki, M.; Lächelt, U.; Ploetz, E.; Diercks, C. S.; Wuttke, S. The Current Status of MOF and COF Applications. *Angew. Chemie Int. Ed.* **2021**, *60* (45), 23975–24001. https://doi.org/https://doi.org/10.1002/anie.202106259.

(3) Bobbitt, N. S.; Mendonca, M. L.; Howarth, A. J.; Islamoglu, T.; Hupp, J. T.; Farha, O. K.; Snurr, R. Q. Metal–Organic Frameworks for the Removal of Toxic Industrial Chemicals and Chemical Warfare Agents. *Chem. Soc. Rev.* **2017**, *46* (11), 3357–3385. https://doi.org/10.1039/C7CS00108H.

(4) Lin, J.-B.; Nguyen, T. T. T.; Vaidhyanathan, R.; Burner, J.; Taylor, J. M.; Durekova, H.; Akhtar, F.; Mah, R. K.; Ghaffari-Nik, O.; Marx, S.; Fylstra, N.; Iremonger, S. S.; Dawson, K. W.; Sarkar, P.; Hovington, P.; Rajendran, A.; Woo, T. K.; Shimizu, G. K. H. A Scalable Metal-Organic Framework as a Durable Physisorbent for Carbon Dioxide Capture. *Science.* **2021**, *374* (6574), 1464–1469. https://doi.org/10.1126/science.abi7281.

(5) Trickett, C. A.; Helal, A.; Al-Maythalony, B. A.; Yamani, Z. H.; Cordova, K. E.; Yaghi, O. M. The Chemistry of Metal–Organic Frameworks for CO_2 Capture, Regeneration and Conversion. *Nat. Rev. Mater.* **2017**, *2* (8), 17045. https://doi.org/10.1038/natrevmats.2017.45.

(6) Adil, K.; Belmabkhout, Y.; Pillai, R. S.; Cadiau, A.; Bhatt, P. M.; Assen, A. H.; Maurin, G.; Eddaoudi, M. Gas/Vapour Separation Using Ultra-Microporous Metal–Organic Frameworks: Insights into the Structure/Separation Relationship. *Chem. Soc. Rev.* **2017**, *46* (11), 3402–3430. https://doi.org/10.1039/C7CS00153C.

(7) Allendorf, M. D.; Stavila, V.; Snider, J. L.; Witman, M.; Bowden, M. E.; Brooks, K.; Tran, B. L.; Autrey, T. Challenges to Developing Materials for the Transport and Storage of Hydrogen. *Nat. Chem.* **2022**, *14* (11), 1214–1223. https://doi.org/10.1038/s41557-022-01056-2.

(8) Moghadam, P. Z.; Li, A.; Wiggin, S. B.; Tao, A.; Maloney, A. G. P.; Wood, P. A.; Ward, S. C.; Fairen-Jimenez, D. Development of a Cambridge Structural Database Subset: A

Collection of Metal-Organic Frameworks for Past, Present, and Future. *Chem. Mater.* **2017**, *29* (7), 2618–2625. https://doi.org/10.1021/acs.chemmater.7b00441.

(9) Moghadam, P. Z.; Li, A.; Liu, X.-W.; Bueno-Perez, R.; Wang, S.-D.; Wiggin, S. B.; Wood, P. A.; Fairen-Jimenez, D. Targeted Classification of Metal–Organic Frameworks in the Cambridge Structural Database (CSD). *Chem. Sci.* **2020**, *11* (32), 8373–8387. https://doi.org/10.1039/D0SC01297A.

(10) Li, A.; Perez, R. B.; Wiggin, S.; Ward, S. C.; Wood, P. A.; Fairen-Jimenez, D. The Launch of a Freely Accessible MOF CIF Collection from the CSD. *Matter* **2021**, *4* (4), 1105–1106. https://doi.org/10.1016/j.matt.2021.03.006.

(11) Bai, Y.; Dou, Y.; Xie, L. H.; Rutledge, W.; Li, J. R.; Zhou, H. C. Zr-Based Metal-Organic Frameworks: Design, Synthesis, Structure, and Applications. *Chem. Soc. Rev.* **2016**, *45* (8), 2327–2367. https://doi.org/10.1039/c5cs00837a.

(12) Kirlikovali, K. O.; Chen, Z.; Islamoglu, T.; Hupp, J. T.; Farha, O. K. Zirconium-Based Metal–Organic Frameworks for the Catalytic Hydrolysis of Organophosphorus Nerve Agents. *ACS Appl. Mater. Interfaces* **2020**, *12* (13), 14702–14720. https://doi.org/10.1021/acsami.9b20154.

(13) Chen, Y.; Zhang, X.; Ma, K.; Chen, Z.; Wang, X.; Knapp, J.; Alayoglu, S.; Wang, F.; Xia, Q.; Li, Z.; Islamoglu, T.; Farha, O. K. Zirconium-Based Metal–Organic Framework with 9-Connected Nodes for Ammonia Capture. *ACS Appl. Nano Mater.* **2019**, *2* (10), 6098–6102. https://doi.org/10.1021/acsanm.9b01534.

(14) Nawrocki, J.; Rigney, M.; McCormick, A.; Carr, P. W. Chemistry of Zirconia and Its Use in Chromatography. *J. Chromatogr. A* **1993**, *657* (2), 229–282. https://doi.org/https://doi.org/10.1016/0021-9673(93)80284-F.

(15) Moghadam, P. Z.; Rogge, S. M. J.; Li, A.; Chow, C.-M.; Wieme, J.; Moharrami, N.; Aragones-Anglada, M.; Conduit, G.; Gomez-Gualdron, D. A.; Van Speybroeck, V.; Fairen-Jimenez, D. Structure-Mechanical Stability Relations of Metal-Organic Frameworks via Machine Learning. *Matter* **2019**, *1* (1), 219–234. https://doi.org/10.1016/j.matt.2019.03.002.

(16) Wiersum, A. D.; Soubeyrand-Lenoir, E.; Yang, Q.; Moulin, B.; Guillerm, V.; Yahia, M. Ben; Bourrelly, S.; Vimont, A.; Miller, S.; Vagner, C.; Daturi, M.; Clet, G.; Serre, C.; Maurin, G.; Llewellyn, P. L. An Evaluation of UiO-66 for Gas-Based Applications. *Chem. – An Asian J.* **2011**, *6* (12), 3270–3280. https://doi.org/10.1002/asia.201100201.

(17) Feng, D.; Gu, Z.-Y.; Li, J.-R.; Jiang, H.-L.; Wei, Z.; Zhou, H.-C. Zirconium-

Metalloporphyrin PCN-222: Mesoporous Metal–Organic Frameworks with Ultrahigh Stability as Biomimetic Catalysts. *Angew. Chemie Int. Ed.* **2012**, *51* (41), 10307–10310. https://doi.org/10.1002/anie.201204475.

(18) Cavka, J. H.; Jakobsen, S.; Olsbye, U.; Guillou, N.; Lamberti, C.; Bordiga, S.; Lillerud, K. P. A New Zirconium Inorganic Building Brick Forming Metal Organic Frameworks with Exceptional Stability. *J. Am. Chem. Soc.* **2008**, *130* (42), 13850–13851. https://doi.org/10.1021/ja8057953.

(19) Banerjee, D.; Simon, C. M.; Plonka, A. M.; Motkuri, R. K.; Liu, J.; Chen, X.; Smit, B.; Parise, J. B.; Haranczyk, M.; Thallapally, P. K. Metal–Organic Framework with Optimally Selective Xenon Adsorption and Separation. *Nat. Commun.* **2016**, *7* (1), ncomms11831. https://doi.org/10.1038/ncomms11831.

(20) Gómez-Gualdrón, D. A.; Colón, Y. J.; Zhang, X.; Wang, T. C.; Chen, Y.-S.; Hupp, J. T.; Yildirim, T.; Farha, O. K.; Zhang, J.; Snurr, R. Q. Evaluating Topologically Diverse Metal–Organic Frameworks for Cryo-Adsorbed Hydrogen Storage. *Energy Environ. Sci.* **2016**, *9* (10), 3279–3289. https://doi.org/10.1039/C6EE02104B.

(21) Ahmed, A.; Liu, Y.; Purewal, J.; Tran, L. D.; Wong-Foy, A. G.; Veenstra, M.; Matzger, A. J.; Siegel, D. J. Balancing Gravimetric and Volumetric Hydrogen Density in MOFs. *Energy Environ. Sci.* **2017**, *10* (11), 2459–2471. https://doi.org/10.1039/C7EE02477K.

(22) Moghadam, P. Z.; Islamoglu, T.; Goswami, S.; Exley, J.; Fantham, M.; Kaminski, C. F.; Snurr, R. Q.; Farha, O. K.; Fairen-Jimenez, D. Computer-Aided Discovery of a Metal–Organic Framework with Superior Oxygen Uptake. *Nat. Commun.* **2018**, *9* (1), 1378. https://doi.org/10.1038/s41467-018-03892-8.

(23) Boyd, P. G.; Chidambaram, A.; García-Díez, E.; Ireland, C. P.; Daff, T. D.; Bounds, R.; Gładysiak, A.; Schouwink, P.; Moosavi, S. M.; Maroto-Valer, M. M.; Reimer, J. A.; Navarro, J. A. R.; Woo, T. K.; Garcia, S.; Stylianou, K. C.; Smit, B. Data-Driven Design of Metal–Organic Frameworks for Wet Flue Gas CO_2 Capture. *Nature* **2019**, *576* (7786), 253–256. https://doi.org/10.1038/s41586-019-1798-7.

(24) Sladekova, K.; Campbell, C.; Grant, C.; Fletcher, A. J.; Gomes, J. R. B.; Jorge, M. The Effect of Atomic Point Charges on Adsorption Isotherms of CO_2 and Water in Metal Organic Frameworks. *Adsorption* **2020**, *26* (5), 663–685. https://doi.org/10.1007/s10450-019-00187-2.

(25) Dubbeldam, D.; Walton, K. S.; Vlugt, T. J. H.; Calero, S. Design, Parameterization, and Implementation of Atomic Force Fields for Adsorption in Nanoporous Materials. *Adv.*

Theory Simulations **2019**, *2* (11), 1900135. https://doi.org/10.1002/adts.201900135.

(26) Fernandez, M.; Trefiak, N. R.; Woo, T. K. Atomic Property Weighted Radial Distribution Functions Descriptors of Metal–Organic Frameworks for the Prediction of Gas Uptake Capacity. *J. Phys. Chem. C* **2013**, *117* (27), 14095–14105. https://doi.org/10.1021/jp404287t.

(27) Kancharlapalli, S.; Gopalan, A.; Haranczyk, M.; Snurr, R. Q. Fast and Accurate Machine Learning Strategy for Calculating Partial Atomic Charges in Metal–Organic Frameworks. *J. Chem. Theory Comput.* **2021**, acs.jctc.0c01229. https://doi.org/10.1021/acs.jctc.0c01229.

(28) Zanca, F.; Glasby, L. T.; Chong, S.; Chen, S.; Kim, J.; Fairen-Jimenez, D.; Monserrat, B.; Moghadam, P. Z. Computational Techniques for Characterisation of Electrically Conductive MOFs: Quantum Calculations and Machine Learning Approaches. *J. Mater. Chem. C* **2021**, *9* (39), 13584–13599. https://doi.org/10.1039/D1TC02543K.

(29) Rosen, A. S.; Iyer, S. M.; Ray, D.; Yao, Z.; Aspuru-Guzik, A.; Gagliardi, L.; Notestein, J. M.; Snurr, R. Q. Machine Learning the Quantum-Chemical Properties of Metal–Organic Frameworks for Accelerated Materials Discovery. *Matter* **2021**, *4* (5), 1578–1597. https://doi.org/10.1016/j.matt.2021.02.015.

(30) Wilmer, C. E.; Kim, K. C.; Snurr, R. Q. An Extended Charge Equilibration Method. *J. Phys. Chem. Lett.* **2012**, *3* (17), 2506–2511. https://doi.org/10.1021/jz3008485.

(31) Xu, Q.; Zhong, C. A General Approach for Estimating Framework Charges in Metal−Organic Frameworks. *J. Phys. Chem. C* **2010**, *114* (11), 5035–5042. https://doi.org/10.1021/jp910522h.

(32) Breneman, C. M.; Wiberg, K. B. Determining Atom-Centered Monopoles from Molecular Electrostatic Potentials. The Need for High Sampling Density in Formamide Conformational Analysis. *J. Comput. Chem.* **1990**, *11* (3), 361–373. https://doi.org/https://doi.org/10.1002/jcc.540110311.

(33) Manz, T. A.; Sholl, D. S. Chemically Meaningful Atomic Charges That Reproduce the Electrostatic Potential in Periodic and Nonperiodic Materials. *J. Chem. Theory Comput.* **2010**, *6* (8), 2455–2468. https://doi.org/10.1021/ct100125x.

(34) Campañá, C.; Mussard, B.; Woo, T. K. Electrostatic Potential Derived Atomic Charges for Periodic Systems Using a Modified Error Functional. *J. Chem. Theory Comput.* **2009**, *5* (10), 2866–2878. https://doi.org/10.1021/ct9003405.

(35) Nazarian, D.; Camp, J. S.; Sholl, D. S. A Comprehensive Set of High-Quality Point

Charges for Simulations of Metal–Organic Frameworks. *Chem. Mater.* **2016**, *28* (3), 785–793. https://doi.org/10.1021/acs.chemmater.5b03836.

(36) Rogge, S. M. J.; Wieme, J.; Vanduyfhuys, L.; Vandenbrande, S.; Maurin, G.; Verstraelen, T.; Waroquier, M.; Van Speybroeck, V. Thermodynamic Insight in the High-Pressure Behavior of UiO-66: Effect of Linker Defects and Linker Expansion. *Chem. Mater.* **2016**, *28* (16), 5721–5732. https://doi.org/10.1021/acs.chemmater.6b01956.

(37) Feng, D.; Chung, W.-C.; Wei, Z.; Gu, Z.-Y.; Jiang, H.-L.; Chen, Y.-P.; Darensbourg, D. J.; Zhou, H.-C. Construction of Ultrastable Porphyrin Zr Metal–Organic Frameworks through Linker Elimination. *J. Am. Chem. Soc.* **2013**, *135* (45), 17105–17110. https://doi.org/10.1021/ja408084j.

(38) Bon, V.; Senkovska, I.; Baburin, I. A.; Kaskel, S. Zr- and Hf-Based Metal–Organic Frameworks: Tracking Down the Polymorphism. *Cryst. Growth Des.* **2013**, *13* (3), 1231–1237. https://doi.org/10.1021/cg301691d.

(39) Planas, N.; Mondloch, J. E.; Tussupbayev, S.; Borycz, J.; Gagliardi, L.; Hupp, J. T.; Farha, O. K.; Cramer, C. J. Defining the Proton Topology of the Zr_6 -Based Metal–Organic Framework NU-1000. *J. Phys. Chem. Lett.* **2014**, *5* (21), 3716–3723. https://doi.org/10.1021/jz501899j.

(40) Willems, T. F.; Rycroft, C. H.; Kazi, M.; Meza, J. C.; Haranczyk, M. Algorithms and Tools for High-Throughput Geometry-Based Analysis of Crystalline Porous Materials. *Microporous Mesoporous Mater.* **2012**, *149* (1), 134–141. https://doi.org/https://doi.org/10.1016/j.micromeso.2011.08.020.

(41) O'Keeffe, M.; Peskov, M. A.; Ramsden, S. J.; Yaghi, O. M. The Reticular Chemistry Structure Resource (RCSR) Database of, and Symbols for, Crystal Nets. *Acc. Chem. Res.* **2008**, *41* (12), 1782–1789. https://doi.org/10.1021/ar800124u.

(42) Shevchenko, A. P.; Alexandrov, E. V; Golov, A. A.; Blatova, O. A.; Duyunova, A. S.; Blatov, V. A. Topology versus Porosity: What Can Reticular Chemistry Tell Us about Free Space in Metal–Organic Frameworks? *Chem. Commun.* **2020**, *56* (67), 9616–9619. https://doi.org/10.1039/D0CC04004E.

(43) Zoubritzky, L.; Coudert, F.-X. CrystalNets.Jl: Identification of Crystal Topologies. *SciPost Chem.* **2022**, *1* (2), 005. https://doi.org/10.21468/SciPostChem.1.2.005.

(44) Blatov, V. A.; Shevchenko, A. P.; Proserpio, D. M. Applied Topological Analysis of Crystal Structures with the Program Package ToposPro. *Cryst. Growth Des.* **2014**, *14*

(7), 3576–3586. https://doi.org/10.1021/cg500498k.

(45) Rouquerol, J.; Llewellyn, P.; Rouquerol, F. Is the Bet Equation Applicable to Microporous Adsorbents? In *Characterization of Porous Solids VII*; Llewellyn, P. L., Rodriquez-Reinoso, F., Rouqerol, J., Seaton, N. B. T.-S. in S. S. and C., Eds.; Elsevier, 2007; Vol. 160, pp 49–56. https://doi.org/10.1016/S0167-2991(07)80008-5.

(46) Gómez-Gualdrón, D. A.; Moghadam, P. Z.; Hupp, J. T.; Farha, O. K.; Snurr, R. Q. Application of Consistency Criteria To Calculate BET Areas of Micro- And Mesoporous Metal–Organic Frameworks. *J. Am. Chem. Soc.* **2016**, *138* (1), 215–224. https://doi.org/10.1021/jacs.5b10266.

(47) Cavka, J. H.; Grande, C. A.; Mondino, G.; Blom, R. High Pressure Adsorption of CO_2 and CH4 on Zr-MOFs. *Ind. Eng. Chem. Res.* **2014**, *53* (40), 15500–15507. https://doi.org/10.1021/ie500421h.

(48) Cmarik, G. E.; Kim, M.; Cohen, S. M.; Walton, K. S. Tuning the Adsorption Properties of UiO-66 via Ligand Functionalization. *Langmuir* **2012**, *28* (44), 15606–15613. https://doi.org/10.1021/la3035352.

(49) Furukawa, H.; Gándara, F.; Zhang, Y.-B.; Jiang, J.; Queen, W. L.; Hudson, M. R.; Yaghi, O. M. Water Adsorption in Porous Metal–Organic Frameworks and Related Materials. *J. Am. Chem. Soc.* **2014**, *136* (11), 4369–4381. https://doi.org/10.1021/ja500330a.

(50) Li, S.; Chung, Y. G.; Snurr, R. Q. High-Throughput Screening of Metal–Organic Frameworks for CO_2 Capture in the Presence of Water. *Langmuir* **2016**, *32* (40), 10368–10376. https://doi.org/10.1021/acs.langmuir.6b02803.

(51) Li, S.; Chung, Y. G.; Simon, C. M.; Snurr, R. Q. High-Throughput Computational Screening of Multivariate Metal–Organic Frameworks (MTV-MOFs) for CO_2 Capture. *J. Phys. Chem. Lett.* **2017**, *8* (24), 6135–6141. https://doi.org/10.1021/acs.jpclett.7b02700.

(52) Altintas, C.; Keskin, S. Role of Partial Charge Assignment Methods in High-Throughput Screening of MOF Adsorbents and Membranes for CO_2/CH_4 Separation. *Mol. Syst. Des. Eng.* **2020**, *5* (2), 532–543. https://doi.org/10.1039/C9ME00163H.

(53) Rogacka, J.; Seremak, A.; Luna-Triguero, A.; Formalik, F.; Matito-Martos, I.; Firlej, L.; Calero, S.; Kuchta, B. High-Throughput Screening of Metal – Organic Frameworks for CO_2 and CH_4 Separation in the Presence of Water. *Chem. Eng. J.* **2021**, *403*, 126392. https://doi.org/https://doi.org/10.1016/j.cej.2020.126392.

(54) Balzer, C.; Oktavian, R.; Zandi, M.; Fairen-Jimenez, D.; Moghadam, P. Z. Wiz: A Web-Based Tool for Interactive Visualization of Big Data. *Patterns* **2020**, 100107. https://doi.org/https://doi.org/10.1016/j.patter.2020.100107.

(55) Carboni, M.; Lin, Z.; Abney, C. W.; Zhang, T.; Lin, W. A Metal–Organic Framework Containing Unusual Eight-Connected Zr–Oxo Secondary Building Units and Orthogonal Carboxylic Acids for Ultra-Sensitive Metal Detection. *Chem. – A Eur. J.* **2014**, *20* (46), 14965–14970. https://doi.org/https://doi.org/10.1002/chem.201405194.

(56) Aw, J. K.; Boellaard, K. C.; Tan, T. K.; Yap, J.; Loh, Y. P.; Colasson, B.; Blanc, É.; Lam, Y.; Fung, F. M. Interacting with Three-Dimensional Molecular Structures Using an Augmented Reality Mobile App. *J. Chem. Educ.* **2020**, *97* (10), 3877–3881. https://doi.org/10.1021/acs.jchemed.0c00387.

(57) Ovens, M.; Ellyard, M.; Hawkins, J.; Spagnoli, D. Developing an Augmented Reality Application in an Undergraduate DNA Precipitation Experiment to Link Macroscopic and Submicroscopic Levels of Chemistry. *J. Chem. Educ.* **2020**, *97* (10), 3882–3886. https://doi.org/10.1021/acs.jchemed.0c00481.

(58) Eriksen, K.; Nielsen, B. E.; Pittelkow, M. Visualizing 3D Molecular Structures Using an Augmented Reality App. *J. Chem. Educ.* **2020**, *97* (5), 1487–1490. https://doi.org/10.1021/acs.jchemed.9b01033.

(59) Vuforia. https://www.vuforia.com/. Accessed 25 Jul 2021. Vuforia.

(60) Sung, R.-J.; Wilson, A. T.; Lo, S. M.; Crowl, L. M.; Nardi, J.; St. Clair, K.; Liu, J. M. BiochemAR: An Augmented Reality Educational Tool for Teaching Macromolecular Structure and Function. *J. Chem. Educ.* **2020**, *97* (1), 147–153. https://doi.org/10.1021/acs.jchemed.8b00691.

(61) Dovesi, R.; Erba, A.; Orlando, R.; Zicovich-Wilson, C. M.; Civalleri, B.; Maschio, L.; Rérat, M.; Casassa, S.; Baima, J.; Salustro, S.; Kirtman, B. Quantum-mechanical Condensed Matter Simulations with CRYSTAL. *WIREs Comput. Mol. Sci.* **2018**, *8* (4), e1360. https://doi.org/10.1002/wcms.1360.

(62) Mayo, S. L.; Olafson, B. D.; Goddard, W. A. DREIDING: A Generic Force Field for Molecular Simulations. *J. Phys. Chem.* **1990**, *94* (26), 8897–8909. https://doi.org/10.1021/j100389a010.

(63) Potoff, J. J.; Siepmann, J. I. Vapor–Liquid Equilibria of Mixtures Containing Alkanes, Carbon Dioxide, and Nitrogen. *AIChE J.* **2001**, *47* (7), 1676–1682. https://doi.org/10.1002/aic.690470719.

(64) Dubbeldam, D.; Calero, S.; Ellis, D. E.; Snurr, R. Q. RASPA: Molecular Simulation Software for Adsorption and Diffusion in Flexible Nanoporous Materials. *Mol. Simul.* **2016**, *42* (2), 81–101. https://doi.org/10.1080/08927022.2015.1010082.

(65) Jmol. Jmol: an open-source Java viewer for chemical structures in 3D. http://jmol.sourceforge.net/. Accessed 25 Jul 2021.

(66) Unity. Unity 3d. Https://Unity.Com/. Accessed 25 Jul 2021.

Supplementary Information Document

S.3.1. Search criteria in CCDC's structure search software, ConQuest

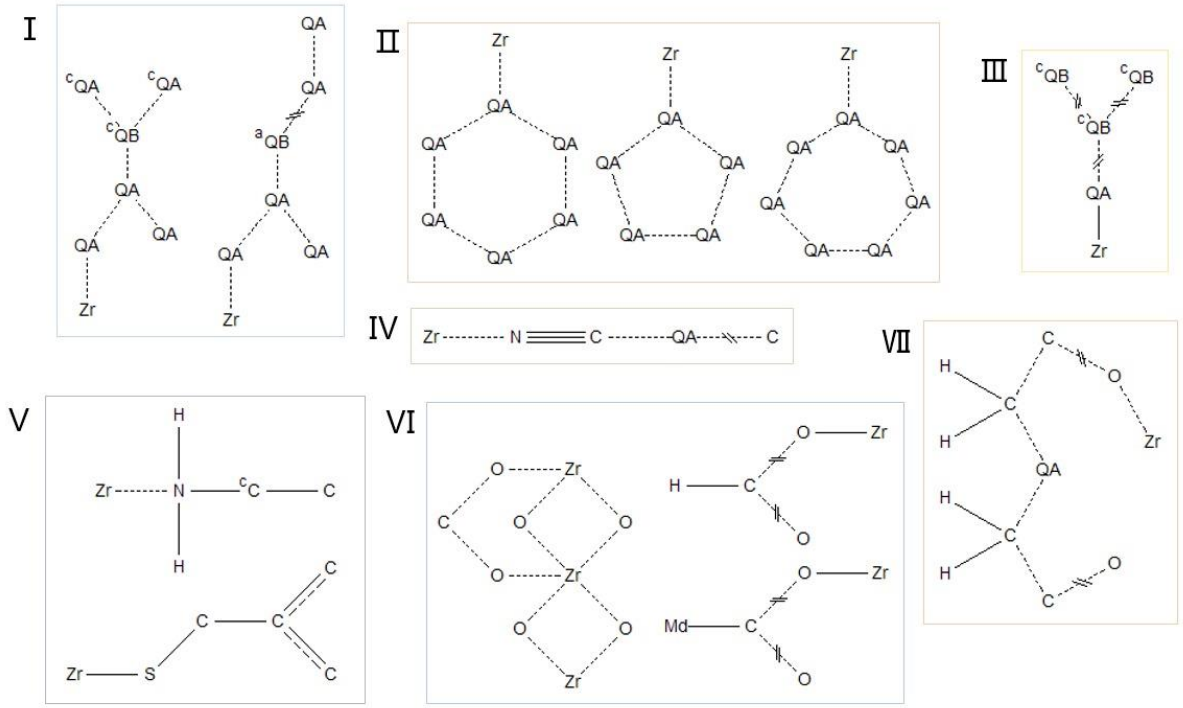

Figure S.3.1. Seven criteria developed for searching for Zr-oxide MOFs in the CSD MOF subset. QA = O, N, P, C, B, S. QB = N, P, B, S, C and superscripts "c" and "a" impose the corresponding atoms to be "cyclic" or "acyclic", respectively. Me denotes methyl groups (redrawn from the work of Moghadam et al.[1])

S.3.2. Constructing hydroxylated Zr-oxide clusters

Figure S2 shows UiO-66, a well-known Zr-oxide MOF that have been reported in two forms: hydroxylated ($Zr_6O_4(OH)_4$) and dehydroxylated (Zr_6O_8).[2] For consistency across all Zr-MOFs, before running the periodic DFT calculations, we manually added the hydroxyl groups for every structure extracted from the CSD MOF subset.

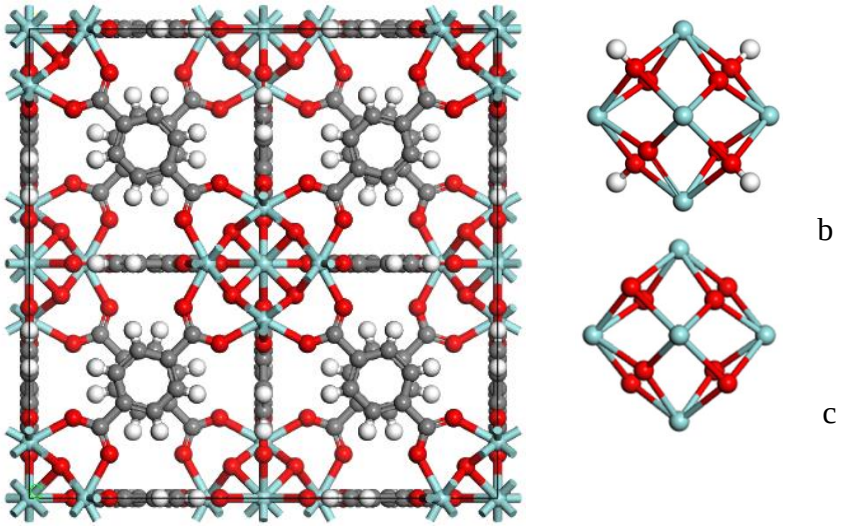

Figure S.3.2. a. The UiO-66 structure. Grey: C, white: H, red: O, cyan: Zr. b. hydroxylated and c. dehydroxylated Zr-oxide node.

S.3.3. N_2 adsorption isotherms and BET area calculations

Nitrogen adsorption isotherms (77 K) in all studied Zr-oxide MOFs were calculated via grand canonical Monte Carlo (GCMC) simulations using RASPA simulation software.[3] 10^4 Monte Carlo cycles were performed, the first 50% of cycles were applied for equilibration, and the remaining cycles were applied to calculate the ensemble averages. Insertion, deletion, rotation, and translation moves were set at equal probability. The framework atoms were kept fixed at the crystallographic positions for all Zr-oxide MOFs. Adsorbate-adsorbate and adsorbate-adsorbent interactions were modelled using a Lennard-Jones (LJ) plus Coulomb potential. The force field parameters for nitrogen and carbon dioxide were taken from the TraPPE force field. All force field parameters are tabulated in Tables S1-S3.

Table S.3.1. LJ parameters for the Zr-oxide MOFs.

Atom type	σ (Å)	ε/k_B (K)	Force field
C	3.473	47.856	Dreiding[4]
O	3.033	48.158	Dreiding[4]
H	2.846	7.649	Dreiding[4]
N	3.263	38.949	Dreiding[4]
Zr	2.783	34.722	UFF[5]

Table S.3.2. LJ parameters and partial charges for N_2.

Atom type	σ (Å)	ε/k_B (K)	Atomic charge	Force field
N_N_2	3.31	36.0	-0.482	TraPPE[6]
N_center of mass	0	0	0.964	TraPPE[6]
N_N_2	3.31	36.0	-0.482	TraPPE[6]

Table S.3.3. LJ parameters and charges for CO_2.

Atom type	σ (Å)	ε/k_B (K)	Atomic charge	Force field
C_CO_2	2.80	27.0	0.70	TraPPE[6]
O_CO_2	3.05	79.0	-0.35	TraPPE[6]

The procedure for BET area calculations is explained in detail as follows:

1) According to the BET theory,[7] monolayers usually form at pressures of $0.05 < P/P_0 < 0.3$. We chose this range as the first guess.
2) Plot the left side of eq. (1) versus selected range of relative pressure, perform linear regression to obtain values for *C* and *Nm*.

$$\frac{P/P_0}{N(1-P/P_0)} = \frac{1}{N_m C} + \frac{C-1}{N_m C}\left(\frac{P}{P_0}\right) \qquad (1)$$

3) Check compliance with consistency criteria 1 and 2.
4) Check whether the selected range from step 1 satisfy criteria 3. If not, pick another range of relative pressure and start from step 2 again.
5) Calculate the value of $(1/\sqrt{C}+1)$. Check whether the selected range from step 1 satisfies criteria 4.[8] If not, pick another range of relative pressure and start from step 2.
6) Calculate the BET area using eq. 2.
   $S = N_m . A_{N_2} . N_{AV} . \hat{V}_{N_2}$ (2)
   where: S = surface area, N_m = nitrogen monolayer uptake in m^3(STP)/g, A_{N2} = cross section of nitrogen molecule (1.62 x 10^{-19} m^2/molecule), N_{AV} = Avogadro number (6.022 x 10^{23}), $\hat{V}_{N_2}$ = nitrogen molar volume at STP (44.64 mol/m^3)

Figure S3 shows an example of N_2 adsorption isotherm in MOF-812 followed by BET area calculations. We note that we have provided N_2 adsorption isotherms and BET area calculations for all 102 Zr-oxide MOFs in the supporting information.

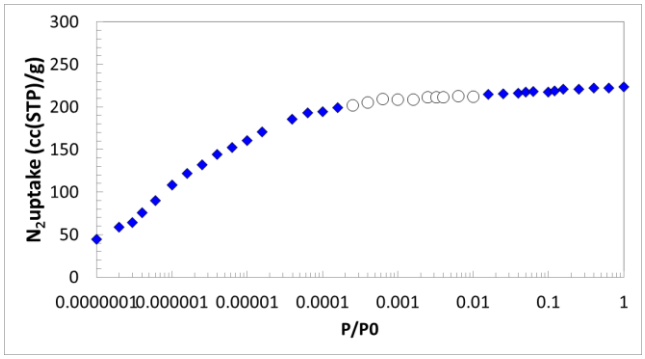

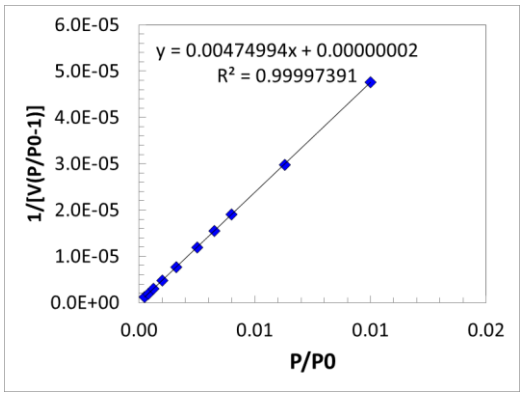

	range 1								
slope	0.00474994								
intercept	0.00000002								
C= 1 + slope/intercept	237498	0.002047763							
A= 1/(slope + intercept)	210.5280887								
uptake monolayer cm3(STP)/g	210.53								
cross section (m2/molecule)	1.62E-19								
molar volume (STP) (mol/m3)	44.64117195								
uptake monolayer m3(STP)/g	0.000210528								
avogadro (Nav)	6.02E+23								
BET surface area (m2/g)	917								
P/Po range	BET SA	A	R	N2@ upper P/Po	N2@lower P/Po	1/(√C + 1)	C	P(A) read	%e P(A)
	m2/g	cc(STP)/g		cc(STP)/g	cc(STP)/g				
0.0003-0.0100	917	210.53	0.999974	212.02	201.79	0.00205	237498.0000	0.0022926	-10.68

Figure S.3.3. Example BET area calculation for MOF-812 (CCDC refcode: BOHWOM). Left panel shows the calculated nitrogen adsorption isotherm: white symbols indicate the pressure range used for BET area calculation. Right panel shows the BET plot used for the first consistency criteria. Bottom panel presents the calculations used to test compliance with all four consistency criteria suggested by Rouquerol et al.[9]

The four consistency criteria proposed by Rouquerol *et al.*[9] are described in details here:

1) Only a range where $N(1 - P/P_o)$ increases monotonically with P/P_o should be selected.
2) The value of C resulting from the linear regression should be positive.
3) The monolayer loading N_m should correspond to a relative pressure P/P_o falling within the selected linear region.

4) The relative pressure corresponding to the monolayer loading calculated from BET theory ($1/\sqrt{C} + 1$) should be equal to the pressure determined in criterion 3. (For this criterion, Rouquerol *et al.*[9] suggested a tolerance of 20%.)

S.3.4. CO_2 adsorption isotherms in UiO-66 and UiO-67

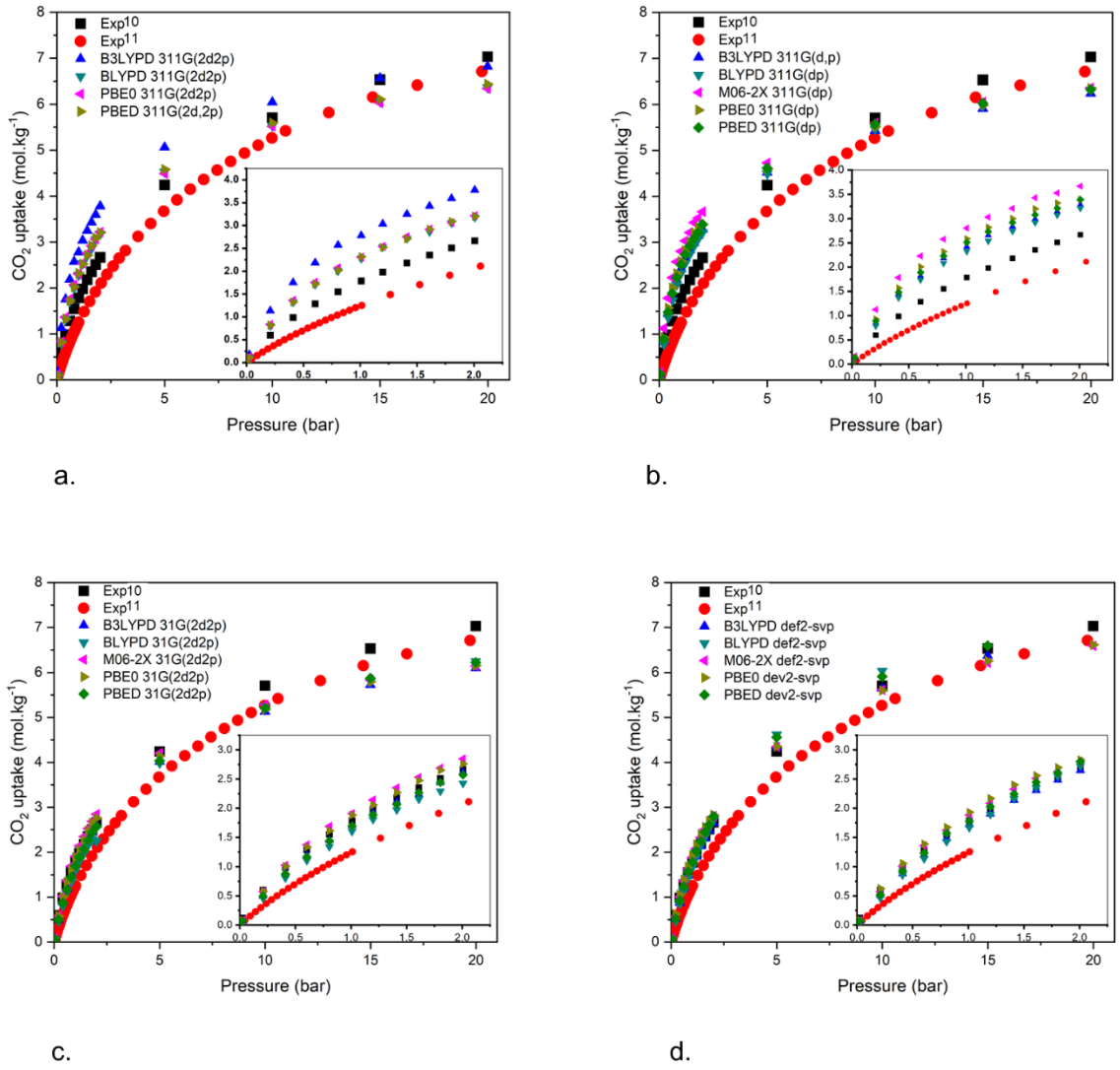

Figure S.3.4. CO_2 adsorption isotherms in UiO-66 at 298 K. Each simulated isotherm is obtained from a different combination of basis set and functional: a. 6-311G(2d,2p); b. 6-311G(d,p); c. 6-31G(2d,2p); d. dev2-svp. Experimental isotherms are shown for comparison.[10,11]

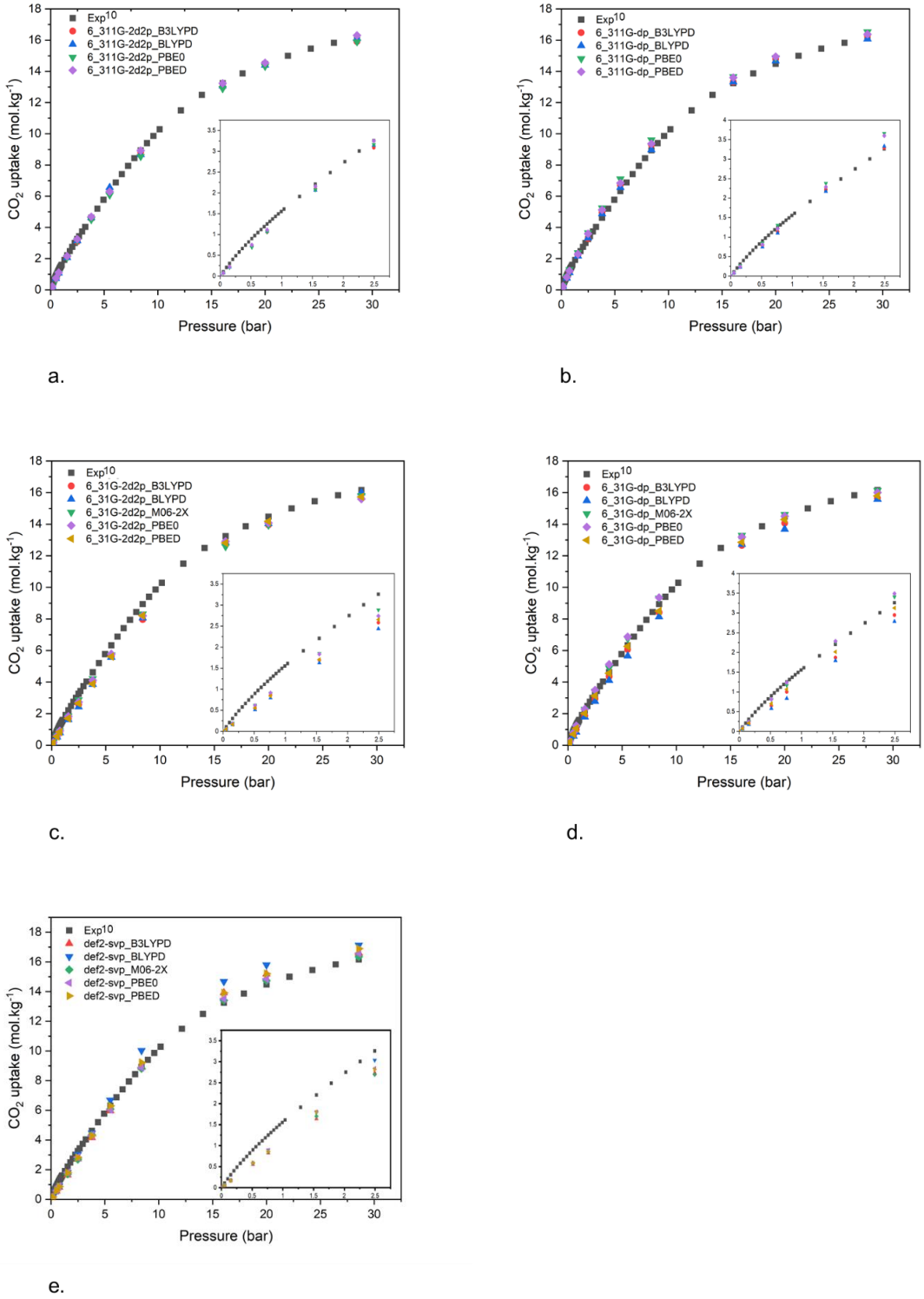

Figure S.3.5. ***CO_2*** *adsorption isotherms in UiO-67 at 298 K. Each simulated isotherm is obtained from a different combination of basis set and functional:* ***a.*** *6-311G(2d,2p);* ***b.*** *6-311G(d,p);* ***c.*** *6-31G(2d,2p);* ***d.*** *6-31G(d,p);* ***e.*** *dev2-svp. Experimental isotherms are shown for comparison.*[10]

S.3.5. CO_2 adsorption isotherms for BOSZEQ structures.

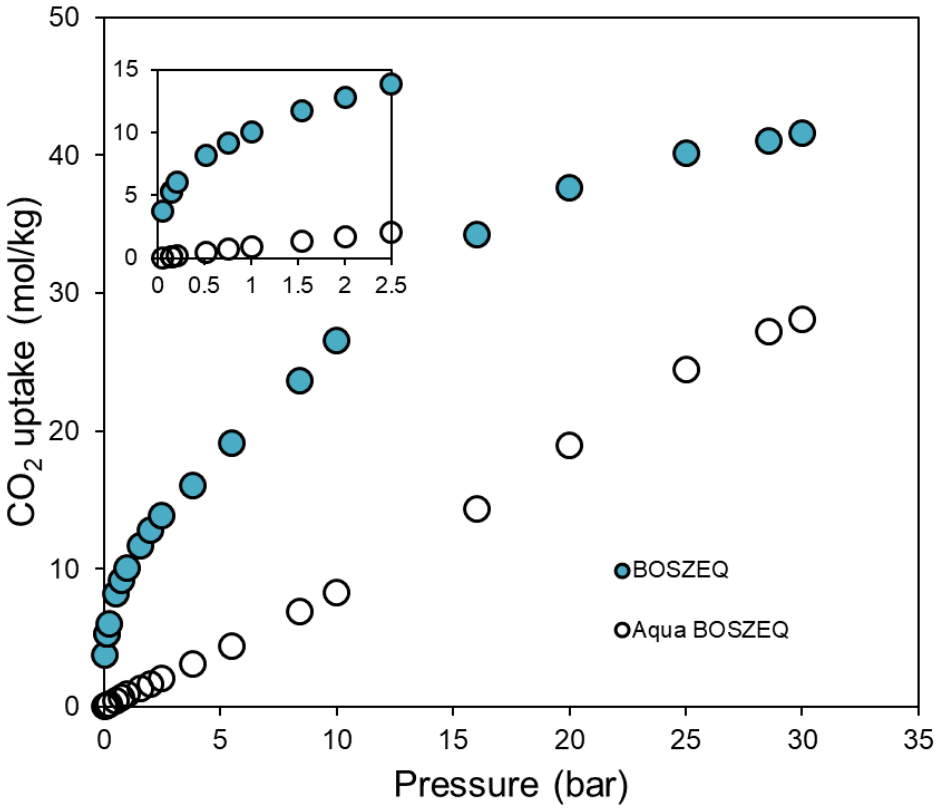

Figure S.3.6. CO_2 adsorption predictions in BOSZEQ (no water) and aqua BOSZEQ at 298 K, inset shows CO_2 adsorption at low pressure regime. The aqua BOXZEQ structure contains the staggered mixed node proton topology.

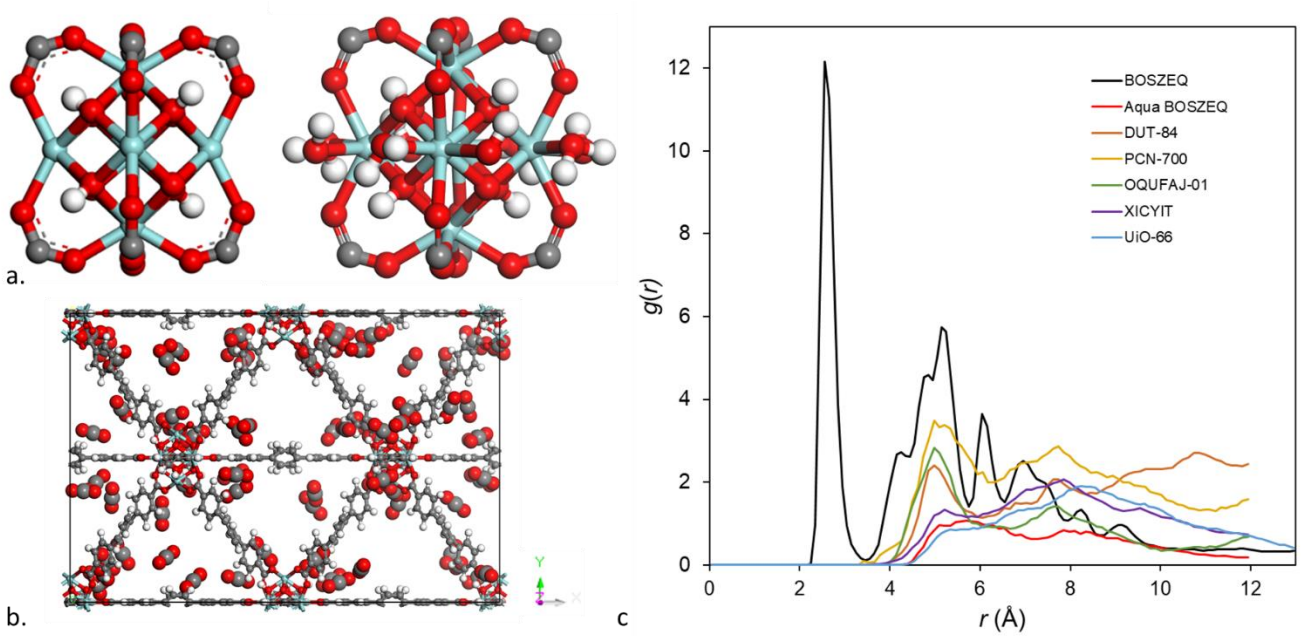

Figure S.3.7. ***a.*** *Metal cluster in BOSZEQ and BOXZEQ structure with the staggered mixed node proton topology i.e. aqua BOSZEQ;* ***b.*** *CO_2 adsorption snapshot in BOSZEQ simulated at 0.15 bar and 298 K;* ***c.*** *Radial distribution functions between Zr of the metal node and O of CO_2 molecules for selected MOFs. For aqua BOSZEQ, the presence of water molecules prevents CO_2 molecules sitting close to the pockets in between ligands and therefore the first RDF peak appears at ca. 5 Å. The proximity of CO_2 molecules to the Zr-oxide nodes in BOSZEQ is explained by the dominant MOF-CO_2 electrostatic interactions.*

S.3.6. MOF-CO_2 electrostatic interactions.

DFT simulations were performed with the fully periodic CRYSTAL17 software package.[12] Framework Partial charges were calculated by subtracting the total atomic charge determined by the SCF electronic structure method from the atomic number. For BOSZEQ, EMIYUW, OFAWID, OQUFAJ01-03, QOKBOJ, RUBLAD, UNEJEE, XICYIT and DITJOH structures, we used PBE0 functional and DDEC[13] charge partitioning approach.

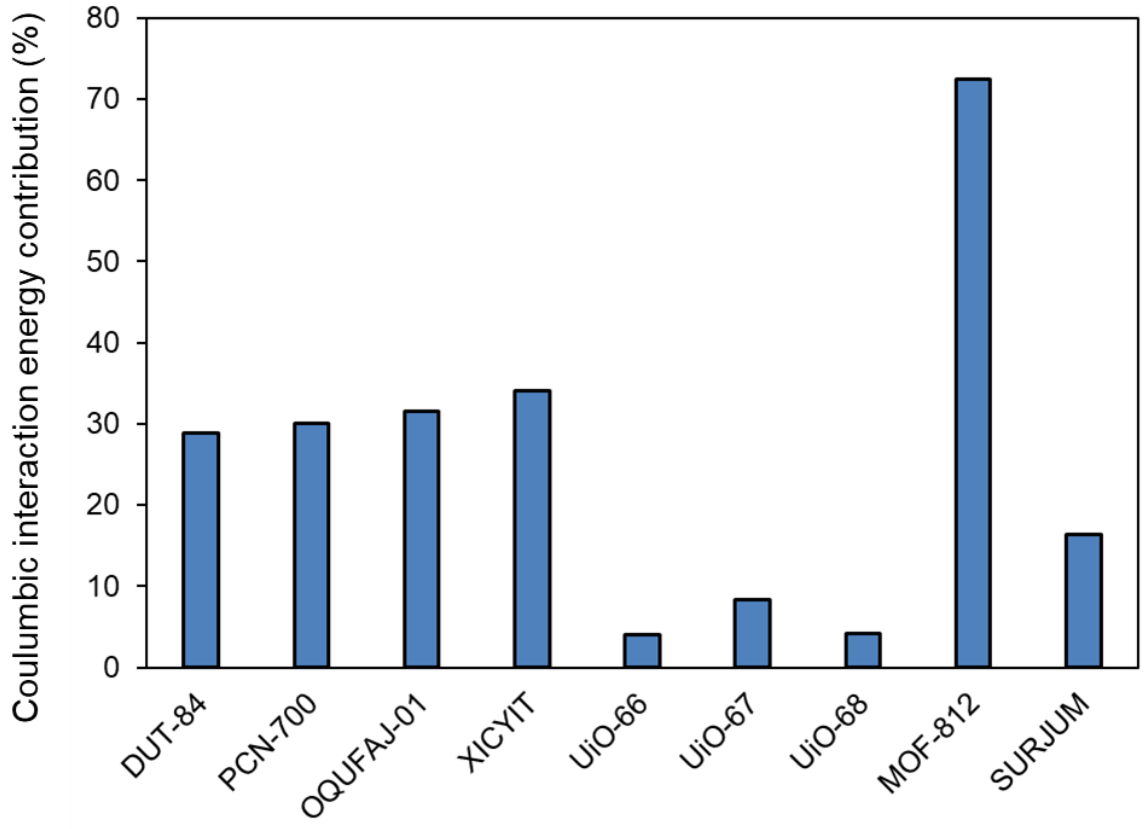

Figure S.3.8. The comparison between MOF-CO_2 Coulombic interaction energy for selected MOFs at 0.15 bar and 298 K.

References

(1) Moghadam, P. Z.; Li, A.; Liu, X.-W.; Bueno-Perez, R.; Wang, S.-D.; Wiggin, S. B.; Wood, P. A.; Fairen-Jimenez, D. Targeted Classification of Metal–Organic Frameworks in the Cambridge Structural Database (CSD). *Chem. Sci.* **2020**, *11* (32), 8373–8387. https://doi.org/10.1039/D0SC01297A.

(2) Katz, M. J.; Brown, Z. J.; Colón, Y. J.; Siu, P. W.; Scheidt, K. A.; Snurr, R. Q.; Hupp, J. T.; Farha, O. K. A Facile Synthesis of UiO-66, UiO-67 and Their Derivatives. *Chem. Commun.* **2013**, *49* (82), 9449. https://doi.org/10.1039/c3cc46105j.

(3) Dubbeldam, D.; Calero, S.; Ellis, D. E.; Snurr, R. Q. RASPA: Molecular Simulation Software for Adsorption and Diffusion in Flexible Nanoporous Materials. *Mol. Simul.* **2016**, *42* (2), 81–101. https://doi.org/10.1080/08927022.2015.1010082.

(4) Mayo, S. L.; Olafson, B. D.; Goddard, W. A. DREIDING: A Generic Force Field for Molecular Simulations. *J. Phys. Chem.* **1990**, *94* (26), 8897–8909. https://doi.org/10.1021/j100389a010.

(5) Rappe, A. K.; Casewit, C. J.; Colwell, K. S.; Goddard, W. A.; Skiff, W. M. UFF, a Full Periodic Table Force Field for Molecular Mechanics and Molecular Dynamics Simulations. *J. Am. Chem. Soc.* **1992**, *114* (25), 10024–10035. https://doi.org/10.1021/ja00051a040.

(6) Potoff, J. J.; Siepmann, J. I. Vapor–Liquid Equilibria of Mixtures Containing Alkanes, Carbon Dioxide, and Nitrogen. *AIChE J.* **2001**, *47* (7), 1676–1682. https://doi.org/10.1002/aic.690470719.

(7) Brunauer, S.; Emmett, P. H.; Teller, E. Adsorption of Gases in Multimolecular Layers. *J. Am. Chem. Soc.* **1938**, *60* (2), 309–319. https://doi.org/10.1021/ja01269a023.

(8) Gómez-Gualdrón, D. A.; Moghadam, P. Z.; Hupp, J. T.; Farha, O. K.; Snurr, R. Q. Application of Consistency Criteria To Calculate BET Areas of Micro- And Mesoporous Metal–Organic Frameworks. *J. Am. Chem. Soc.* **2016**, *138* (1), 215–224. https://doi.org/10.1021/jacs.5b10266.

(9) Rouquerol, J.; Llewellyn, P.; Rouquerol, F. Is the Bet Equation Applicable to Microporous Adsorbents? In *Characterization of Porous Solids VII*; Llewellyn, P. L., Rodriquez-Reinoso, F., Rouqerol, J., Seaton, N. B. T.-S. in S. S. and C., Eds.; Elsevier, 2007; Vol. 160, pp 49–56. https://doi.org/10.1016/S0167-2991(07)80008-5.

(10) Cavka, J. H.; Grande, C. A.; Mondino, G.; Blom, R. High Pressure Adsorption of CO_2 and CH_4 on Zr-MOFs. *Ind. Eng. Chem. Res.* **2014**, *53* (40), 15500–15507.

https://doi.org/10.1021/ie500421h.

(11) Cmarik, G. E.; Kim, M.; Cohen, S. M.; Walton, K. S. Tuning the Adsorption Properties of UiO-66 via Ligand Functionalization. *Langmuir* **2012**, *28* (44), 15606–15613. https://doi.org/10.1021/la3035352.

(12) Dovesi, R.; Erba, A.; Orlando, R.; Zicovich-Wilson, C. M.; Civalleri, B.; Maschio, L.; Rérat, M.; Casassa, S.; Baima, J.; Salustro, S.; Kirtman, B. Quantum-mechanical Condensed Matter Simulations with CRYSTAL. *WIREs Comput. Mol. Sci.* **2018**, *8* (4), e1360. https://doi.org/10.1002/wcms.1360.

(13) Manz, T. A.; Sholl, D. S. Chemically Meaningful Atomic Charges That Reproduce the Electrostatic Potential in Periodic and Nonperiodic Materials. *J. Chem. Theory Comput.* **2010**, *6* (8), 2455–2468. https://doi.org/10.1021/ct100125x.

nature communications

Article

https://doi.org/10.1038/s41467-024-48136-0

4. Gas adsorption and framework flexibility of CALF-20 explored by experiments and simulations

Rama Oktavian[1], Ruben Goeminne[2], Lawson T. Glasby[1], Ping Song[3], Racheal Huynh[3], Omid Taheri Qazvini[3], Omid Ghaffari-Nik[3], Nima Masoumifard[3], Joan L. Cordiner[1], Pierre Hovington[3], Veronique Van Speybroeck[2], Peyman Z. Moghadam[4]

[1]*Department of Chemical and Biological Engineering, The University of Sheffield, Sheffield S1 3JD, UK*
[2]*Center for Molecular Modeling (CMM), Ghent University, Technologiepark 46, 9052 Zwijnaarde, Belgium*
[3]*Svante Inc., 8800 Glenlyon Pkwy, Burnaby, BC Canada V5J 5K3*
[4]*Department of Chemical Engineering, University College London, London WC1E 7JE, UK*

Abstract

In 2021, Svante, in collaboration with BASF, reported successful scale up of CALF-20 production, a stable MOF with high capacity for post-combustion CO_2 capture and exhibits remarkable stability towards water. CALF-20's success story in the MOF commercialisation space provides new thinking about appropriate structural and adsorptive metrics important for CO_2 capture. Here, we combine atomistic-level simulations with experiments to study adsorptive properties of CALF-20 and shed light on its flexible crystal structure. We compare measured and predicted CO_2 and water adsorption isotherms and explain the role of water-framework interactions and hydrogen bonding networks in CALF-20's hydrophobic behaviour. Furthermore, regular and enhanced sampling molecular dynamics simulations are performed with both density-functional theory (DFT) and machine learning potentials (MLPs) trained to DFT energies and forces. From these simulations, the effects of adsorption-induced flexibility in CALF-20 are uncovered. We envisage this work would encourage development of other MOF materials useful for CO_2 capture applications in humid conditions.

Published in Nature Commun., 2024, 15(1) 3898.

https://doi.org/10.1038/s41467-024-48136-0

Chapter 4

4.1. Introduction

Metal-organic frameworks (MOFs), one of the most ex-citing developments in recent porous materials science, are now, more than ever, in the center of attention as they make their way successfully into industrial applications for gas adsorption and separation process.[1–5] Most adsorption applications, especially CO_2 capture from either post combustion flue gas or direct air capture are inevitably operated under humid conditions where many MOFs suffer from the competitive adsorption of water.[6–11] In 2014, Shimizu's laboratory at the University of Calgary reported a Zn-based MOF named Calgary Framework 20 (CALF-20) for physisorptive CO_2 capture under real flue gas conditions.[12] CALF-20 demonstrates an excellent CO_2 adsorption capacity of 2.6 mmol/g at 0.15 bar and 298 K, CO_2 selectivity against water of up to 40% relative humidity, as well as durability and stability to-wards steam, wet acid gases, and prolonged exposure to direct flue gas stream.[13]

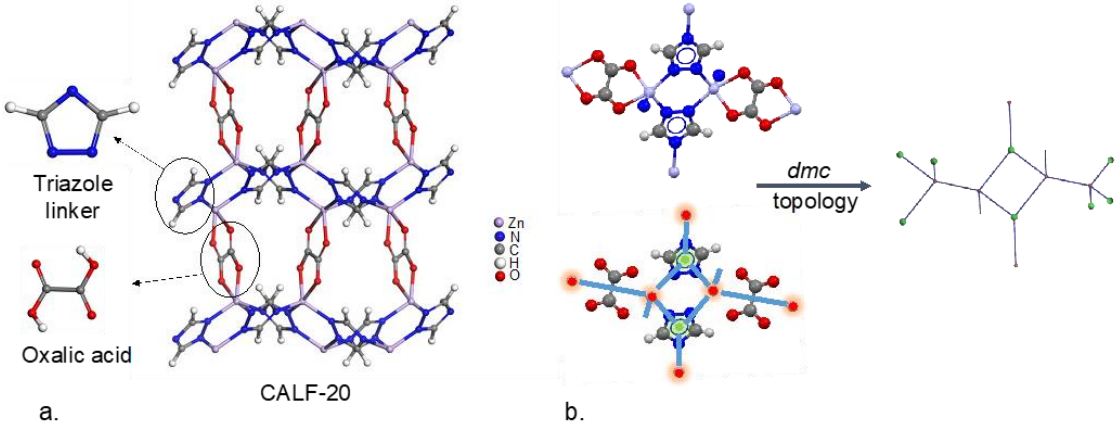

Figure 4.1. The structure and topology of CALF-20. ***a.*** *3D representation of CALF-20 along with its azolate linker and oxalate pillar.* ***b.*** *A schematic diagram showing the simplification of CALF-20 into its underlying* ***dmc*** *topology. The triazolate and oxalate linkers are disconnected from the metal nodes and simplified into 3-c and straight-through branches, respectively. The red spheres represent metallic nodes and the green spheres represent organic nodes, connected via blue linker 'branches'.*

CALF-20, shown in **Figure 4.1a**, consists of repeating layers of 1,2,4-triazoles connected by Zn atoms with oxalate ions bridging the layers. 1,2,4-triazole is well known for its water and basic environment stability; and its geometric rigidity, strong binding affinity, and high basicity has been exploited for constructing other robust MOFs.[14–20] Moreover, the scalability of CALF-20's synthesis has been demonstrated due to its relatively benign synthesis conditions. The use of methanol and water as solvents, as well as low-cost, commercially available starting materials results in high product yields of up to 90% and an exceptional space-time yield of 550 kg/m3 day.[13]

In 2021, Svante reported successful single-step commercial synthesis of CALF-20 deployed in industrial scale Temperature Swing Adsorption (TSA) process for up to 1 tonne of CO_2

removal per day from cement flue gas.[21] CALF-20 has now become the hallmark of success among MOFs undergoing the scale up process from laboratory to industry - as it ticks many of the required boxes for an optimum adsorbent for practical CO_2 capture. Developing new materials for CO_2 abatement has never been more critical and in this context, a number of research groups have started examining CALF-20 in more detail with the aim of aiding the design and development of other adsorbent materials for selective adsorption of CO_2. In late 2023, Ho and Paesani[22] and Magnin et al.[23] studied competitive adsorption and diffusion of water and CO_2 in CALF-20 via classical Monte Carlo and molecular dynamics simulations. At the same time, Chen et al.[24] looked into structural transformations of CALF-20 in humid environments via powder X-ray diffraction (PXRD) and pair distribution function analysis. In the present study, in collaboration with MOF scientists from Svante, we used a close feedback loop between simulations and experiments to obtain molecular-level insights into some of the key CO_2 adsorption properties of CALF-20, and determine its structural flexibility triggered by the presence of guest molecules. We investigated water-CALF-20 interactions through water adsorption simulations and hydrogen-bond analysis, and studied the structural transformations of CALF-20 using *in-situ* adsorption/PXRD data in combination with first-principles molecular dynamics (MD) simulations. With the aid of machine learning potentials (MLPs) trained to DFT data, fully converged free energy profiles of both the empty and guest-loaded frameworks were also computed, demonstrating the guest-induced flexibility of the framework. Importantly, in this work, we note that all the computational works were performed before laboratory synthesis and physical gas adsorption measurements were carried out by Svante. The excellent agreement between simulation and experiment provided a powerful example of the predictive ability of molecular modelling, showcased in the assessment of MOF candidates for CO_2 capture in wet conditions.

4.2. Results and Discussion

4.2.1. Geometric characterization, gas adsorption properties and structural flexibility analysis of CALF-20

To perform the simulations in this work, we used the Crystallographic Information File (CIF) from the published CALF-20 structure.[13] We first calculated the geometric properties of CALF-20 such as the surface area, pore size distribution, largest cavity diameter (LCD), pore limiting diameter (PLD) and topology. We note that computational characterisation of geometric properties can provide valuable information about the expected adsorption performance of materials and help to assess the quality of experimental samples. The LCD and

PLD values in CALF-20 are ca. 4.3 Å and 3 Å, respectively: pore size ranges that provide a tight fit for CO_2 adsorption. Figure 1.b. shows the characterisation of CALF-20's topology. The structure can be separated into C_2N_3 (triazole) and C_2O_4 (oxalic acid) linkers, with individual zinc atoms as the metallic nodes. After considering these two linker types, we simplified the structure using the SingleNode approach and arrived at the Reticular Chemistry Structure Resource (RCSR) **dmc** topology, calculated using ToposPro[25] and CrystalNets[26]

We also simulated the N_2 adsorption isotherm at 77 K and compared it with experimental measurements (**Figure 4.2a**). We found excellent agreement between the two isotherms proving that the synthesized sample was highly crystalline and successfully activated. By strictly following the BET consistency criteria[27,28], we obtained BET area of 550 m^2/g for CALF-20. **Figure 4.2.b.** shows simulated CO_2 adsorption isotherms for CALF-20 at a range of temperatures from 273 K to 387 K and compares them with experiments conducted at Svante. Overall, the predicted CO_2 uptakes are in good agreement with experimental data for the entire pressure range and across different temperatures. Flue gas typically consists of about 0.1-0.15 atmospheres of CO_2 pressure, and at these conditions, the amount of CO_2 adsorbed is ca. 0.4, 0.7, 1.3, 1.9, and 3.3 mmol/g at 387, 365, 343, 323, and 273 K respectively. Generally, the experimentally synthesized MOFs contain solvents in their pores, which can be removed upon activation. Before per-forming gas adsorption simulations, these solvent molecules can be fully removed mimicking the experimental activation process. This process assumes that the experimental activation is successful in removing all residual solvent inside the pores and the structure is not changed upon removing the solvent. Clearly, incomplete experimental activation in MOFs can reduce the accessibility to the pore space. Therefore, when solvent-free structures are used in simulations, the amount of predicted gas adsorption is usually higher than experimental measurements, given that more pore space is accessible for guest molecules.[29,30] Since the atoms in CALF-20's structure are fixed at their crystallographic positions during the simulations, underpredicting CO_2 uptake indicated to us that CALF-20 undergoes structural changes in the presence of external stimuli such as gas adsorption or temperature. Moreover, we present here the QR code (https://p3d.in/RIA6W) for the augmented reality (AR) of CO_2 adsorption snapshot in CALF-20 adapted from our previous work[31] to visualize more clearly the interaction between CO_2 molecules and framework.

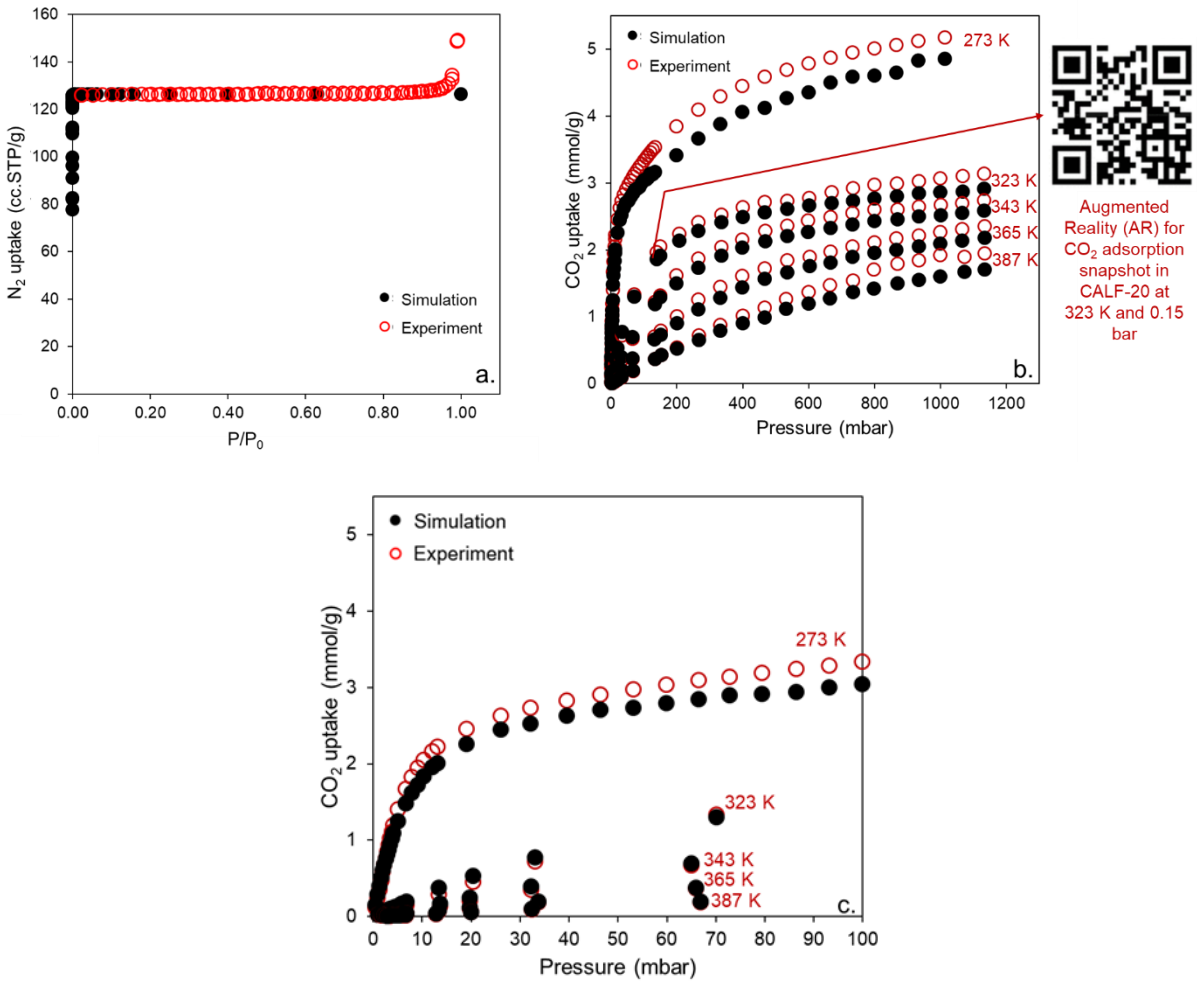

Figure 4.2. N_2 and CO_2 adsorption isotherms in CALF-20. ***a****. Experimental and simulated N_2 adsorption isotherms at 77 K in CALF-20.* ***b****. Comparison between simulated and experimental CO_2 adsorption isotherms for CALF-20 at different temperatures along with QR code for augmented reality (AR) of CO_2 adsorption snapshot at 0.15 bar and 323 K.* ***c.*** *Comparison between simulated and experimental CO_2 adsorption isotherms for CALF-20 at different temperatures and pressures up to 100 mbar. Black solid symbols represent simulation data, and red open symbols represent experiments carried out at Svante.*

To investigate potential interactions involved for guest-induced structural dynamics of CALF-20, we monitored structural transformations via in situ powder crystal X-ray diffraction (PXRD). We obtained PXRD data under different gas and liquid exposures (N_2, CO_2, water, and ethanol) and compared the results with the as-synthesized CALF-20 sample (**Figure 4.3.a**.).

The CIF from the published CALF-20 structure contains EtOH as guest molecules. Hence, when the experimentally synthesized CALF-20 powder is soaked in EtOH and then briefly dried (see Supplementary Methods 1 for the details), the PXRD obtained matches that of the simulated one. Since solvents induced substantial changes to the PXRD pattern, we evacuated CALF-20 by drying the powder *in-situ* at 110°C for 45 minutes under N_2 flow (**Figure 4.3a**), see Supplementary Methods 1 for more details.

The evacuated PXRD pattern is similar to the simulated or EtOH soaked sample, with only slight changes in the (100) and (011) reflections. The (100) plane in the simulated pattern, which corresponds to the interplanar distances between the Zn-triazolate layers in the xz-plane (**Figure 4.3.b**.), exhibits a slight shift to lower 2θ and expansion of this plane when the sample is evacuated. There is a corresponding shift in the (011) reflection, which represents the middle of the pore (**Figure 4.3c**), to a higher 2θ of the evacuated sample, suggesting a contraction along this plane. This implies that in the absence of solvent, the pores of CALF-20 as viewed along the x axis are contracted, with a corresponding expansion between the Zn-triazolate layers compared to the EtOH soaked CALF-20. We take this evacuated CALF-20 as a baseline for further guest loaded studies.

Given CALF-20's ability to selectively adsorb CO_2 over water at low relative humidity (RH), we loaded CALF-20 with water and CO_2 to observe the effects on the PXRD pattern (see Supplementary Methods 1 for experimental details). Compared to the evacuated sample, loading CALF-20 with 100% CO_2 and soaking in liquid water induced a slight shift in the (100) reflection to higher 2θ, showing contraction between the Zn-triazolate layers, similar to what is observed in the EtOH soaked sample. In addition, the (020) reflection corresponding to the planes containing the oxalate moieties (**Figure 4.3d**) shifts to lower 2θ for both water and CO_2, and it does not show much change for ethanol. In contrast, the (011) reflection remains the same in the CO_2 loaded sample, whereas a shift to lower 2θ is observed in the water soaked sample. The PXRD pattern of CALF-20 does not show significant changes at low RH (4% and 10%). At 20% RH, an obvious change of pattern was observed at (100), (011) and (020) planes. This is consistent with the reported phase change of CALF-20 in moisture.[24] Thus, H_2O accommodation requires the (011), (100) and (020) peaks to shift significantly, while CO_2 requires only the (100) and (020) reflections to move. The differences between PXRD patterns at 20%RH and water soaking indicated that water soaking might bring different changes to the structure compared to the adsorption of water vapor. Overall, water is able to bring more changes to the framework compared to all other guests discussed here. In other words, CO_2's accommodation requires less structural change than H_2O; this could explain why CALF-20 accepts CO_2 over water at low RH. A simplified explanation would be that CO_2 adsorption into CALF-20 does not require much structural adjustment of the activated phase, whereas water needs the framework to open slightly more: even before there is sufficient water to make this structural change, the CO_2 fills up, making CALF-20 more CO_2 selective. These changes in

the PXRD patterns demonstrate that CALF-20 is not a rigid and undergoes structural flexibility dependent on the guests inside the pores.

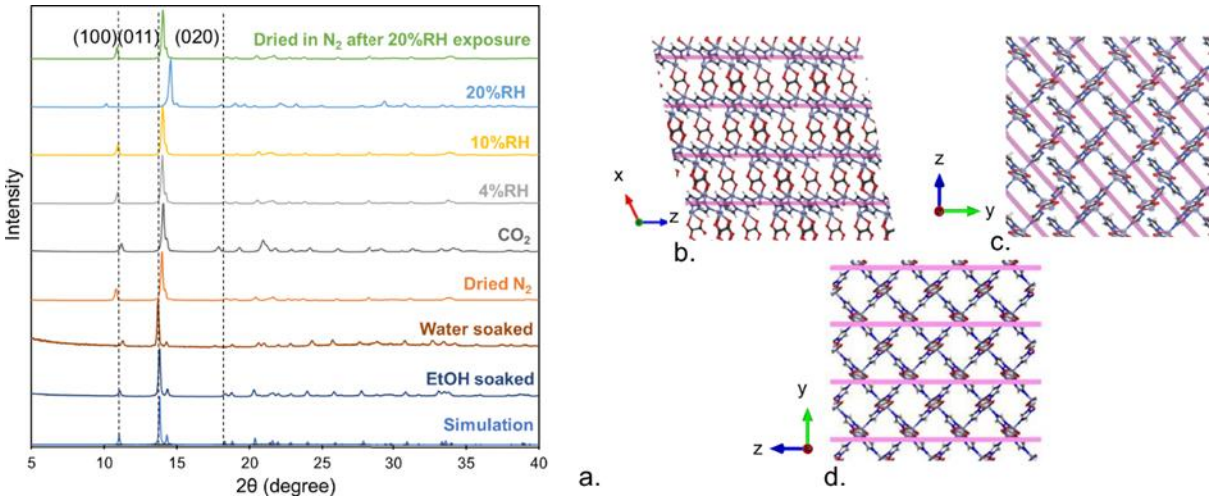

Figure 4.3. ***a*** *Comparison of PXRD patterns for CALF-20 at different adsorption conditions, and for fully dried samples under dry N_2 and CO_2 at 50 °C. For the samples under gas flow, CALF-20 was first heated to 110 °C for 30 min under dry N_2 flow to evacuate the sample. Then, the sample was cooled to 50 °C and the PXRD pattern was collected under N_2 or CO_2 flow at 50 °C. PXRD patterns under different relative humidities (%RH) were all collected in N_2. Dashed lines represent the peaks for the simulated structure. CALF-20 structure with highlighted* ***b*** *(100),* ***c*** *(011) and* ***d*** *(020) hkl planes. The pink lines represent the relevant planes. Atoms coloring scheme is: red, oxygen; blue, nitrogen; white, hydrogen; gray, carbon, and light blue, zinc.*

Simulation of MOFs exhibiting structural flexibility is challenging. Our reported GCMC simulations of gas adsorption (Figure 2) made the assumption that framework atoms are fixed at their crystallographic positions, thus we modelled CALF-20 as rigid. This assumption is valid for many MOFs whose building block topology do not allow for high degrees of flexibility. However, simulated gas adsorption predictions can deviate from experiments when MOFs are structurally flexible in response to external stimuli such as temperature or guest loading.[32] Here, to further investigate the effects of adsorption-induced flexibility in CALF-20, we also performed MD simulations at the density-functional (DFT) level of theory (PBE-D3(BJ)) using CP2K.[33] By comparing MD simulations of both the empty and the guest-loaded CALF-20 framework at experimentally observed loadings, the effect of guests on the framework can be directly determined. Simulations were performed in the NPT ensemble (controlling the temperature and pressure, allowing the cell shape to fluctuate) with a 2x2x2 supercell of CALF-20 at 273 K, 323 K, and 387 K for a duration of 20 ps with a time step of 1 fs. From these MD trajectories, we computed histograms of the cell volume, cell lengths, pore volumes and pore size distributions, as shown in **Figure 4.4**.

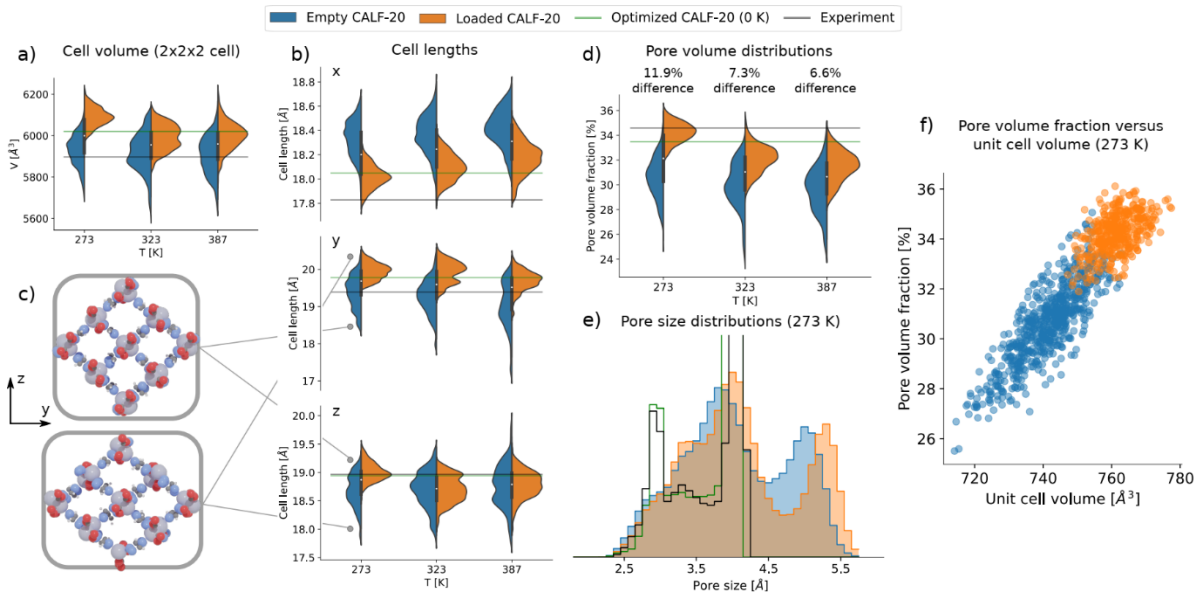

Figure 4.4. CALF-20 structural changes characterised via first-principles molecular dynamics simulations. Distributions of ***a.*** *cell volume (2x2x2) cell,* ***b.*** *cell lengths, and* ***d.*** *pore volume obtained from MD simulations of the empty (blue) and guest-loaded framework (orange) at 273 K, 323 K, and 387 K, compared to the values of the DFT optimized framework (green) and the experimentally resolved structure (black).* ***c****. Two snapshots from MD simulations demonstrating the variability of the cell vectors perpendicular to the Zn-triazolate layers. Atom colouring scheme is: light grey, zinc; red, oxygen; white, hydrogen; blue: nitrogen; grey: carbon).* ***e****. Pore size distributions of the experimental structure (black), the DFT optimized structure (green), and those averaged over MD trajectories of the empty and guest-loaded CALF-20 at 273 K.* ***f.*** *Pore volume fraction as a function of the unit cell volume for the empty CALF-20 framework (blue) and the CO_2 loaded framework (orange) at 273 K.*

Firstly, consider the cell lengths shown in **Figure 4.4.b**. For the empty framework there is most variability along the y and z-axis, perpendicular to the Zn-triazolate layers. To illustrate this, two snapshots of the framework are extracted from the MD simulations, the yz-plane of which is shown in **Figure 4.4.c.**, with cell lengths annotated on **Figure 4.4.b**.We can see there is significant flexibility where one of the cell lengths varies inversely with the other: this corroborates with the differences observed in the PXRD patterns of CALF-20 upon exposure to guests (**Figure 4.3**). This flexible mode is significantly inhibited when guests are present in the framework, as can be seen from the narrower orange distributions in **Figure 4.4.b**.

Secondly, the previous conclusion can also be drawn from the volume histograms in **Figure 4.4.a**. The difference between the guest-loaded and empty framework is largest at 273 K, at which the most guests are adsorbed. The adsorbed guests hold open the framework, resulting in a volume of 6,089 $Å^3$, compared to a volume of 5,930 $Å^3$ for the empty CALF-20. Even though this difference of 2.7% appears quite small, the effect is much more pronounced when considering the pore volume fraction of the framework, shown in **Figure 4.4.d**. This fraction is equal to the volume accessible in the framework for a nitrogen probe divided by the total volume, as computed from PoreBlazer.[34] This fraction is a measure for the amount of space accessible for guest molecules. At 273 K, the difference between the pore volume fractions of

the empty and loaded frameworks is 11.9%, compared to 7.3% at 323 K and 6.6% at 387 K. The adsorbed guests clearly increase the pore volume available in the framework, expanding the space for more adsorbates, consistent with the hypothesis that the difference between the experimental observations and the GCMC simulations at 273 K is due to the ability of the framework to adapt to the presence of guests.

Lastly, the pore size distributions at 273 K are shown in **Figure 4.4.e**. Comparing the empty and guest-loaded frameworks in blue and orange, it is observed that the presence of guests increases the size of the largest pores in the framework, holding the material open. The correlation between the cell volume and pore volume fraction of the empty and guest-loaded framework is shown in **Figure 4.4.f**. Large spreads across these quantities can be seen for both the empty and guest-loaded framework suggesting that a thorough characterization of the adsorption properties for both should include this variation.

Empty and guest-loaded DFT free energy profiles

These initial results indicate that the framework shows a degree of flexibility upon guest adsorption. To determine the relative stability of the framework at different volumes in the presence of guest adsorbates and at different temperatures, the free energy profiles can be derived.[35] However, as the construction of these profiles at the PBE-D3(BJ) level of theory is computationally excessively demanding, machine learning potentials (MLPs) were used instead in the following way. First, short (2 ps) DFT metadynamics simulations were performed on the 2x2x2 CALF-20 supercell with the cell volume as a collective variable to explore the space of possible states of the framework. Within these simulations, all relevant volumes of the framework were sampled. Then, short DFT umbrella sampling simulations lasting 0.5 ps were performed, restrained at volumes between 4000 and 7000 $Å^3$ with a step of 50 $Å^3$, and a temperature of 500 K. Snapshots are taken every 5 fs from these simulations and together make up the training set for the MLP (using NequIP[35]). The approach of generating enhanced sampling DFT MD data for training an MLP has been successfully applied before to model the flexibility of MOFs.[36] The training error on the MLP was 0.13 meV per atom on the energy and 28.3 meV/˚ A on the forces. With the trained MLP, longer (15 ps) umbrella sampling simulations were then performed at 223 K, 273 K, and 387 K again at volumes between 4000 and 7000 $Å^3$ with a step of 50 $Å^3$. The calculated free energy profiles at these three temperatures are shown in **Figure 4.5.a**.

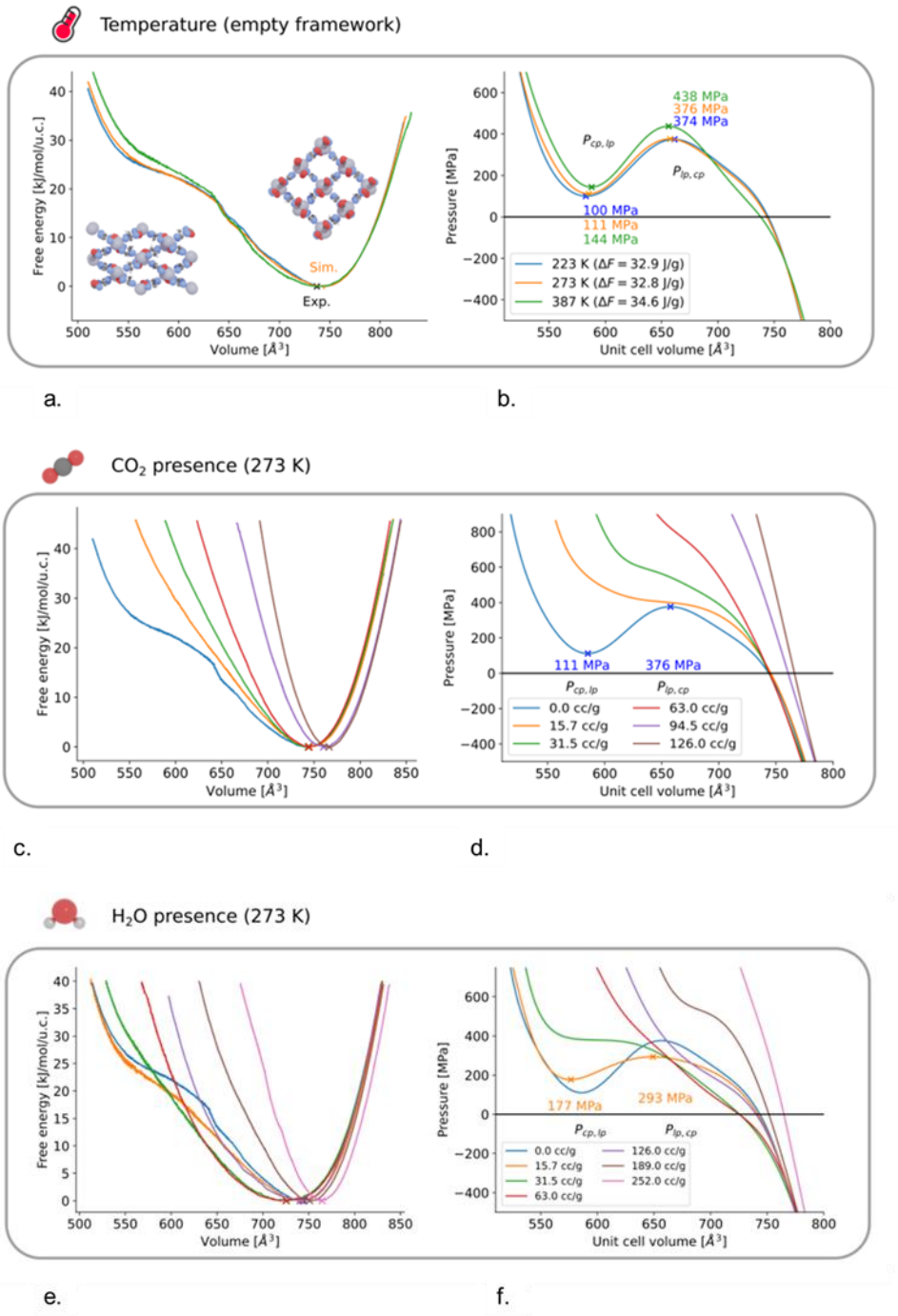

Figure 4.5. Free energy profiles of the empty and guest-loaded CALF-20. ***a****. Free energy profiles as a function of the unit cell volume of the empty CALF-20 framework at temperature of 223 K, 273 K, and 387 K. The inset shows closed pore (cp) and large pore (lp) structures.* ***b****. Internal pressure of the framework, calculated as the negative derivative of the free energy, revealing the possibility of a metastable cp phase at a volume of 585 Å³; Free energy profiles of* ***c****. CO_2-loaded and* ***e****. water-loaded CALF-20 framework at different loadings; Internal pressure of the framework in* ***d****. CO_2-loaded CALF-20;* ***f****. water-loaded CALF-20.*

The predicted unit cell volume at 273 K agrees very well with the experimentally obtained volume. Furthermore, temperature only has a moderate effect on the relative stability of the framework. In **Figure 4.5.b**, the internal pressure (negative derivative of the free energy) is shown as function of the unit cell volume. From the simulations, the existence of a metastable

closed pore (cp) is predicted at a unit cell volume of 585 $Å^3$. This cp phase can be reached by applying a mechanical pressure larger than the transition pressure (376 MPa at 273 K). This metastable cp phase only disappears, with a transition back to the large pore (lp) being predicted, when lowering the mechanical pressure to below the cp—lp transition pressure (111 MPa at 273 K). Such phase transitions have not been observed experimentally, but this could be due to the large magnitude of the transition pressures required.

The method to predict the free energy profiles of the empty framework was also used to predict the free energy of the CO_2-loaded framework. Again, training data at a CO_2 loading of 15.7 cc/g, 31.5 cc/g, 63.0 cc/g, 94.5 cc/g, and 126 cc/g were generated, MLPs were trained, and MLP umbrella sampling simulations were performed. The resulting free energy profiles are shown in **Figure 4.5.c**. As expected from the results in **Figure 4.4**, higher guest loadings make the space of accessible volumes narrower, as well as shifting the equilibrium unit cell volume upwards. From the empty framework to the guest-loaded framework at 126 cc/g, the equilibrium volume shifts from 744 $Å^3$ to 766 $Å^3$. Furthermore, as seen from the pressure profiles in **Figure 4.5.d**, the presence of guest molecules removes the possibility of a metastable cp phase being reached under the application of mechanical pressure. This can be rationalized from the lower possible pore volume in the cp phase, hindering the presence of guest molecules. However, these conclusions could change when loading the framework with water instead as the oxalic acid linkers could interact strongly with present water adsorbates, possibly even stabilizing the lower-volume cp phase instead of destabilizing it, as is the case for carbon dioxide. Subsequently, we expanded this investigation by including H_2O guests as water was suspected to be able to stabilize lower-volume states of the framework more than CO_2. The same simulations as CO_2 were performed for H_2O as guest at a range of loadings. The results of these additional simulations are shown in **Figure 4.5.e—f**.

Comparing the free energy profiles of the CO_2-loaded and the H_2O-loaded framework reveals some interesting differences. First of all, low H_2O loadings indeed stabilized lower framework volumes, where this is not seen for CO_2. This stabilization also affects the transition pressure that would be required to trigger a phase transition from the lp to cp phase. At the lowest loading of 15.7 cc/g, the transition pressure is lowered to 293 MPa, compared to 376 MPa for the empty framework.

Moreover, a larger spread of lp volumes is predicted under water adsorption compared to CO_2. However, for water, a non-monotonic behavior is observed. The free energy minimum first decreases from 744 $Å^3$ to 725 $Å^3$ at intermediate loadings (31.5 cc/g), and subsequently

increases to 764 $Å^3$ at the highest loading. This demonstrates how, at intermediate water loadings, lower volumes are stabilized. Only when further increasing the water loadings are larger volumes again stabilized. This is consistent with our hypothesis that water, through its stronger interactions with the oxalate linkers, can more effectively stabilize the lower framework volumes than CO_2. Simulated PXRD patterns for guest-induced CALF-20 structures are shown in **Supplementary Figure 4.1**. Similar to experimental PXRDs shown in **Figure 4.3.a**, simulated PXRDs also clearly show global flexibility for CO_2- and water-induced CALF-20 structures, demonstrated by the different patterns obtained from five representative framework snapshots during the NPT simulations.

From the free energy calculations, we also analysed the rotation of the traizolate linkers in the empty, CO_2-loaded and H_2O-loaded CALF-20 structures. Essentially, we considered the angle between the normal on the plane defined by the linker and the YZ-plane, which determines how much the linker is rotated to "obstruct" the pore along the X-axis (see **Supplementary Figure 4.2**). For the experimental structure, this angle is ca. 21° whereas the calculation of the angle distributions for the empty, CO_2-loaded and H_2O-loaded CALF-20 structures yields a wide range of values up to 60°. Interestingly, the H_2O-loaded structure exhibit larger angles with peaks of around 30-40° compared to those for the empty (10-20°) and CO_2-loaded (20-30°) structures. This means that with water loading, the imidazolate linker is further rotated compared to the CO_2-loaded structure. This finding suggests the high CO_2 selectivity of the framework with respect to water, as water likes a more rotated imidazole angle to optimize its interactions with the framework. However, when CO_2 is present, this rotation is somewhat inhibited.

4.2.2. Water adsorption in CALF-20

Water is a ubiquitous component in flue gas and often adversely affects the efficiency of adsorbents because it can be preferentially adsorbed over CO_2. This phenomenon depends on the relative binding affinity of CO_2 and water with the adsorbent which is related to the heat of adsorption. The heat of adsorption for water is often high and the initial adsorbed molecules can seed and attract more water molecules through formation of strong intermolecular hydrogen bonds. This often results in a sudden and sharp increase in the water uptake reaching saturation. To evaluate the water-framework and water-water interactions at different levels of humidity, we began by simulating water adsorption in CALF-20 and compared the results with experiments at 293 K (**Figure 6.a**). We found a reasonably good agreement between the

experiments and simulations throughout the entire pressure range. In particular, the simulations predict the shape of the type-V isotherm typical of hydrophobic adsorbents, with poor water-sorbent interactions and relatively stronger intermolecular attraction. Both simulations and experiments show the inflection point below 20% RH with saturation loading of around 11 mmol/g: these findings are similar to water adsorption data previously reported by Lin et al.[13] **Supplementary Figure 4.3.a** shows the predicted heat of adsorption versus water loading in molecules/unit cell of CALF-20. Overall, the heat of adsorption increases as more water molecules adsorbed in CALF-20 from ca. 37—40 kJ/mol at low loadings (1 molecules/unit cell) to ~50 kJ/mol at higher loadings of ca. 8 molecules/unit cell. We also investigated the breakdown of water-water and water-framework van der Waals (vdW) and electrostatic interactions for water adsorption in CALF-20 (**Supplementary Figures 4.3.b-c**). Electrostatic interactions account for ca. 73% of the total energy when water-MOF interactions are compared (**Supplementary Figure 4.3.c**). Electrostatic interactions between water molecules are also dominant and increase from 5 kJ/mol to around 30 kJ/mol when the RH increases from 5% to 80%.

To investigate water adsorption sites in CALF-20, we analysed the simulation snapshots for water and studied the distance between water molecules and CALF-20's Zn and O atoms through analysis of the Radial Distribution Function (RDF). **Figure 4.6.b** compares the RDF of atom pairs between Zn and O atoms in CALF-20 with the O atom in water at 10% RH where the initial water molecules are adsorbed. The first peak appears at a distance of 2.8 Å and corresponds to the distance between O of water and O of CALF-20 demonstrating that water molecules sit next to the oxygen atoms from the oxalate linkers. The distance between the Zn, and O of water occurs at larger distances of ca. 4 Å which indicates lack of direct contact with the metal atoms and explains why the material does not adsorb significant amount of water at low levels of humidity. **Figure 4.6.c** shows the simulation snapshot for water adsorption in CALF-20 at 10% RH. Water molecules are adsorbed close to the oxalate pillars of CALF-20 rather than the metal clusters in agreement with the RDF results. To better understand the water adsorption mechanism in CALF-20 we studied how water forms clusters in the pores of CALF-20 and compared it with water adsorption behavior in Cu-BTC, a representative hydrophilic MOF. To achieve this, we calculated the distribution of hydrogen bonds at different relative humidities averaged over the production cycles. To calculate the number of hydrogen bonds, we used a geometric criterion described by Xu et al.[37] In these calculations, a pair of water molecules is considered hydrogen bonded if the O-O distance is below 3.5 Å and

simultaneously the O-H…O angle is greater than 150°. Using this criterion we obtained the hydrogen bond distributions for different water loadings in CALF-20 shown in **Figure 4.6.d**. At relative humidities less than 20%, water molecules are far apart and form zero or, at most, one hydrogen bond. At higher relative humidities (80%), after condensation occurs, water molecules start to interact but only begin to form one or two hydrogen bonds per water molecule. This indicates that water molecules are more spread out in the pore space and clustering becomes less probable within the small pores of CALF-20. However, at high RH values in Cu-BTC, we observe up to three and four hydrogen bonds per water molecule, indicating a strong tendency for clustering (**Figure 4.6.e**). In liquid water (red), molecules construct mainly four hydrogen bonds, forming tetrahedral conformations of water clusters. In general, when compared with bulk water, we observe a reduction in the dominant number of hydrogen bonds in the adsorbed phase from four to three in Cu-BTC, and from four to two in CALF-20. These findings are also supported by the water adsorption snapshots displayed in **Figure 4.6.c** where the hydrogen bonds are schematically illustrated. Overall, the hydrophobicity observed in CALF-20 at low RH is related to the lack of sufficient force from water to open the framework and accommodate enough water to favor direct cooperative contact between water molecules, the lack of water's direct contact with the Zn atoms, as well as pore confinement effects for which strong hydrogen bonding between neighboring water molecules cannot occur.

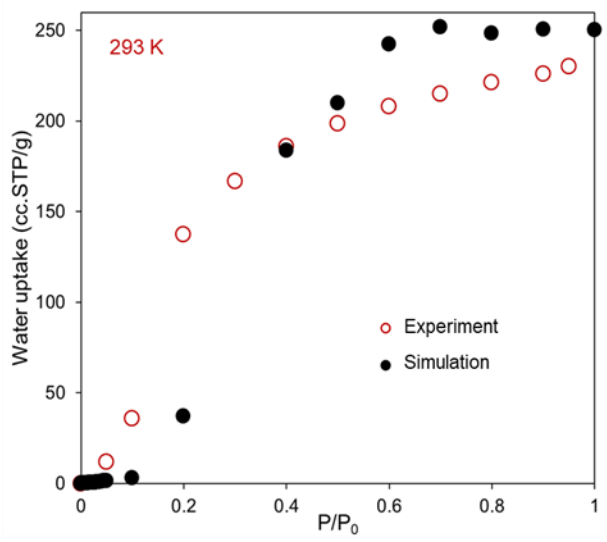

a.

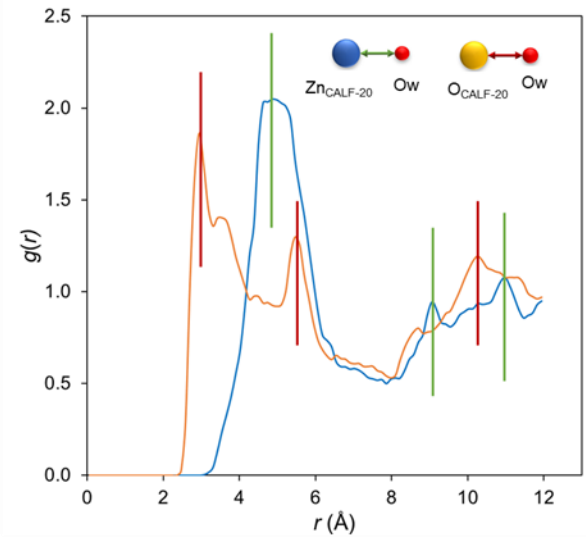

b.

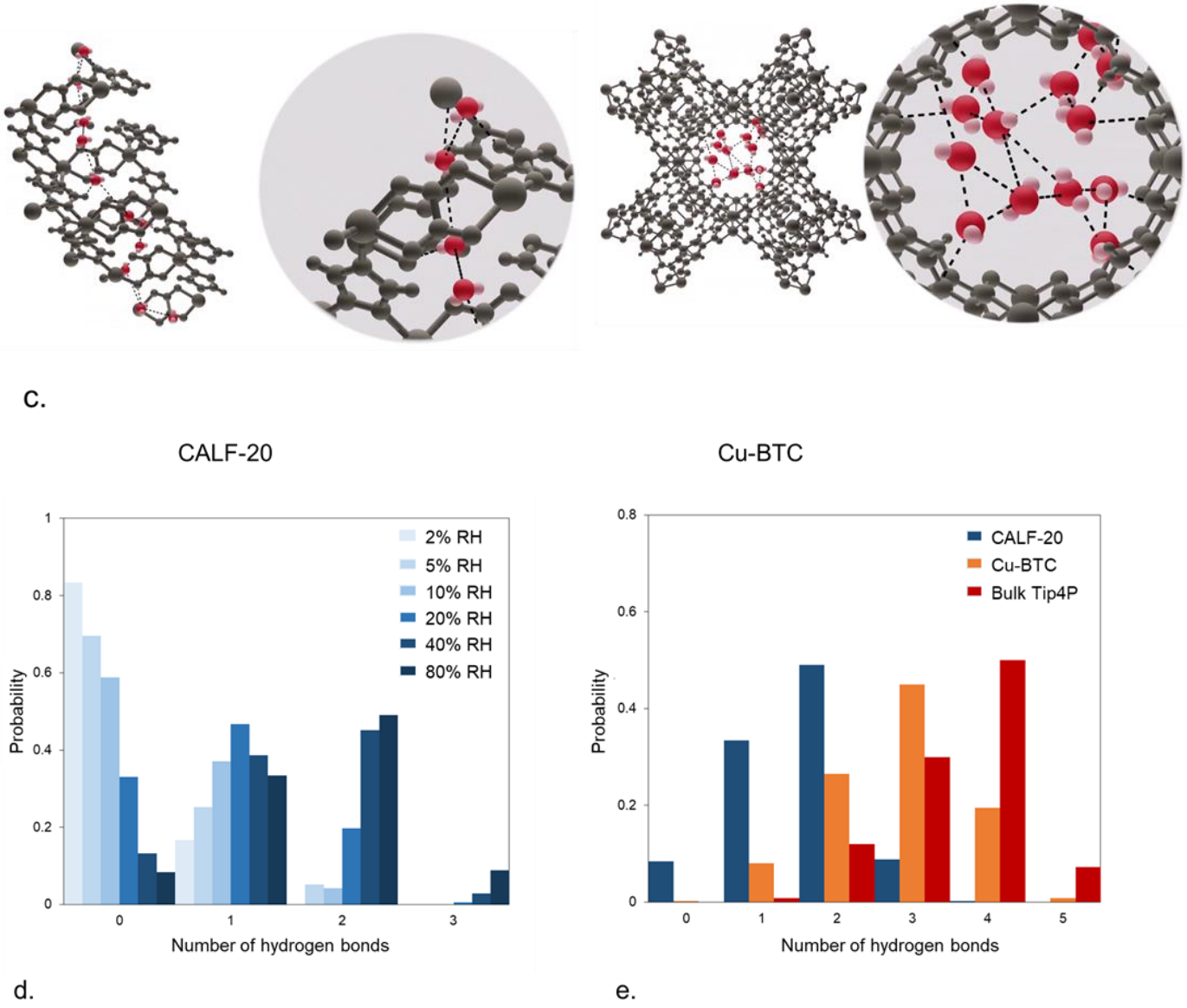

Figure 4.6. Characterisation of water adsorption and hydrogen bonds in CALF-20. ***a.*** *Simulated and experimental water adsorption isotherms in CALF-20 at 293 K.* ***b.*** *Radial distribution functions between framework Zn and O atom and O atom in water for 10% RH and 293 K.* ***c.*** *Simulation snapshot at 10% RH (oxygen, red ball and stick representation; hydrogen, white; carbon, grey; nitrogen, blue; zinc, purple) and water molecule clustering comparison between CALF-20 and Cu-BTC.* ***d.*** *Distribution of the number of hydrogen bonds for different levels of relative humidity (RH) in CALF-20.* ***e.*** *Distribution of the number of hydrogen bonds for water at 80% RH for CALF-20 compared with water in Cu-BTC and bulk TIP4P liquid water.*

In summary, CALF-20 is an outstanding water stable structure capable of selectively separating CO_2 from flue gas. Here, we provide an in-depth study of the gas adsorption properties and framework flexibility of CALF-20 combining different simulation and experimental techniques. The unexpected underprediction of CO_2 adsorption, when compared with experiments, suggested structural changes in the presence of gas molecules most notably at 273 K. CALF-20's framework flexibility was explored using experimental gas adsorption and PXRD data in combination with molecular dynamics simulations at the DFT level. At 273 K, the difference between the pore volume fractions of the empty and CO_2-loaded framework was

calculated to be ca. 12% demonstrating that the adsorbed guests clearly increase the pore space for more adsorbates, consistent with the hypothesis that the difference between the experimental observations and the Monte Carlo simulations is due to the flexibility of the framework under guest-adsorption. Furthermore, the complete free energy profiles of the empty and guest-loaded frameworks were computed, making use of machine learning potential (MLPs) trained to enhanced sampling DFT data, demonstrating the induced flexibility of the framework under guest adsorption. We note that, our approach of generating training data for an MLP at the DFT level to fully characterize the framework flexibility as a function of temperature and guest adsorption has the promise to be extended widely to other nanoporous materials. The investigation of guest-induced framework flexibility at the DFT level has mostly been limited to energy optimizations.[38] In contrast, trained MLPs can be used at a significantly reduced computational costs, allowing for the first principles construction of temperature and guest-loading dependent free energy profiles. In this way, the behavior of MOFs can be characterized at the relevant operating conditions. Based on the analysis, the flexibility of CALF-20 is mainly exhibited due to the presence of guest molecule. Furthermore, recent implementations of active learning loops for MLP training can further reduce the required number of DFT evaluations, enabling wide-scale applications to the field of nanoporous materials.[39] The investigation into the hydrophobic nature of CALF-20 showed that water molecules do not interact directly with the Zn and instead prefer to sit inside the small pores, as evidenced by simulation snapshots and radial distribution function analysis. The analysis of the hydrogen bond network showed that water molecules are spread out in the tightly confined pores of CALF-20 which inhibits formation of more than two hydrogen bonds per water molecule and therefore water clustering is less probable. In conclusion, we demonstrated a great example of collaboration and feedback between computational and experimental MOF researchers to encourage identification and characterization of other hydrophobic MOF materials useful for CO_2 capture applications.

4.3. Methods

4.3.1. GCMC simulations of gas adsorption in CALF-20

Gas adsorption simulations were carried out via the grand canonical Monte Carlo (GCMC) calculations performed in RASPA-2.0 code.[40] In the GCMC simulations, insertion, deletion, and translation and rotation moves were attempted with equal probability. The interactions between the gas species and the framework were modelled using Lennard–Jones (LJ) plus

Coulomb potentials. LJ parameters for all atoms in MOFs were taken from Dreiding force field (DFF)[41] and were truncated at a cut-off radius of 12.8 Å. The force field parameters for the adsorbates and CALF-20 are tabulated in **Supplementary Tables 4.1-4.4** in the supporting information. The Lorentz-Berthelot mixing rules were used to calculate cross interactions. Partial atomic charges for CALF-20 were calculated using the REPEAT (Repeating Electrostatic Potential Extracted Atomic) method.[42] and the Ewald summation technique was used to calculate electrostatic interactions. GCMC simulations for N_2 and CO_2 adsorption were run for 20,000 cycles for equilibration and a further 20,000 cycles to average properties. N_2 and CO_2 were modelled using the TraPPE model.[43] Water was modelled using the TIP4P force field.[44] The model was selected in this study for the comparison to the previous study on water adsorption in CALF-20.[13] For water simulations we used 100,000 cycles for equilibration and subsequent 100,000 cycles for production. Water was modelled using the TIP4P force field.[44] The relative humidity of 100% corresponds to the saturation pressure of the TIP4P model.

4.3.2. (MLP) MD simulations of the empty and guest-loaded CALF-20

To assess the flexibility of the CALF-20 framework, NPT MD simulations with a fully flexible unit cell were performed for both the empty and guest-loaded frameworks at 273 K, 323 K, and 387 K with the PBE-D3(BJ) level of theory using the CP2K software package (version 7.1).[33] A plane wave energy cutoff of 500 Ry and GTH pseudopotentials were used, employing the TZVP-MOLOPT basis set. Simulations were performed for a duration of 20 ps.

To compute the free energy profiles of the empty and guest-loaded framework, machine learning potentials (MLPs) were trained and employed to significantly reduce the required computational resources. First, DFT metadynamics simulations are performed for 2 ps on the 2x2x2 CALF-20 supercell (both empty framework and guest-loaded frameworks) with the cell volume as a collective variable to explore the space of possible states of the framework. In these simulations, Gaussian hills with a height of 10 kJ/mol and a width of 50 $Å^3$ are added every 25 fs. For both the empty and guest-loaded framework, short (0.5 ps) DFT umbrella sampling (US) simulations of the 2x2x2 supercells were then performed, restrained with a bias potential with a strength of 0.005 kJ/$Å^6$ at volumes between 4000 $Å^3$ and 7000 $Å^3$ with a step of 50 $Å^3$. PLUMED was used to apply the bias potential.[45,46]

The energy and forces of snapshots extracted from these simulations every 5 fs were then used to train a NequIP model.[36] A model was trained separately for each guest-loading. The dataset was randomly divided into a training and validation set with a 90:10 ratios. The MLPs

were trained making use of a cutoff radius of 5 Å, 4 interaction blocks, a maximum rotation order of 1 and 64 features. The loss function contains both energies (with weight 1) and forces (with weight 5). For all MLPs, a validation error lower than 0.13 meV per atom for energies and 39.6 meV/Å for forces were obtained. With the trained MLPs, US MLP MD simulations were performed, restrained at the same set of volumes as performed with CP2K,[33] for a duration of 15 ps. To obtain the unbiased free energy profiles, the weighted histogram analysis method (WHAM) was used.[47] The internal pressure as a function of the volume was derived by fitting a 12th order polynomial to the free energy profiles, and computing the negative derivative with respect to the volume.[35]

Student's contribution: Performing simulation and calculation for N_2, CO_2 and H_2O adsorption isotherms in CALF-20 using GCMC simulation protocol. Student also perform the analysis of the distribution of the hydrogen bond number of water in CALF-20. In addition, student successfully published this work in the journal as the first author preparing the first draft of submitted manuscript.

References

(1) Silva, P.; Vilela, S. M. F.; Tomé, J. P. C.; Almeida Paz, F. A. Multifunctional Metal–Organic Frameworks: From Academia to Industrial Applications. *Chem. Soc. Rev.* **2015**, *44* (19), 6774–6803. https://doi.org/10.1039/C5CS00307E.

(2) Czaja, A. U.; Trukhan, N.; Müller, U. Industrial Applications of Metal–Organic Frameworks. *Chem. Soc. Rev.* **2009**, *38* (5), 1284. https://doi.org/10.1039/b804680h.

(3) Chen, Z.; Wasson, M. C.; Drout, R. J.; Robison, L.; Idrees, K. B.; Knapp, J. G.; Son, F. A.; Zhang, X.; Hierse, W.; Kühn, C.; Marx, S.; Hernandez, B.; Farha, O. K. The State of the Field: From Inception to Commercialization of Metal–Organic Frameworks. *Faraday Discuss.* **2021**, *225* (0), 9–69. https://doi.org/10.1039/D0FD00103A.

(4) Faust, T. MOFs Move to Market. *Nat. Chem.* **2016**, *8* (11), 990–991. https://doi.org/10.1038/nchem.2656.

(5) Ryu, U.; Jee, S.; Rao, P. C.; Shin, J.; Ko, C.; Yoon, M.; Park, K. S.; Choi, K. M. Recent Advances in Process Engineering and Upcoming Applications of Metal–Organic Frameworks. *Coord. Chem. Rev.* **2021**, *426*, 213544. https://doi.org/https://doi.org/10.1016/j.ccr.2020.213544.

(6) Boyd, P. G.; Chidambaram, A.; García-Díez, E.; Ireland, C. P.; Daff, T. D.; Bounds, R.; Gładysiak, A.; Schouwink, P.; Moosavi, S. M.; Maroto-Valer, M. M.; Reimer, J. A.; Navarro, J. A. R.; Woo, T. K.; Garcia, S.; Stylianou, K. C.; Smit, B. Data-Driven Design of Metal–Organic Frameworks for Wet Flue Gas CO_2 Capture. *Nature* **2019**, *576* (7786), 253–256. https://doi.org/10.1038/s41586-019-1798-7.

(7) Benoit, V.; Chanut, N.; Pillai, R. S.; Benzaqui, M.; Beurroies, I.; Devautour-Vinot, S.; Serre, C.; Steunou, N.; Maurin, G.; Llewellyn, P. L. A Promising Metal–Organic Framework (MOF), MIL-96(Al), for CO_2 Separation under Humid Conditions. *J. Mater. Chem. A* **2018**, *6* (5), 2081–2090. https://doi.org/10.1039/C7TA09696H.

(8) Kolle, J. M.; Fayaz, M.; Sayari, A. Understanding the Effect of Water on CO_2 Adsorption. *Chem. Rev.* **2021**, *121* (13), 7280–7345. https://doi.org/10.1021/acs.chemrev.0c00762.

(9) Mason, J. A.; McDonald, T. M.; Bae, T.-H.; Bachman, J. E.; Sumida, K.; Dutton, J. J.; Kaye, S. S.; Long, J. R. Application of a High-Throughput Analyzer in Evaluating Solid Adsorbents for Post-Combustion Carbon Capture via Multicomponent Adsorption of CO_2, N_2, and H_2O. *J. Am. Chem. Soc.* **2015**, *137* (14), 4787–4803. https://doi.org/10.1021/jacs.5b00838.

(10) Masala, A.; Vitillo, J. G.; Mondino, G.; Grande, C. A.; Blom, R.; Manzoli, M.; Marshall, M.; Bordiga, S. CO_2 Capture in Dry and Wet Conditions in UTSA-16 Metal–Organic Framework. *ACS Appl. Mater. Interfaces* **2017**, *9* (1), 455–463. https://doi.org/10.1021/acsami.6b13216.

(11) Kim, E. J.; Siegelman, R. L.; Jiang, H. Z. H.; Forse, A. C.; Lee, J.-H.; Martell, J. D.; Milner, P. J.; Falkowski, J. M.; Neaton, J. B.; Reimer, J. A.; Weston, S. C.; Long, J. R. Cooperative Carbon Capture and Steam Regeneration with Tetraamine-Appended Metal–Organic Frameworks. *Science.* **2020**, *369* (6502), 392–396. https://doi.org/10.1126/science.abb3976.

(12) Shimizu, G. K. H.; Vaidhyanathan, R.; Iremonger, S. S.; Deakin, K.; Lin, J.-B.; Dawson, K. W. Metal Organic Framework, Production and Use Thereof. WO2014138878A1, 2014.

(13) Lin, J.-B.; Nguyen, T. T. T.; Vaidhyanathan, R.; Burner, J.; Taylor, J. M.; Durekova, H.; Akhtar, F.; Mah, R. K.; Ghaffari-Nik, O.; Marx, S.; Fylstra, N.; Iremonger, S. S.; Dawson, K. W.; Sarkar, P.; Hovington, P.; Rajendran, A.; Woo, T. K.; Shimizu, G. K. H. A Scalable Metal-Organic Framework as a Durable Physisorbent for Carbon Dioxide Capture. *Science.* **2021**, *374* (6574), 1464–1469. https://doi.org/10.1126/science.abi7281.

(14) Shi, Z.; Tao, Y.; Wu, J.; Zhang, C.; He, H.; Long, L.; Lee, Y.; Li, T.; Zhang, Y.-B. Robust Metal–Triazolate Frameworks for CO_2 Capture from Flue Gas. *J. Am. Chem. Soc.* **2020**, *142* (6), 2750–2754. https://doi.org/10.1021/jacs.9b12879.

(15) Demessence, A.; D'Alessandro, D. M.; Foo, M. L.; Long, J. R. Strong CO_2 Binding in a Water-Stable, Triazolate-Bridged Metal−Organic Framework Functionalized with Ethylenediamine. *J. Am. Chem. Soc.* **2009**, *131* (25), 8784–8786. https://doi.org/10.1021/ja903411w.

(16) Li, S.; Zeng, S.; Tian, Y.; Jing, X.; Sun, F.; Zhu, G. Two Flexible Cationic Metal-Organic Frameworks with Remarkable Stability for CO_2/CH_4 Separation. *Nano Res.* **2021**, *14* (9), 3288–3293. https://doi.org/10.1007/s12274-021-3329-8.

(17) Zhang, J.-P.; Zhang, Y.-B.; Lin, J.-B.; Chen, X.-M. Metal Azolate Frameworks: From Crystal Engineering to Functional Materials. *Chem. Rev.* **2012**, *112* (2), 1001–1033. https://doi.org/10.1021/cr200139g.

(18) Vaidhyanathan, R.; Iremonger, S. S.; Shimizu, G. K. H.; Boyd, P. G.; Alavi, S.; Woo, T. K. Direct Observation and Quantification of CO_2 Binding Within an Amine-

Functionalized Nanoporous Solid. *Science.* **2010**, *330* (6004), 650–653. https://doi.org/10.1126/science.1194237.

(19) Rosen, A. S.; Mian, M. R.; Islamoglu, T.; Chen, H.; Farha, O. K.; Notestein, J. M.; Snurr, R. Q. Tuning the Redox Activity of Metal–Organic Frameworks for Enhanced, Selective O_2 Binding: Design Rules and Ambient Temperature O_2 Chemisorption in a Cobalt–Triazolate Framework. *J. Am. Chem. Soc.* **2020**, *142* (9), 4317–4328. https://doi.org/10.1021/jacs.9b12401.

(20) Rosen, A. S.; Notestein, J. M.; Snurr, R. Q. High-Valent Metal–Oxo Species at the Nodes of Metal–Triazolate Frameworks: The Effects of Ligand Exchange and Two-State Reactivity for C−H Bond Activation. *Angew. Chemie* **2020**, *132* (44), 19662–19670. https://doi.org/10.1002/ange.202004458.

(21) Hovington, P.; Ghaffari-Nik, O.; Mariac, L.; Liu, A.; Henkel, B.; Marx, S. Rapid Cycle Temperature Swing Adsorption Process Using Solid Structured Sorbent for CO_2 Capture from Cement Flue Gas. In *Proceedings of the 15th Greenhouse Gas Control Technologies Conference 15-18 March 2021*; 2021; pp 1–11. https://doi.org/10.2139/ssrn.3814414.

(22) Ho, C.-H.; Paesani, F. Elucidating the Competitive Adsorption of H_2O and CO_2 in CALF-20: New Insights for Enhanced Carbon Capture Metal–Organic Frameworks. *ACS Appl. Mater. Interfaces* **2023**, *15* (41), 48287–48295. https://doi.org/10.1021/acsami.3c11092.

(23) Magnin, Y.; Dirand, E.; Maurin, G.; Llewellyn, P. L. Abnormal CO_2 and H_2O Diffusion in CALF-20(Zn) Metal–Organic Framework: Fundamental Understanding of CO_2 Capture. *ACS Appl. Nano Mater.* **2023**, *6* (21), 19963–19971. https://doi.org/10.1021/acsanm.3c03752.

(24) Chen, Z.; Ho, C.-H.; Wang, X.; Vornholt, S. M.; Rayder, T. M.; Islamoglu, T.; Farha, O. K.; Paesani, F.; Chapman, K. W. Humidity-Responsive Polymorphism in CALF-20: A Resilient MOF Physisorbent for CO_2 Capture. *ACS Mater. Lett.* **2023**, *5* (11), 2942–2947. https://doi.org/10.1021/acsmaterialslett.3c00930.

(25) Blatov, V. A.; Shevchenko, A. P.; Proserpio, D. M. Applied Topological Analysis of Crystal Structures with the Program Package ToposPro. *Cryst. Growth Des.* **2014**, *14* (7), 3576–3586. https://doi.org/10.1021/cg500498k.

(26) Zoubritzky, L.; Coudert, F.-X. CrystalNets.Jl: Identification of Crystal Topologies. *SciPost Chem.* **2022**, *1* (2), 005. https://doi.org/10.21468/SciPostChem.1.2.005.

(27) Rouquerol, J.; Llewellyn, P.; Rouquerol, F. Is the Bet Equation Applicable to Microporous Adsorbents? In *Characterization of Porous Solids VII*; Llewellyn, P. L., Rodriquez-Reinoso, F., Rouqerol, J., Seaton, N. B. T.-S. in S. S. and C., Eds.; Elsevier, 2007; Vol. 160, pp 49–56. https://doi.org/10.1016/S0167-2991(07)80008-5.

(28) Gómez-Gualdrón, D. A.; Moghadam, P. Z.; Hupp, J. T.; Farha, O. K.; Snurr, R. Q. Application of Consistency Criteria To Calculate BET Areas of Micro- And Mesoporous Metal–Organic Frameworks. *J. Am. Chem. Soc.* **2016**, *138* (1), 215–224. https://doi.org/10.1021/jacs.5b10266.

(29) Chung, Y. G.; Gómez-Gualdrón, D. A.; Li, P.; Leperi, K. T.; Deria, P.; Zhang, H.; Vermeulen, N. A.; Stoddart, J. F.; You, F.; Hupp, J. T.; Farha, O. K.; Snurr, R. Q. In Silico Discovery of Metal-Organic Frameworks for Precombustion CO2 Capture Using a Genetic Algorithm. *Sci. Adv.* **2024**, *2* (10), e1600909. https://doi.org/10.1126/sciadv.1600909.

(30) Sturluson, A.; Huynh, M. T.; Kaija, A. R.; Laird, C.; Yoon, S.; Hou, F.; Feng, Z.; Wilmer, C. E.; Colón, Y. J.; Chung, Y. G.; Siderius, D. W.; Simon, C. M. The Role of Molecular Modelling and Simulation in the Discovery and Deployment of Metal-Organic Frameworks for Gas Storage and Separation. *Mol. Simul.* **2019**, *45* (14–15), 1082–1121. https://doi.org/10.1080/08927022.2019.1648809.

(31) Glasby, L. T.; Oktavian, R.; Zhu, K.; Cordiner, J. L.; Cole, J. C.; Moghadam, P. Z. Augmented Reality for Enhanced Visualization of MOF Adsorbents. *J. Chem. Inf. Model.* **2023**, *63* (19), 5950–5955. https://doi.org/10.1021/acs.jcim.3c01190.

(32) Schneemann, A.; Bon, V.; Schwedler, I.; Senkovska, I.; Kaskel, S.; Fischer, R. A. Flexible Metal–Organic Frameworks. *Chem. Soc. Rev.* **2014**, *43* (16), 6062–6096. https://doi.org/10.1039/C4CS00101J.

(33) Kühne, T. D., et al. CP2K: An Electronic Structure and Molecular Dynamics Software Package - Quickstep: Efficient and Accurate Electronic Structure Calculations. *J. Chem. Phys.* **2020**, *152* (19), 194103. https://doi.org/10.1063/5.0007045.

(34) Sarkisov, L.; Bueno-Perez, R.; Sutharson, M.; Fairen-Jimenez, D. Materials Informatics with PoreBlazer v4.0 and the CSD MOF Database. *Chem. Mater.* **2020**, *32* (23), 9849–9867. https://doi.org/10.1021/acs.chemmater.0c03575.

(35) Vanduyfhuys, L.; Rogge, S. M. J.; Wieme, J.; Vandenbrande, S.; Maurin, G.; Waroquier, M.; Van Speybroeck, V. Thermodynamic Insight into Stimuli-Responsive Behaviour of Soft Porous Crystals. *Nat. Commun.* **2018**, *9* (1), 204.

https://doi.org/10.1038/s41467-017-02666-y.

(36) Batzner, S.; Musaelian, A.; Sun, L.; Geiger, M.; Mailoa, J. P.; Kornbluth, M.; Molinari, N.; Smidt, T. E.; Kozinsky, B. E(3)-Equivariant Graph Neural Networks for Data-Efficient and Accurate Interatomic Potentials. *Nat. Commun.* **2022**, *13* (1), 2453. https://doi.org/10.1038/s41467-022-29939-5.

(37) Xu, H.; Stern, H. A.; Berne, B. J. Can Water Polarizability Be Ignored in Hydrogen Bond Kinetics? *J. Phys. Chem. B* **2002**, *106* (8), 2054–2060. https://doi.org/10.1021/jp013426o.

(38) Nazarian, D.; Camp, J. S.; Chung, Y. G.; Snurr, R. Q.; Sholl, D. S. Large-Scale Refinement of Metal−Organic Framework Structures Using Density Functional Theory. *Chem. Mater.* **2017**, *29* (6), 2521–2528. https://doi.org/10.1021/acs.chemmater.6b04226.

(39) Vandenhaute, S.; Cools-Ceuppens, M.; DeKeyser, S.; Verstraelen, T.; Van Speybroeck, V. Machine Learning Potentials for Metal-Organic Frameworks Using an Incremental Learning Approach. *npj Comput. Mater.* **2023**, *9* (1), 19. https://doi.org/10.1038/s41524-023-00969-x.

(40) Dubbeldam, D.; Calero, S.; Ellis, D. E.; Snurr, R. Q. RASPA: Molecular Simulation Software for Adsorption and Diffusion in Flexible Nanoporous Materials. *Mol. Simul.* **2016**, *42* (2), 81–101. https://doi.org/10.1080/08927022.2015.1010082.

(41) Mayo, S. L.; Olafson, B. D.; Goddard, W. A. DREIDING: A Generic Force Field for Molecular Simulations. *J. Phys. Chem.* **1990**, *94* (26), 8897–8909. https://doi.org/10.1021/j100389a010.

(42) Campañá, C.; Mussard, B.; Woo, T. K. Electrostatic Potential Derived Atomic Charges for Periodic Systems Using a Modified Error Functional. *J. Chem. Theory Comput.* **2009**, *5* (10), 2866–2878. https://doi.org/10.1021/ct9003405.

(43) Potoff, J. J.; Siepmann, J. I. Vapor–Liquid Equilibria of Mixtures Containing Alkanes, Carbon Dioxide, and Nitrogen. *AIChE J.* **2001**, *47* (7), 1676–1682. https://doi.org/10.1002/aic.690470719.

(44) Vega, C.; Abascal, J. L. F.; Nezbeda, I. Vapor-Liquid Equilibria from the Triple Point up to the Critical Point for the New Generation of TIP4P-like Models: TIP4P/Ew, TIP4P/2005, and TIP4P/Ice. *J. Chem. Phys.* **2006**, *125* (3), 34503. https://doi.org/10.1063/1.2215612.

(45) Tribello, G. A.; Bonomi, M.; Branduardi, D.; Camilloni, C.; Bussi, G. PLUMED 2: New

Feathers for an Old Bird. *Comput. Phys. Commun.* **2014**, *185* (2), 604–613. https://doi.org/https://doi.org/10.1016/j.cpc.2013.09.018.

(46) Bonomi, M., et al. Promoting Transparency and Reproducibility in Enhanced Molecular Simulations. *Nat. Methods* **2019**, *16* (8), 670–673. https://doi.org/10.1038/s41592-019-0506-8.

(47) Grossfield, A. WHAM: the weighted histogram analysis method, version 2.0.10 http://membrane.urmc.rochester.edu/wordpress/?page_id=126.

Chapter 4

Supplementary Information Document

S.4.1. Supplementary Methods 1

Powder X-ray Diffraction (PXRD) measurements

PXRD patterns were collected using a Rigaku Miniflex 600 bench top PXRD equipped with a CuK_α x-ray source. The samples were prepared by soaking the powders in a solvent (ethanol or water) for 1 hour and then drop casted onto a standard sample holder. The PXRD pattern was collected while the powder was still wet. For the samples run under N_2, the powder was loaded onto a BTS 500 high temperature sample holder and heated to 110°C for 45 minutes under constant N_2 flow. Then the powder was allowed to cool to 50°C and equilibrated at this temperature for 10 minutes. The PXRD pattern was then collected at 50°C. The samples run under CO_2 were dried under N_2 and then during the PXRD collection, 100% CO_2 was flowed through under the same conditions described above. The PXRD patterns under different relative humidities (%RH) were collected by flowing wet gas through the BTS 500 chamber. The humidity of wet gas was controlled using gas bubbler and monitored with a RH probe.

Gas adsorption measurements

Nitrogen and CO_2 isotherms were measured using ASAP2020 from Micromeritics Instruments Inc. Before gas adsorption, the samples were heated under vacuum at 140 °C for 5 hours. The water isotherm was measured using a gravimetric vapor sorption analyzer (DVS Resolution, Surface measurement system). Samples were activated under dry nitrogen flow at 140 °C for 2 hours. Dm/dt value of 0.0005%/min was used as the equilibrium criteria for each data point.

S.4.2. Supplementary Figures

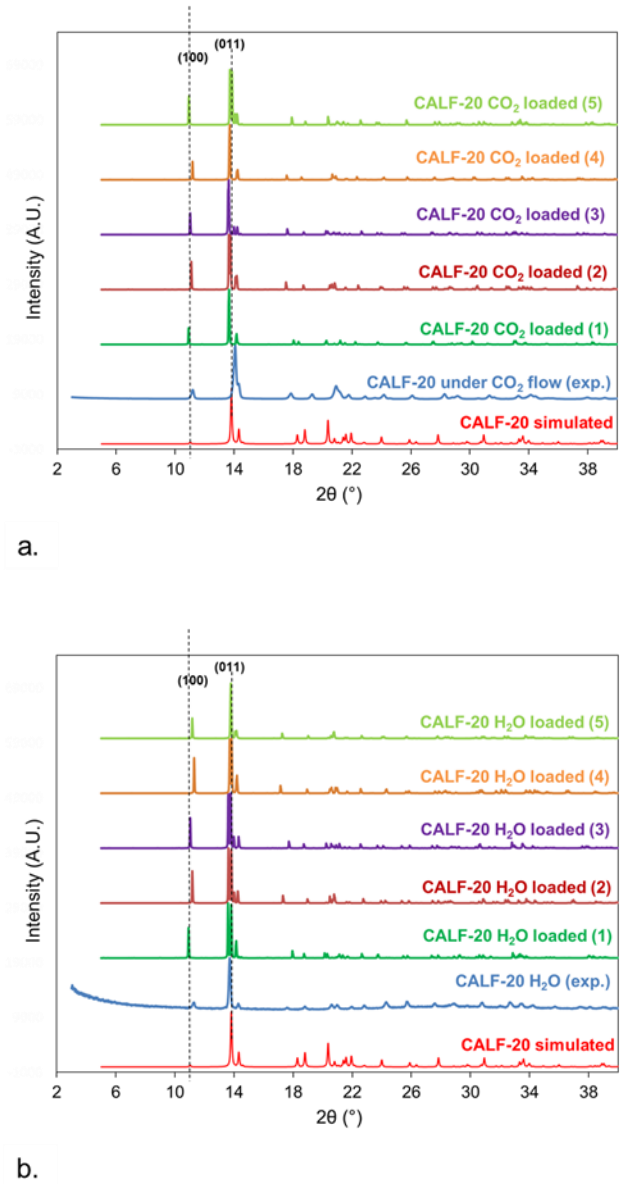

Figure S.4.1. The powder X-ray diffraction (PXRD) patterns for ***a.*** *CO_2-induced CALF-20 and* ***b.*** *water-induced CALF-20 obtained from different configuration of NPT simulations. The simulated PXRDs are compared with experimental PXRDs in the presence CO_2 and soaked in water.*

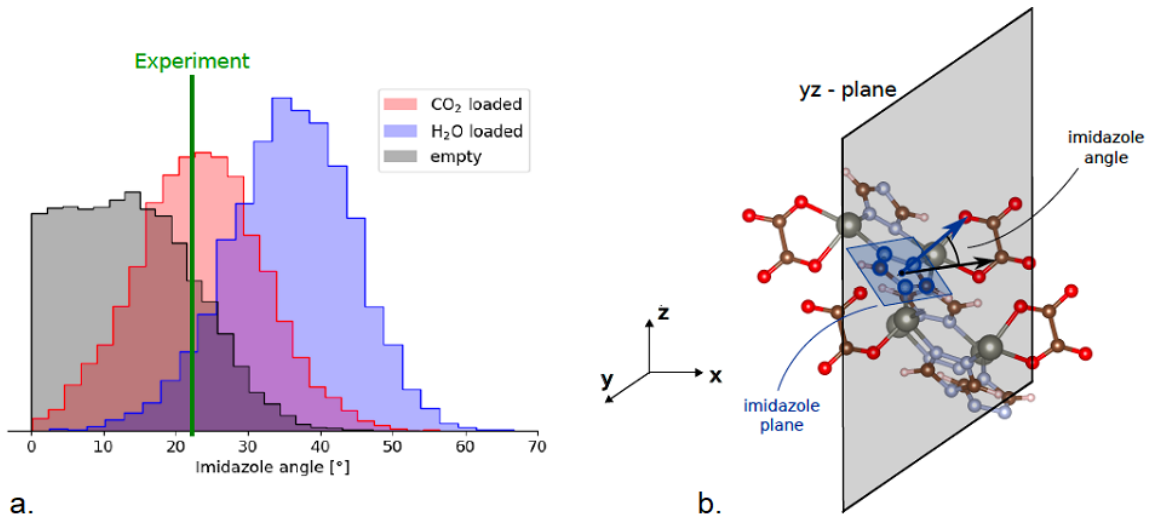

Figure S.4.2 ***a.*** *Histograms showing the rotation of the traizolate linkers in the experimental, empty, CO_2-loaded and H_2O-loaded CALF-20 structures. The angle distributions are obtained from the free energy profiles at saturation loadings and 273 K.* ***b.*** *Schematic showing the angle between the normal on the plane defined by the triazolate linker and the YZ-plane calculated in* ***a.***

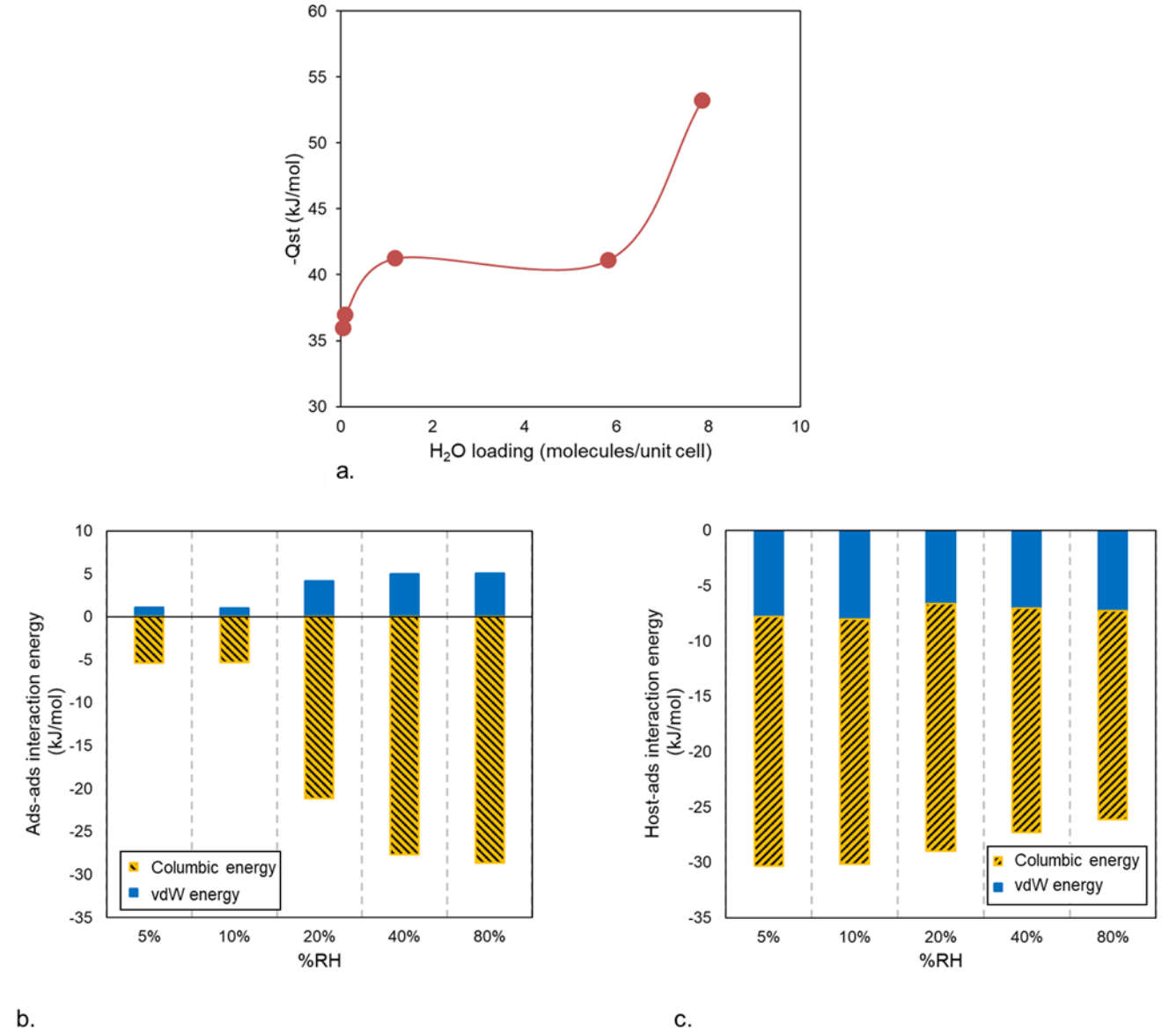

Figure S.4.3. ***a****. Heat of adsorption versus water loading in molecules per unit cells of CALF-20 at 293 K. Breakdown of van der Waals and Columbic interaction energy for* ***b.*** *water-water and* ***c.*** *water-framework at different relative humidities (%RH).*

S.4.4. Supplementary Methods 2

Gas adsorption isotherms in CALF-20 were calculated via grand canonical Monte Carlo (GCMC) simulations using the RASPA simulation software.[1] The Lennard-Jones (LJ) parameters for adsorbent atoms are tabulated in Table S1. N_2 and CO_2 molecules were modelled using the TraPPE[2] force field with charges placed on each atom and at the centre of mass. Water molecule was modelled using the TIP4P force field.[3] Table S2-S4 tabulates all of the LJ parameters and atomic charges for all gas molecules.

Table S.4.1. LJ parameters for CALF-20

Atom type	σ (Å)	ε/k_B (K)	Force field
C	3.473	47.859	Dreiding[4]
O	3.033	48.160	Dreiding[4]
H	2.846	7.649	Dreiding[4]
N	3.263	38.951	Dreiding[4]
Zn	4.045	27.677	Dreiding[4]

Table S.4.2. LJ parameters and charges for N_2

Atom type	σ (Å)	ε/k_B (K)	Atomic charge	Force field
N_N_2	3.31	36.0	-0.482	TraPPE[2]
N_center of mass	0	0	0.964	TraPPE[2]
N_N_2	3.31	36.0	-0.482	TraPPE[2]

Table S.4.3. LJ parameters and charges for CO_2

Atom type	σ (Å)	ε/k_B (K)	Atomic charge	Force field
C_CO_2	2.80	27.0	0.70	TraPPE[2]
O_CO_2	3.05	79.0	-0.35	TraPPE[2]

Table S.4.4. LJ parameters and charges for water

Atom type	σ (Å)	ε/k_B (K)	Atomic charge	Force field
O_H_2O	3.154	78.0	0	Tip4P[3]
H_H_2O	0	0	0.52	Tip4P[3]
M_H_2O	0	0	-1.04	Tip4P[3]

References

(1) Dubbeldam, D.; Calero, S.; Ellis, D. E.; Snurr, R. Q. RASPA: Molecular Simulation Software for Adsorption and Diffusion in Flexible Nanoporous Materials. *Mol. Simul.* **2016**, *42* (2), 81–101. https://doi.org/10.1080/08927022.2015.1010082.

(2) Potoff, J. J.; Siepmann, J. I. Vapor–Liquid Equilibria of Mixtures Containing Alkanes, Carbon Dioxide, and Nitrogen. *AIChE J.* **2001**, *47* (7), 1676–1682. https://doi.org/10.1002/aic.690470719.

(3) Vega, C.; Abascal, J. L. F.; Nezbeda, I. Vapor-Liquid Equilibria from the Triple Point up to the Critical Point for the New Generation of TIP4P-like Models: TIP4P/Ew, TIP4P/2005, and TIP4P/Ice. *J. Chem. Phys.* **2006**, *125* (3), 34503. https://doi.org/10.1063/1.2215612.

(4) Mayo, S. L.; Olafson, B. D.; Goddard, W. A. DREIDING: A Generic Force Field for Molecular Simulations. *J. Phys. Chem.* **1990**, *94* (26), 8897–8909. https://doi.org/10.1021/j100389a010.

5. High Throughput Screening of MOFs for CO_2 capture in the presence of humidity

Abstract

Metal-organic frameworks (MOFs), one of the most exciting developments in recent porous materials science, are now, more than ever, in the center of attention as they make their way successfully into industrial applications for gas storage and separation applications such as CO_2 capture from flue gas. Most gas adsorption/separation applications are inevitably operated under humid conditions where most MOFs suffer from the competitive adsorption of water which leads to adverse effects on their ability to adsorb CO_2. Therefore, considering the co-adsorption of water in the designing design new MOFs to capture CO_2 from flue gas is essential. Here, using a multi-scale computational strategy that includes density functional theory (DFT) and grand canonical Monte Carlo (GCMC) simulations, we developed a systematic high-throughput computational screening to explore The Quantum MOF (QMOF) database and the Computation-Ready, Experimental (CoRE) MOF database for selective adsorption of CO_2 from a wet flue gas mixture. After the first-stage screening based on geometric properties of MOFs, a total of ca. 10,000 porous MOFs were considered for large-scale simulations of CO_2 and H_2O adsorption. The next stage of the simulations was focused on pure component CO_2 and H_2O, as well as the binary CO_2-water simulations. The screening strategy successfully identified a number of promising MOFs that are selective towards CO_2 in the presence of water vapour. Through a tight feedback loop between simulations, and experiments performed by our industrial collaborator, a number of MOFs were successfully synthesized and tested in the lab demonstrating the validity of our approach in identifying outstanding MOFs for CO_2 capture.

Chapter 5

5.1. Introduction

The utilisation of robust adsorbents present a compelling and energy-efficient alternative for strategies pertaining to carbon capture and storage (CCS). Nevertheless, some adsorbents may suffer from the competitive adsorption of other gas molecules present in flue gas.[1–4] Hence, the identification of an appropriate adsorbent material that exhibits superior performance in selectively adsorbing CO_2 in the presence of other gas molecules, including nitrogen and water remains the key challenge. Metal-organic frameworks (MOFs) have emerged as a significant advancement in the field of porous materials science. Currently, given the continue increase in the number of MOFs synthesis to date reaching about 100,000 structures,[5,6] they are garnering considerable attention due to being an ideal platform and their successful implementation into industrial-scale adsorption process.[7–9] Notably, they have demonstrated efficacy in capturing CO_2 from flue gas, further highlighting their potential in this domain. CALF-20, low-price and scalable Zn-based MOFs synthesized by Shimizu et al, proved its best practice MOFs in post-combustion CO_2 capture in cement production by capturing 1 tonne of CO_2.[10–12] The hydrophobicity nature of CALF-20 makes it as one of the only top candidates for this application.

However, the precise mechanisms underlying the development of hydrophobic behaviour in materials are not yet fully comprehended, although recent advancements have shed light on the connections between molecular properties and the hydrophobic nature of MOFs.[13–15] Hence, the exploration on MOFs characterized by minimal or negligible water adsorption, commonly referred to as hydrophobic MOFs, hold potential as viable options for carbon capture applications. A number of recent studies in the field of high-throughput screening (HTS) have examined the presence of water vapour in conjunction with carbon dioxide (CO_2) and nitrogen (N_2). Li et al.[16] conducted a screening of 5109 CoRE MOFs to evaluate their potential for CO_2 capture from wet flue gas mixtures. The selectivity for CO_2/H_2O was determined by comparing the calculated Henry's law constants (K_H) for CO_2 and H_2O. Based on the findings of this study, it has been determined that a reduced pore size exhibits enhanced affinity for CO_2 molecules, thereby restricting the adsorption of water under conditions of elevated humidity. This is primarily attributed to the prevention of water cluster formation within the confined pore structure. In a separate and intriguing investigation, Boyd et al.[1] documented the empirical identification of MOFs for the purpose of capturing CO_2 from a moist flue gas mixture. In this study, a library consisting of 325,000 computationally generated MOFs was subjected to screening. MOFs featuring parallel aromatic rings at a distance of

approximately 7 Å have been suggested as promising materials for the capture of CO_2 in the presence of water vapour. While HTS can suggest new materials for certain application, but the actual process is still complicated due to the challenge of proposing MOFs that are hard to synthesize in a lab setting.[17] This technique has so far failed to accurately predict the most empirically relevant features of stability (e.g activation and thermal stability).[18] Thus, the quantity of best-performance MOFs identified by computer-based methods remains rather scarce.

There exists a motivation to evaluate and establish a standard for materials in the domain of CO_2 sorbents in the presence of water for practical implementation. It is customary to assess several industrial represented key evaluation metrics[19] and integrating process knowledge into the screening framework[20] including materials stability in which it has been challenging to predict. Initial efforts have been made in this direction, such as comparing the stability of various MOFs using their calculated free energies.[21] Therefore, integrating the predicted stability of MOFs[22,23] into the screening protocol shows great promise. Here, we developed a systematic and efficient computational screening method to investigate the selective adsorption of CO_2 from a wet flue gas mixture using the Quantum MOF (QMOF) database[24] and the Computation-Ready, Experimental (CoRE) MOF database.[25] The screening methodology effectively discovered several interesting MOFs that exhibit selectivity towards CO_2 in the presence of water vapor involving the key process parameters. Though some top-performing MOFs were identified through this protocol, yet in real condition these structures failed to perform in industrial settings. Interestingly, we successfully identified several top-performing MOFs out of ~20,000 published experimental structures by establishing a rigorous feedback loop encompassing screening process and experimental testing conducted in collaboration our industrial partner. The screening process was evaluated according to the operating condition set by the industrial partner in which few studies could provide. Those top-performing structures should be further evaluated to comply with this application for their (1) materials synthesizability, (2) high CO_2 capture capacity and selectivity towards water, and (3) mechanical, thermal and chemical stability. It is worth-noting to introduce other industrial-related parameters in computational screening protocols for identifying top-performance materials in particular applications.

5.2. Results and Discussion

5.2.1. High-Throughput Computational Screening of ~23,000 MOFs

For the selection of MOFs search space, we explored a newly developed MOF database in the literature: QMOF database,[24] a publicly-available database of computed quantum-chemical properties for more than ca. 20,000 experimentally-synthesized MOFs. The geometry of these structures are relaxed using DFT calculations and partial atomic charges are computed using the Density Derived Electrostatic and Chemical (DDEC) method. In addition, we also explored 2,932 MOFs in the CoRE MOF database[25] where the partial atomic charges for all MOFs were also calculated using the DDEC method. The initial screening was conducted with respect to structures having Pore Limiting Diameter (PLD) values of > 2.0 Å, to take into account materials even with ultramicropores, and consider potential structural flexibility in certain materials: we note that the kinetic diameter of CO_2 is ca. 3.3 Å. This criterion in initial screening allowed for pre-selection of ~7,800 structures (out of ~20,000 structures) from the QMOF database. This subset was then complemented with 2,932 MOFs from the CoRE/DDEC MOF database for further simulations. For the total of ca. 10,732 structures, we first calculated the Henry's constant (K_H) at 323 K through the Widom insertion method.[27] CO_2 and H_2O K_H calculations indicate the affinity of MOFs towards each adsorbate at low-pressure regimes and can be used as a useful metric to identify CO_2-selective materials and eliminate hydrophilic structures to avoid competitive adsorption of water. After the K_H screening, we calculated the amount of CO_2 adsorbed in all 10,732 MOFs at 323 K and 114 mmHg. At the request of industrial collaborator, we later calculated the CO_2 uptake at 30.4 mmHg for the entire database. The temperature and pressure set for screening calculations are according to the industrial-relevant operating condition set by the input from our industrial collaborator.

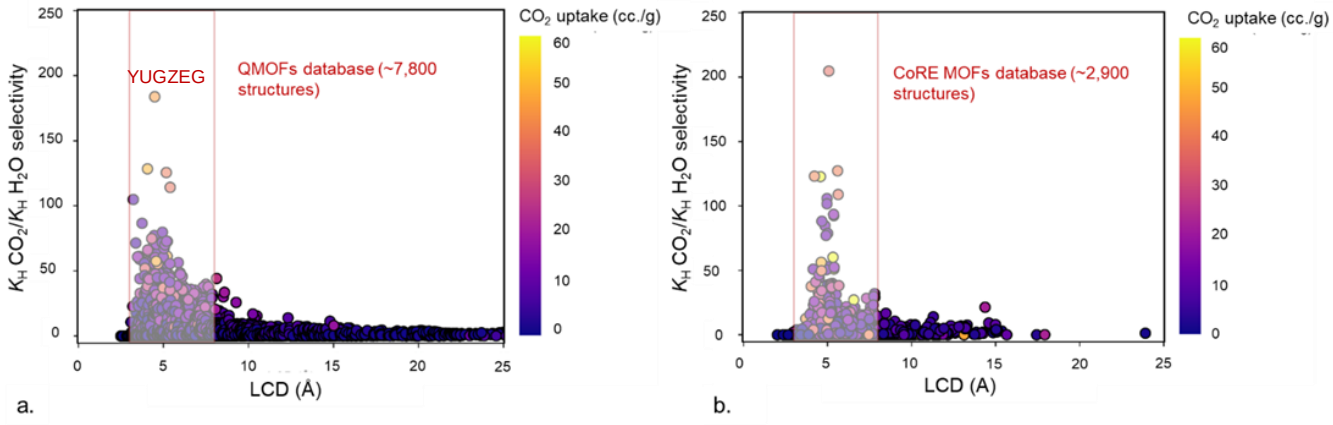

*Figure 5.1. CO_2/H_2O K_H selectivity vs. the largest cavity diameter (LCD) for **a.** the QMOF database and **b.** MOFs present in the CoRE/DDEC database. The color bar represents the amount of CO_2 adsorbed at 114 mmHg and 323 K.*

Figure 5.1 presents the structure-property relationships for all screened MOFs (a. QMOF and b. CoRE/DDEC). They y-axis shows the CO_2/H_2O selectivity as a function of LCD and how it relates to the CO_2 adsorption capacity via the color bar representation. The CO_2/H_2O selectivity was calculated from the ratio of CO_2 and H_2O Henry's constant at 323 K. It is shown that the structures containing cavities between 4–7 Å, in both the QMOF and the CoRE/DDEC databases, have high CO_2 capacity of > ca. 20 cc/g and CO_2/H_2O selectivity of > 10 due to tighter fit of CO_2 inside the pores. However, for MOFs with larger pores i.e. those with LCD > 7 Å, the selectivity and the amount of CO_2 adsorbed decreases dramatically due to lower interactions with the framework walls. One notable MOFs from this screening is (CSD REFOCDE: YUGZEG)[27], a copper-based MOFs with 2,3-pyrazinedithiol linker, which shows high CO_2/H_2O selectivity of 183 and relatively high CO_2 uptake of c.a 45 cc/g.

To identify promising materials, we looked into structures with CO_2 uptake higher than 22.4 cc/g, and 11 cc/g at 114 mmHg and 30.4 mmHg, respectively. These values correspond to the CO_2 uptake in activated carbons at the similar operating conditions. We also eliminated materials with CO_2/H_2O selectivity less than unity at this stage of the screening, as this indicates preferential adsorption of water over CO_2. We also highlight structures whose water K_H values are lower than that of CALF-20 (K_H H_2O in CALF-20: 5.6 X 10^{-5} mol/kg.Pa) to eliminate more hydrophilic materials. We have previously shown that low affinity towards water at low loadings indicate hydrophobic behavior resulting in a type V (S-shaped) water adsorption isotherm. This means that these structures should not adsorb water at lower relative humidity values. The above criteria allowed further reduction of the total number of promising MOFs to ca. 200 MOFs in the QMOF and ca. 100 MOFs in the CoRE/DDEC MOF database.

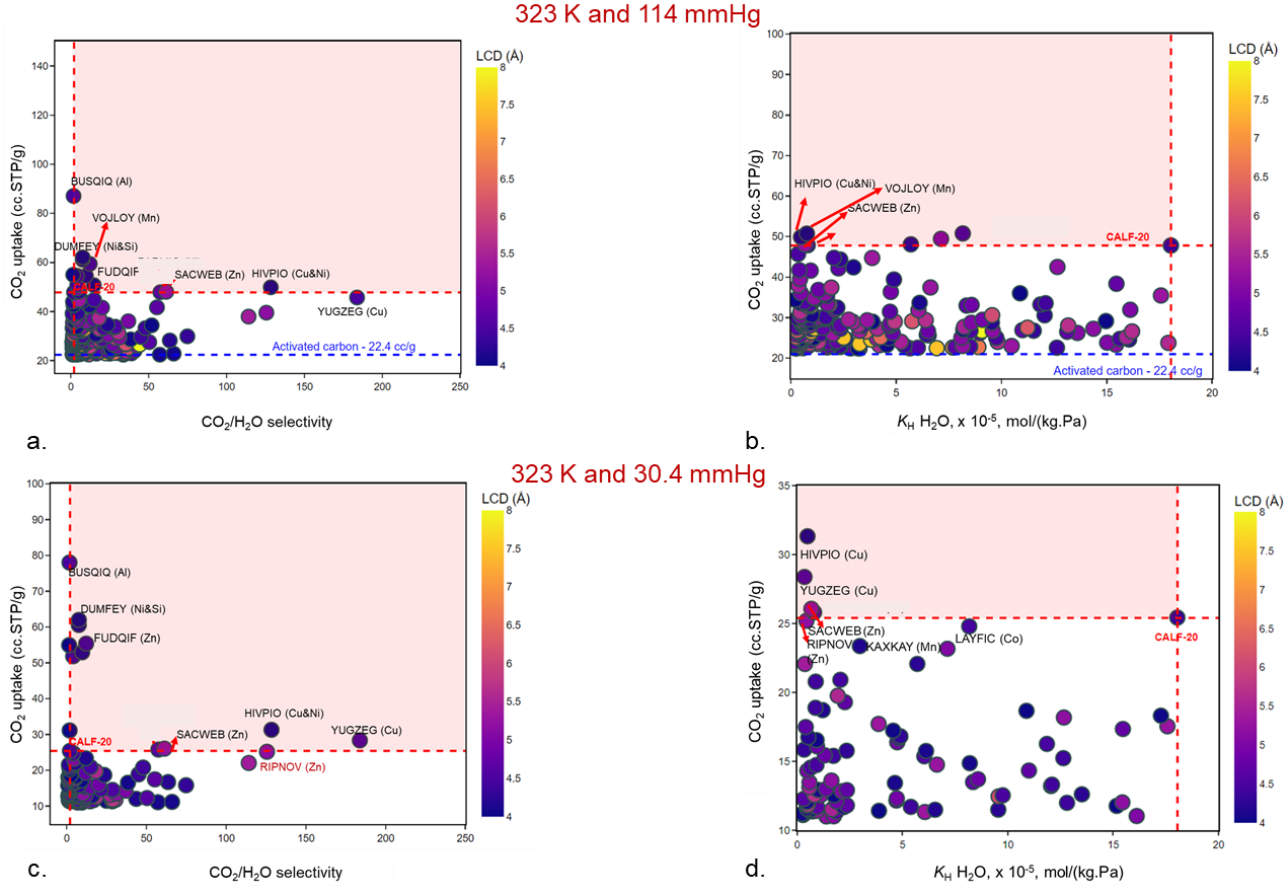

Figure 5.2. ***a.*** *CO_2 uptake vs. CO_2/H_2O selectivity for ~200 MOFs in the QMOF database at 323 K and 114 mmHg;* ***b.*** *CO_2 uptake vs. water K_H for hydrophobic MOFs at 323 K and 114 mmHg;* ***c.*** *CO_2 uptake vs. CO_2/H_2O selectivity at 323 K and 30.4 mmHg; and* ***d.*** *CO_2 uptake vs. water K_H for hydrophobic MOFs at 323 K and 30.4 mmHg. The color bar represents the largest cavity diameter (LCD).*

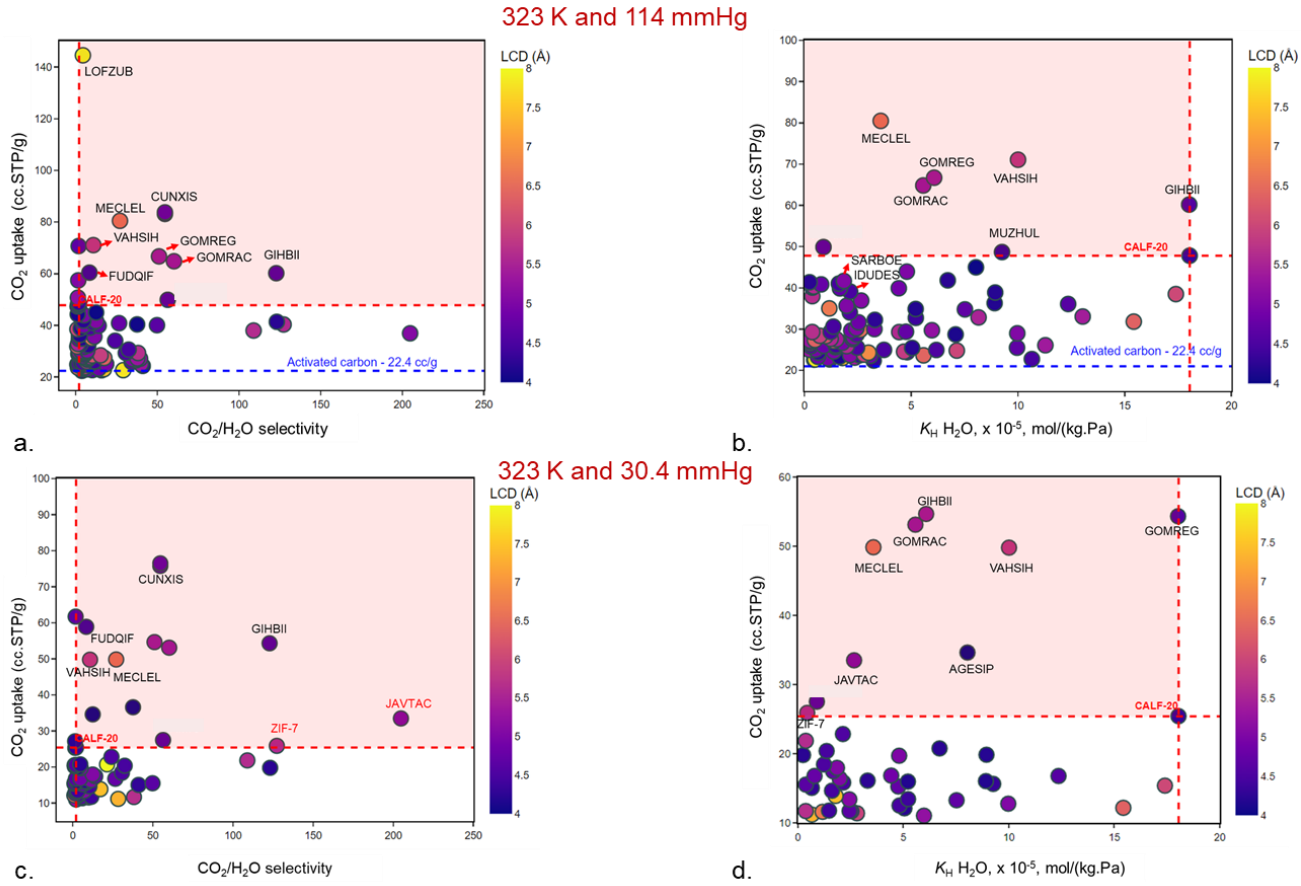

Figure 5.3. ***a.*** *CO_2 uptake vs CO_2/H_2O selectivity for ~100 MOFs in the CoRE/DDEC MOF database at 323 K and 114 mmHg;* ***b.*** *CO_2 uptake vs water K_H water at 323 K and 114 mmHg;* ***c.*** *CO_2 uptake vs CO_2/H_2O selectivity at 323 K and 30.4 mmHg; and* ***d.*** *CO_2 uptake vs K_H water at 323 K and 30.4 mmHg. The color bar represents the largest cavity diameter (LCD).*

Figures 5.2-5.3 show a wide range of structure-property relationships corresponding to the CO_2 uptake vs CO_2/H_2O selectivity and their hydrophobicity indicated by the water K_H at 323 K; and two different pressure points of 114 mmHg and 30.4 mmHg. The color in the data points shows the largest cavity diameter (LCD) of the structures. Here, we show that most materials with small pore size (< 6 Å) tend to have high CO_2 uptake of > 30 cc/g and high selectivity vs. water. Interestingly, out of all the structures screened for both databases, only a handful exhibit CO_2 uptakes larger than that of CALF-20 (Figure 2a and 2b, Figure 3a and 3b). The CCDC refcodes for these structures are: SACWEB,[28] HIVPIO,[29] BUSQIQ,[30] FUDQIF,[31] and YUGZEG[27] identified from both MOF databases.

5.2.2. CO_2, Water and Binary Adsorption Isotherms for the Top MOF Candidates

CO_2 adsorption isotherms calculated for the top candidates:

Figure 5.4 presents simulated CO_2 adsorption isotherms for the top candidates identified and compares them with isotherm obtained from CALF-20 at 323 K. At low pressures of < 200

mmHg, SACWEB has rather similar CO_2 uptake when compared with CALF-20. At the same pressure range, BUSQIQ and FUDQIF present higher uptakes of 60 cc/g and 80 cc/g, respectively, reaching their saturation loading at low pressures.

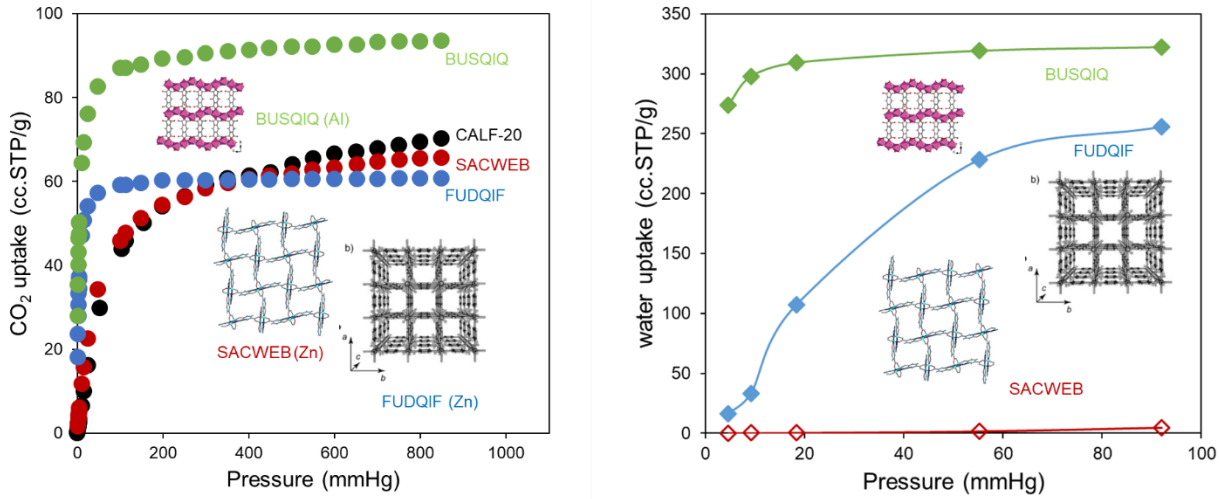

Figure 5.4. ***a****. Simulated CO2 adsorption isotherms for the top MOF candidates identified through computational screening. The simulations are carried out at 323 K and compared with the benchmark material, CALF-20.* ***b****. Simulated volumetric H2O adsorption isotherms at 323 K; close and open symbol represent hydrophilic and hydrophobic MOFs, respectively.*

Table 1 lists other MOFs that were considered for further simulations given their high CO_2 uptake at both 4% and 15% of P_{CO2} while exhibiting low water affinity. We note that most of these structures possess similar range of pore sizes when compared to CALF-20. A longer list of structures ranked according to their CO_2 adsorption performance were also shared with our collaborator scientists for further synthesis and testing in the laboratory.

Table 5.1. List of all the top-performing MOFs considered for CO_2, water and binary adsorption isotherms calculations.

QMOF ID	CCDC refcode	K_H CO_2 ($x10^{-4}$) mol/(kg.Pa)	K_H H_2O ($x10^{-4}$) mol/(kg.Pa)	K_H CO_2 / K_H H_2O selectivity	CO_2 uptake (cc.STP/g) at 30.4 mmHg	CO_2 uptake (cc.STP/g) at 114 mmHg	LCD (Å)	PLD (Å)	Metal
qmof-9af4bae	BUSQIQ	135.58	75.39	1.80	78.02	87.07	4.46	3.90	Al
qmof-3b672a9	FUDQIF	64.66	5.29	12.23	55.38	59.42	4.37	3.82	Zn
qmof-ee435a5	HIVPIO	6.24	0.05	128.45	31.33	49.88	4.06	3.64	Cu
qmof-6f21ecc	SACWEB	4.10	0.07	61.30	26.06	48.03	5.21	2.20	Zn
qmof-03a39a4	YUGZEG	6.29	0.34	183.84	28.37	45.72	4.49	3.54	Cu
CALF-20	TASYAR	2.74	0.57	4.84	25.43	47.80	4.34	2.85	Zn

Following our molecular simulation and high-throughput screening results, the industrial collaborator recommends some of potential structures for further analysis. This selection is based on the availability of metal precursor and organic linker as well as their synthesizability factor set by our industrial collaborator. **Figure 5.5** compares CO_2 adsorption isotherms for a few other top MOFs and compares them with that of CALF-20 at 323 K. The structures are: FUWXOL, EMIVAY, YUGZEG, HIVPIO, ABAVIJ, and XEQLEM. We note that these structures show comparable or even higher CO_2 uptakes than CALF-20 at pressures below 200 mmHg with capacities up to ~30 cc/g at 323 K and 114 mmHg. DAYCEN, GULPIN, ABAVIJ, and XEQLEM exhibit substantially lower saturation loading than CALF-20 with the uptake of lower than 60 cc/g (**Figure 5.5c**).

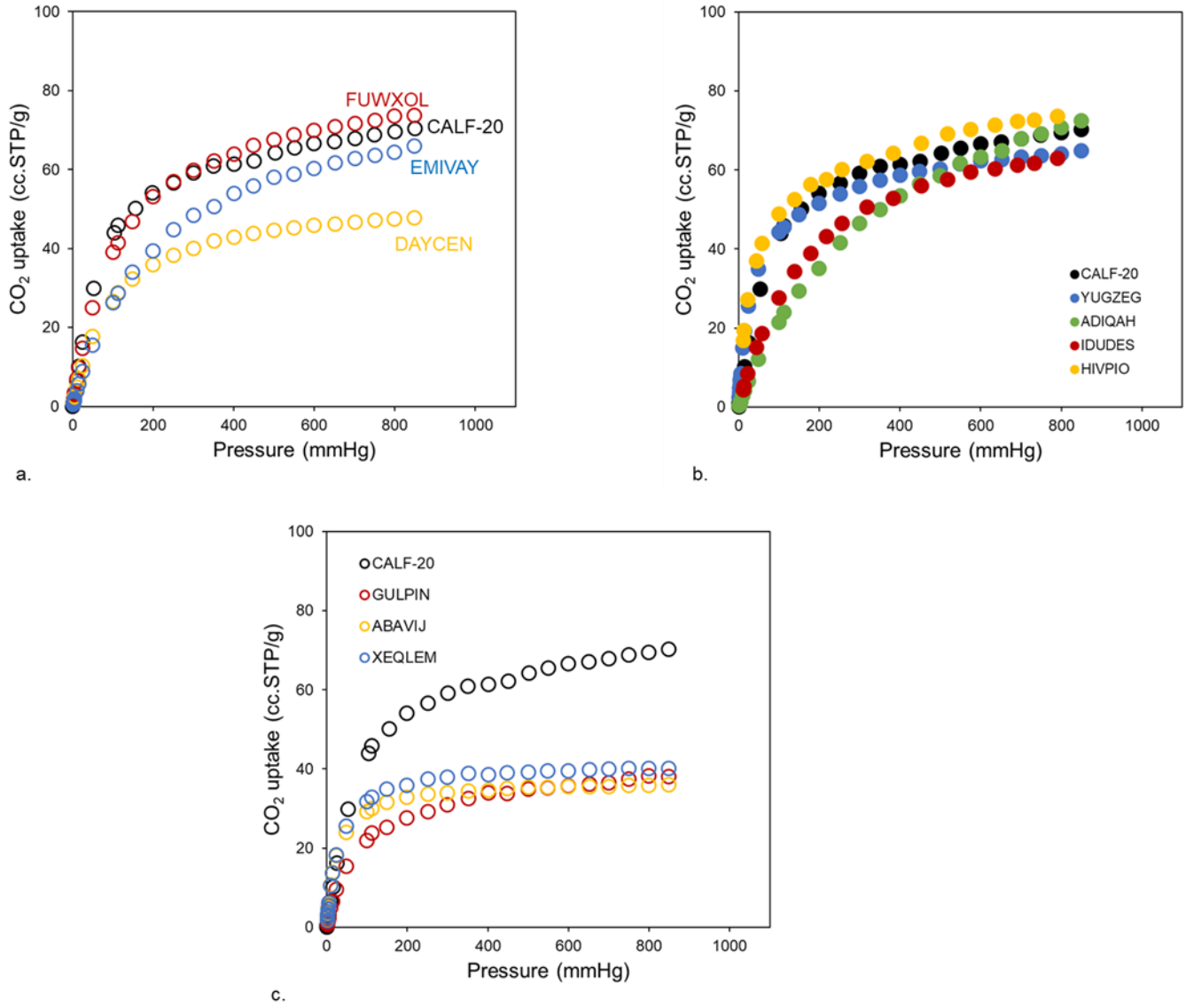

Figure 5.5. Simulated CO_2 adsorption isotherms for selected MOF candidates at 323 K.

H_2O adsorption isotherms calculated for the top candidates:

Production of full adsorption isotherms for water is important as we can determine the exact pressure where the condensation occurs and the pores start to get filled with water. We note here that the shape of the water isotherms is important in determining water affinity of MOFs: type I isotherms are often observed for hydrophilic MOFs and type V for those exhibiting hydrophobic behavior. **Figure 5.6.a** and 5.**6.b** compares water adsorption isotherms for a number of hydrophilic and hydrophobic MOFs, respectively at 323 K and pressure ranges of 0 – 800 mmHg. As shown in **Figure 5.6.a**, 5 out of 14 top MOF candidates can be categorized as hydrophilic indicated from the shape of water isotherms and the amount of water adsorbed at low pressure. For example, it can be clearly seen that BUSQIQ and FUDQIF are hydrophilic as they adsorb substantial amount of water at low pressure ranges (< 60 mmHg). The inflection point for GULPIN, KOMGUP, and DAYCEN occurs at higher pressures when they start to adsorb water. We anticipate high levels of competitive water adsorption for these structures which makes them non-ideal for CO_2 capture in humid conditions. On the other hand, **Figure 6b** shows nine MOFs exhibiting strong hydrophobicity indicated by relatively low amount of water adsorbed for the entire pressure range studied. Some of these structures were recommended to the industrial collaborator for further laboratory synthesis and testing.

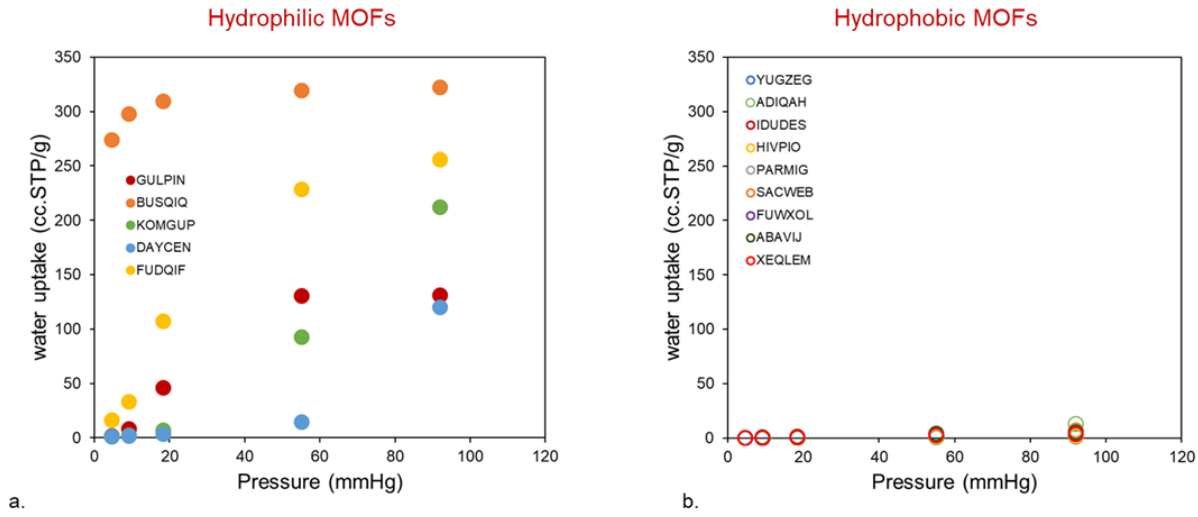

*Figure 5.6. Simulated H_2O adsorption isotherms **a**. hydrophilic and **b**. hydrophobic MOFs at 323 K.*

Binary CO_2/H_2O adsorption isotherms calculated for the top candidates:

The binary CO_2-water adsorption isotherms are shown in **Figure 5.7.a** for hydrophilic MOFs and **Figure 5.7.b** for those that are hydrophobic. As expected, for the hydrophilic structures, we see a reduction in CO_2 adsorption capacity with the increase of relative humidity of > 10%.

This means that there is a competition adsorption between CO_2 and water for the same adsorption sites they prefer to interact stronger with water molecules. Moreover, at high %RH, these structures have lost almost all of their CO_2 capacity. **Figure 5.7.b** compares the binary CO_2-water adsorption isotherms for the hydrophobic MOFs. It can be clearly seen that the CO_2 uptake in these structures is hardly affected by the vapor presence. In other words, water has negligible effect on the CO_2 uptake in those structures.

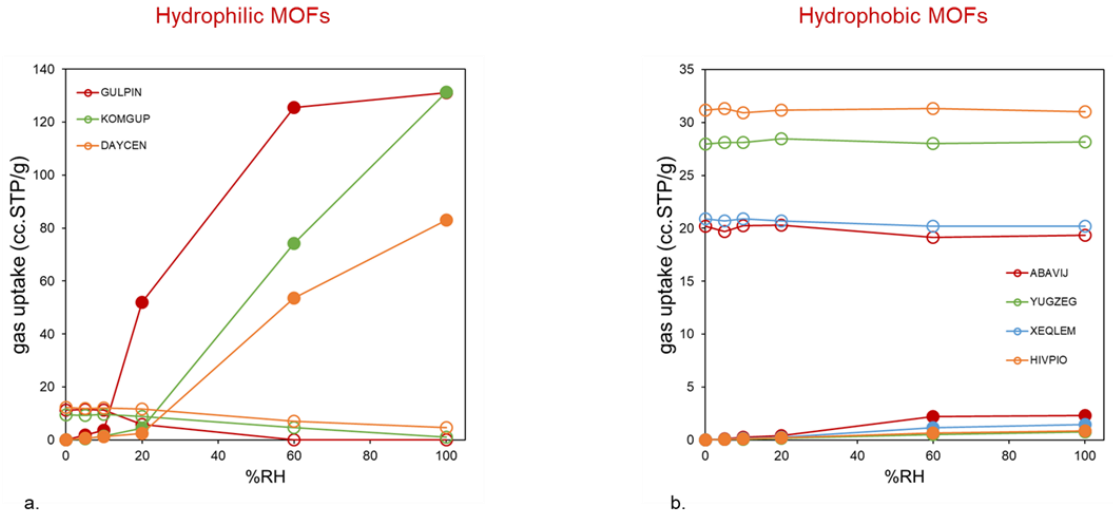

*Figure 5.7. Simulated CO_2-H_2O binary adsorption isotherms **a.** hydrophilic and **b.** hydrophobic MOFs at 323 K and different relative humidities (%RH). The partial pressure of CO_2 is fixed at 4% for all MOFs.*

5.2.3. Study on CO_2, Water and Binary Adsorption Isotherms for Fluorinated-Functionalized MOFs

There are a few reports in the literature where flourinated compounds have performed well for CO_2 adsorption in the presence of high humidity levels.[32] Another class of fluorinated MOFs is the anionic structures such as SIFSIX-3-Ni[33] and KAUST-7,[34] have been gaining a lot of interest. In SIFSIX-3-Ni, $(SiF_6)^{2-}$ anions coordinate divalent metal cations of Ni while in KAUST-7 each Ni^{2+} cation is coordinated to two $(NbOF_5)^{2-}$ polyatomic anions and four pyrazine molecules to form a primitive tetragonal lattice with ***pcu*** topology.[35] Motivated by the already-published performance of these structures, we investigated their performance in capturing CO_2. Using the same computational protocols employed in the previous sections, we performed pure component CO_2 and water adsorption isotherms along with binary CO_2-water mixture isotherms for SIFSIX-3-Ni and KAUST-7 (**Figure 5.8**). It is shown that both materials adsorb high amounts of CO_2 at low pressure regime of < 100 mmHg with capacities of ca. 55 cc/g and 60 cc/g calculated for SIFSIX-3-Ni and KAUST-7, respectively. Due to their ultramicroporous nature, both structures are saturated with CO_2 at ca. 100 mmHg. This means that both structures, surpass the CO_2 capacity of CALF-20 at the Henry's regime (**Figure 5.8a**).

Looking at water adsorption isotherms shown in **Figure 5.8b**, both structures adsorb high amounts of water at even low pressure of 20 mmHg indicating their high affinity with water molecules. When water vapor was introduced in CO_2 binary mixture calculations, we observe that in SIFSIX-3-Ni, the CO_2 uptake is first reduced at 20%RH, where water adsorption isotherms showed the inflection point. KAUST-7, the more hydrophilic structure, exhibits even more drastic change in its CO_2 uptake even at low %RH and loses almost all of its CO_2 capacity at 60% RH. This means that although the CO_2 uptake at 4% is very high at *ca.* 60 cc/g for SIFSIX-3-Ni co-adsorption of water in the presence of CO_2 can be detrimental to their performance, a prediction that was also verified by experiments.

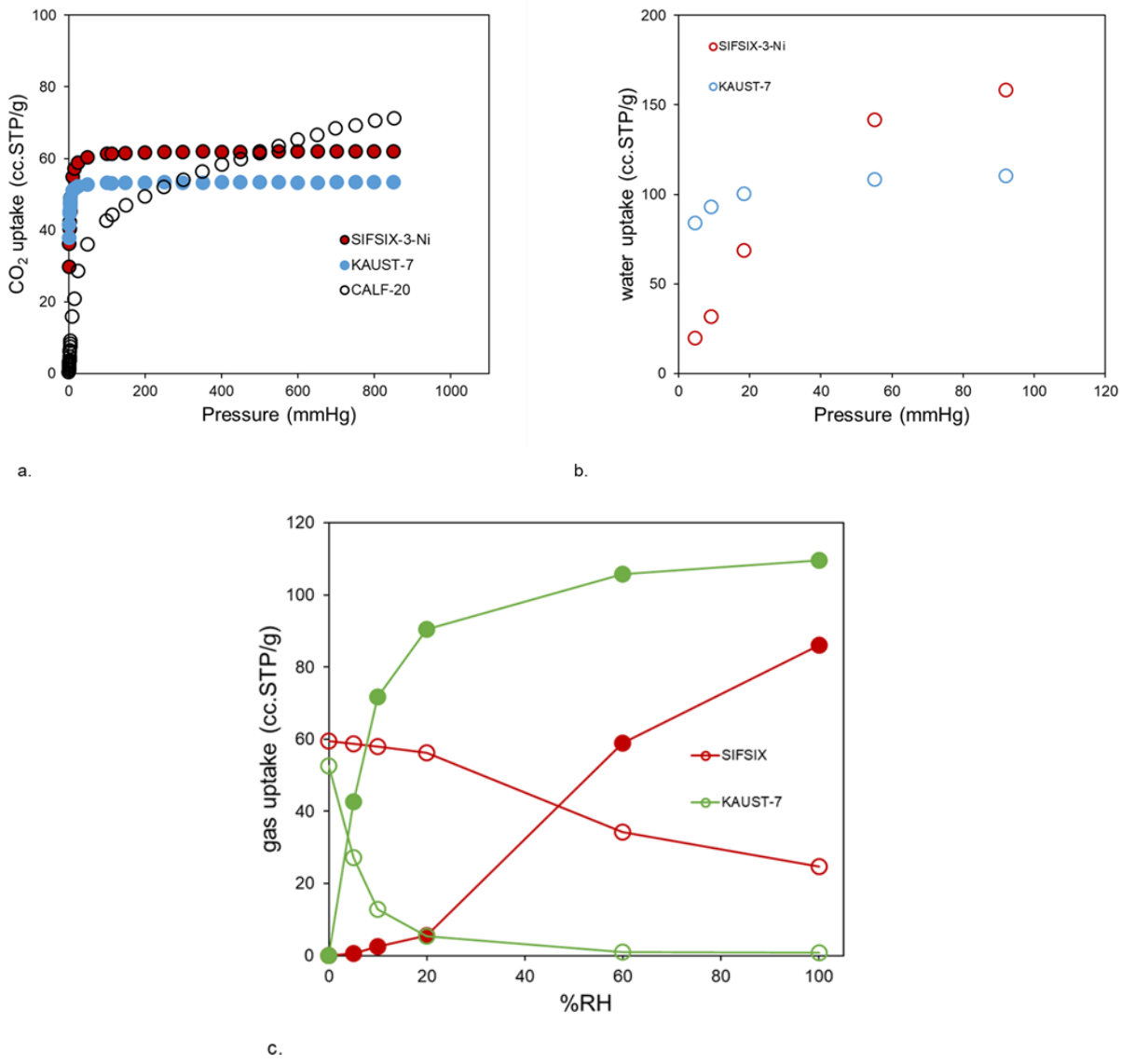

Figure 5.8. ***a.*** *Simulated CO_2 adsorption isotherms for SIFSIX-3-Ni and KAUST-7 at 323 K compared with CALF-20.* ***b.*** *Simulated water adsorption isotherms at 323 K.* ***c.*** *Simulated binary CO_2-water adsorption isotherms at 323 K and 4% P_{CO2} and different relative humidity values; the open symbol corresponds to CO_2 uptake, while the closed symbol represent water uptake.*

5.3. Computational Methodology

5.3.1. Force Fields (FF) Model

The non-bonded interactions between atoms in the framework and the adsorbates were described using a Lennard-Jones (LJ) potential combined with a Coulomb potential as shown in eq. (1)

$$V_{ij} = 4\varepsilon_{ij}\left[\left(\frac{\sigma_{ij}}{r_{ij}}\right)^{12} - \left(\frac{\sigma_{ij}}{r_{ij}}\right)^{6}\right] + \frac{q_i q_j}{4\pi\epsilon_0 r_{ij}}$$

where i and j correspond to the interacting atoms, r_{ij} is the distance between atoms i and j, q_i and q_j are the partial atomic charges on atoms i and j, ε and σ are the LJ parameters, and ε_0 is the vacuum permittivity constant. The parameters for the framework atoms, specifically ε and σ, were taken from Dreiding Force Fields (DFF).[36] The LJ parameters for adsorbate molecules, CO_2 and H_2O, were obtained from the TraPPE FF[37] and TiP4P-Ew,[38] respectively. The Lorentz-Berthelot mixing rules were employed to calculate the LJ parameters for various atom types. The interactions involving LJ (Lennard-Jones) potential were truncated at a distance of 12.8 Å. The Ewald submission method was employed to calculate the cumulative effects of atomic partial charges, specifically the long-range electrostatic interactions. The partial charges of framework atoms were calculated by DDEC method. During the simulations, the positions of all atoms in the MOFs were kept constant.

5.3.2. Screening Procedure

In-silico screening of already-synthesized MOFs from published database was performed with a multi-step simulations approach to identify outstanding materials for CO_2 capture. A detailed structure-property relationships and optimal adsorbents were then identified using industrial-represented metrics include CO_2/H_2O Henry's constants, adsorption capacity and selectivity, as well as isosteric heat of adsorption (Qst): all obtained through Monte Carlo simulations of adsorption at relevant operating conditions. These metrics were benchmarked against identified top materials for this application so far, CALF-20.

The initial screening was conducted with respect to structures having Pore Limiting Diameter (PLD) values of > 2.0 Å, to take into account materials even with ultramicropores, and consider potential structural flexibility in certain materials: we note that the kinetic diameter of CO_2 is ca. 3.3 Å. This criterion in initial screening allowed for pre-selection of ~7,800 structures (out of ~20,000 structures) from the QMOF database. This subset was then

complemented with 2,932 MOFs from the CoRE/DDEC MOF database for further simulations. This mainly because all of MOFs contained in the CoRE/DDEC MOF database are porous - having PLD > 2.0 Å. For the total of ca. 10,732 structures, we first calculated the Henry's constant (K_H) at 323 K through the Widom insertion method.[26] CO_2 and H_2O K_H calculations indicate the affinity of MOFs towards each adsorbate at low-pressure regimes and can be used as a useful metric to identify CO_2-selective materials and eliminate hydrophilic structures to avoid competitive adsorption of water, the structures whose w ater K_H values are higher than that of CALF-20 (K_H H_2O in CALF-20: 5.6 X 10^{-5} mol/kg.Pa). After the K_H screening, we calculated the amount of CO_2 adsorbed in all 10,732 MOFs at 323 K and two sets of industry-relevant operating pressures of 30.4 mmHg and 114 mmHg using the grand canonical Monte Carlo (GCMC) simulation technique as implemented in the RASPA code.[39] To identify promising materials, we looked into structures with CO_2 uptake higher than 22.4 cc/g, and 11 cc/g at 114 mmHg and 30.4 mmHg, respectively. These values correspond to the CO_2 uptake in activated carbons at the similar operating conditions. CO_2-selective materials are selected based on the value of K_H CO_2/K_H H_2O > 1. The use of Henry's constant for determining these structures may valid since the operating pressures for screening process are at low pressure regimes. For the top candidates we identified through high-throughput computational screening, CO_2 adsorption isotherms for a range of pressures from 0 – 800 mmHg were calculated. This protocol is conducted for both MOF databases and the results is presented separately for each database. Some structures may overlap each other, nevertheless this is beyond the scope of this work to perform the analysis on how database selection affect the assessment of CO_2 adsorption on potential MOFs.

To conduct a more comprehensive examination of the hydrophobic characteristics of MOFs, a simulations of water adsorption isotherms were performed at a specific temperature of 323 K and at varied relative humidities of 5%, 10%, 20% and 60% for the CO_2-selective MOF candidates which is equal to water partial pressure of 613, 1226, 2452, and 7356 Pa, respectively. For this study, the experimental saturation pressure of 12260 Pa at 323 K was used for relative humidities calculation. The generation of comprehensive adsorption isotherms for water is of significance as it enables the precise identification of the pressure at which condensation takes place and the initiation of water filling within the pores. The main aim of this study is to screen MOFs for CO_2 capture in the presence of humidity. To account for competitive adsorption of water, after performing GCMC simulations for pure-component CO_2 and water, we then performed GCMC simulations for the binary CO2/H2O adsorption

isotherms at 4% P_{CO2}, while changing the relative humidity to 5%, 10%, 20%, and 60%, i.e water partial pressures of 613 Pa, 1226 Pa, 2452 Pa, and 7356 Pa, respectively.

5.4. Conclusion

Competitive co-adsorption of water is a major problem in the deployment of adsorption-based CO_2 capture. Water molecules may compete for adsorption sites, reducing the capacity of the material. Therefore, development of materials that can selectively adsorb CO_2 in the presence of water would be a major step forward in the deployment of CO_2 capture adsorbents in practical settings. Here, we perform large-scale computational screening to look for MOFs with high capacity of CO_2 and high selectivity toward CO_2 over H_2O. We screen two databases, the QMOF and the CoRE MOF database consisting of ca. 10,000 porous structures in search for suitable candidates for CO_2 capture at 114 mmHg and lower pressure of 30.4 mmHg at 323 K. We first identify MOFs with high CO_2/H_2O selectivities based on the ratio of Henry's constants. We then identify MOFs with hydrophobic characteristics by benchmarking against CALF-20's water Henry's constant. The adsorption characteristics of the top MOFs are then calculated using GCMC simulations. Binary mixture simulations of selected top-performing MOFs show that our strategy works very well to find MOFs with high CO_2/H_2O selectivities and the identification of hydrophobic MOFs. Our results further show that high CO_2 capacity and high CO_2/H_2O selectivity originates from strong van der Waals interaction between pore walls and CO_2 molecules in structures with pore sizes of less than 6 Å. Using the computational approach that we develop here, we identify a number of MOF candidates with high CO_2 uptake, even higher than that of CALF-20. Yet, for some of these structures, high interaction with water is observed and therefore reduce CO_2 uptake capacity. We also identify a number of MOFs such as HIVPIO, YUGZEG, SACWEB and ABAVIJ exhibiting high CO_2 uptake with and without the presence of water. These top-performing materials are further suggested to our collaborator's experimental teams for further analysis and testing in the lab. Furthermore, we also study a number of anionic fluorinated MOFs with promising performance metrics for post-combustion CO_2 capture processes, but these structures are predicted to be hydrophilic. This work clearly demonstrates the important role that molecular simulations can guide experimentalist to identify promising materials in a quick and efficient manner. Future computational work can focus on the identification of hydrothermally stable MOFs as well as developing and designing hydrophobic MOFs with high CO_2 working capacity. While molecular-level calculations are useful for high-throughput calculations, they are not usually accurate for predicting particular guest-host interactions for example water adsorption on MOFs' unsaturated metal sites, and/or stability via bond formation, bond breakage. From the experimental point of view, future computational approaches should focus on incorporating the

MOFs stability, such as thermal, chemical and mechanical. Computational screening efforts should also involve the relevant industry operating condition for the identification of top-performing MOFs for particular application.

References

(1) Boyd, P. G.; Chidambaram, A.; García-Díez, E.; Ireland, C. P.; Daff, T. D.; Bounds, R.; Gładysiak, A.; Schouwink, P.; Moosavi, S. M.; Maroto-Valer, M. M.; Reimer, J. A.; Navarro, J. A. R.; Woo, T. K.; Garcia, S.; Stylianou, K. C.; Smit, B. Data-Driven Design of Metal–Organic Frameworks for Wet Flue Gas CO_2 Capture. *Nature* **2019**, *576* (7786), 253–256. https://doi.org/10.1038/s41586-019-1798-7.

(2) Benoit, V.; Chanut, N.; Pillai, R. S.; Benzaqui, M.; Beurroies, I.; Devautour-Vinot, S.; Serre, C.; Steunou, N.; Maurin, G.; Llewellyn, P. L. A Promising Metal–Organic Framework (MOF), MIL-96(Al), for CO_2 Separation under Humid Conditions. *J. Mater. Chem. A* **2018**, *6* (5), 2081–2090. https://doi.org/10.1039/C7TA09696H.

(3) Mason, J. A.; McDonald, T. M.; Bae, T.-H.; Bachman, J. E.; Sumida, K.; Dutton, J. J.; Kaye, S. S.; Long, J. R. Application of a High-Throughput Analyzer in Evaluating Solid Adsorbents for Post-Combustion Carbon Capture via Multicomponent Adsorption of CO_2, N_2, and H_2O. *J. Am. Chem. Soc.* **2015**, *137* (14), 4787–4803. https://doi.org/10.1021/jacs.5b00838.

(4) Kim, E. J.; Siegelman, R. L.; Jiang, H. Z. H.; Forse, A. C.; Lee, J.-H.; Martell, J. D.; Milner, P. J.; Falkowski, J. M.; Neaton, J. B.; Reimer, J. A.; Weston, S. C.; Long, J. R. Cooperative Carbon Capture and Steam Regeneration with Tetraamine-Appended Metal–Organic Frameworks. *Science.* **2020**, *369* (6502), 392–396. https://doi.org/10.1126/science.abb3976.

(5) Moghadam, P. Z.; Li, A.; Liu, X.-W.; Bueno-Perez, R.; Wang, S.-D.; Wiggin, S. B.; Wood, P. A.; Fairen-Jimenez, D. Targeted Classification of Metal–Organic Frameworks in the Cambridge Structural Database (CSD). *Chem. Sci.* **2020**, *11* (32), 8373–8387. https://doi.org/10.1039/D0SC01297A.

(6) Moghadam, P. Z.; Li, A.; Wiggin, S. B.; Tao, A.; Maloney, A. G. P.; Wood, P. A.; Ward, S. C.; Fairen-Jimenez, D. Development of a Cambridge Structural Database Subset: A Collection of Metal–Organic Frameworks for Past, Present, and Future. *Chem. Mater.* **2017**, *29* (7), 2618–2625. https://doi.org/10.1021/acs.chemmater.7b00441.

(7) Silva, P.; Vilela, S. M. F.; Tomé, J. P. C.; Almeida Paz, F. A. Multifunctional Metal–Organic Frameworks: From Academia to Industrial Applications. *Chem. Soc. Rev.* **2015**, *44* (19), 6774–6803. https://doi.org/10.1039/C5CS00307E.

(8) Czaja, A. U.; Trukhan, N.; Müller, U. Industrial Applications of Metal–Organic Frameworks. *Chem. Soc. Rev.* **2009**, *38* (5), 1284. https://doi.org/10.1039/b804680h.

(9) Freund, R.; Zaremba, O.; Arnauts, G.; Ameloot, R.; Skorupskii, G.; Dincă, M.; Bavykina, A.; Gascon, J.; Ejsmont, A.; Goscianska, J.; Kalmutzki, M.; Lächelt, U.; Ploetz, E.; Diercks, C. S.; Wuttke, S. The Current Status of MOF and COF Applications. *Angew. Chemie Int. Ed.* **2021**, *60* (45), 23975–24001. https://doi.org/https://doi.org/10.1002/anie.202106259.

(10) Shimizu, G. K. H.; Vaidhyanathan, R.; Iremonger, S. S.; Deakin, K.; Lin, J.-B.; Dawson, K. W. Metal Organic Framework, Production and Use Thereof. WO2014138878A1, 2014.

(11) Hovington, P.; Ghaffari-Nik, O.; Mariac, L.; Liu, A.; Henkel, B.; Marx, S. Rapid Cycle Temperature Swing Adsorption Process Using Solid Structured Sorbent for CO_2 Capture from Cement Flue Gas. In *Proceedings of the 15th Greenhouse Gas Control Technologies Conference 15-18 March 2021*; 2021; pp 1–11. https://doi.org/10.2139/ssrn.3814414.

(12) Lin, J.-B.; Nguyen, T. T. T.; Vaidhyanathan, R.; Burner, J.; Taylor, J. M.; Durekova, H.; Akhtar, F.; Mah, R. K.; Ghaffari-Nik, O.; Marx, S.; Fylstra, N.; Iremonger, S. S.; Dawson, K. W.; Sarkar, P.; Hovington, P.; Rajendran, A.; Woo, T. K.; Shimizu, G. K. H. A Scalable Metal-Organic Framework as a Durable Physisorbent for Carbon Dioxide Capture. *Science.* **2021**, *374* (6574), 1464–1469. https://doi.org/10.1126/science.abi7281.

(13) Ho, C.-H.; Paesani, F. Elucidating the Competitive Adsorption of H_2O and CO_2 in CALF-20: New Insights for Enhanced Carbon Capture Metal–Organic Frameworks. *ACS Appl. Mater. Interfaces* **2023**, *15* (41), 48287–48295. https://doi.org/10.1021/acsami.3c11092.

(14) Magnin, Y.; Dirand, E.; Maurin, G.; Llewellyn, P. L. Abnormal CO_2 and H_2O Diffusion in CALF-20(Zn) Metal–Organic Framework: Fundamental Understanding of CO2 Capture. *ACS Appl. Nano Mater.* **2023**, *6* (21), 19963–19971. https://doi.org/10.1021/acsanm.3c03752.

(15) Chen, Z.; Ho, C.-H.; Wang, X.; Vornholt, S. M.; Rayder, T. M.; Islamoglu, T.; Farha, O. K.; Paesani, F.; Chapman, K. W. Humidity-Responsive Polymorphism in CALF-20: A Resilient MOF Physisorbent for CO2 Capture. *ACS Mater. Lett.* **2023**, *5* (11), 2942–2947. https://doi.org/10.1021/acsmaterialslett.3c00930.

(16) Li, S.; Chung, Y. G.; Snurr, R. Q. High-Throughput Screening of Metal-Organic Frameworks for CO_2 Capture in the Presence of Water. *Langmuir* **2016**. https://doi.org/10.1021/acs.langmuir.6b02803.

(17) Moghadam, P. Z.; Chung, Y. G.; Snurr, R. Q. Progress toward the Computational Discovery of New Metal–Organic Framework Adsorbents for Energy Applications. *Nat. Energy* **2024**, *9* (2), 121–133. https://doi.org/10.1038/s41560-023-01417-2.

(18) Nandy, A.; Duan, C.; Kulik, H. J. Using Machine Learning and Data Mining to Leverage Community Knowledge for the Engineering of Stable Metal–Organic Frameworks. *J. Am. Chem. Soc.* **2021**, *143* (42), 17535–17547. https://doi.org/10.1021/jacs.1c07217.

(19) Leperi, K. T.; Chung, Y. G.; You, F.; Snurr, R. Q. Development of a General Evaluation Metric for Rapid Screening of Adsorbent Materials for Postcombustion CO_2 Capture. *ACS Sustain. Chem. Eng.* **2019**, *7* (13), 11529–11539. https://doi.org/10.1021/acssuschemeng.9b01418.

(20) Farmahini, A. H.; Krishnamurthy, S.; Friedrich, D.; Brandani, S.; Sarkisov, L. Performance-Based Screening of Porous Materials for Carbon Capture. *Chem. Rev.* **2021**, *121* (17), 10666–10741. https://doi.org/10.1021/acs.chemrev.0c01266.

(21) Anderson, R.; Gómez-Gualdrón, D. A. Large-Scale Free Energy Calculations on a Computational Metal–Organic Frameworks Database: Toward Synthetic Likelihood Predictions. *Chem. Mater.* **2020**, *32* (19), 8106–8119. https://doi.org/10.1021/acs.chemmater.0c00744.

(22) Moghadam, P. Z.; Rogge, S. M. J.; Li, A.; Chow, C.-M.; Wieme, J.; Moharrami, N.; Aragones-Anglada, M.; Conduit, G.; Gomez-Gualdron, D. A.; Van Speybroeck, V.; Fairen-Jimenez, D. Structure-Mechanical Stability Relations of Metal-Organic Frameworks via Machine Learning. *Matter* **2019**, *1* (1), 219–234. https://doi.org/10.1016/j.matt.2019.03.002.

(23) Healy, C.; Patil, K. M.; Wilson, B. H.; Hermanspahn, L.; Harvey-Reid, N. C.; Howard, B. I.; Kleinjan, C.; Kolien, J.; Payet, F.; Telfer, S. G.; Kruger, P. E.; Bennett, T. D. The Thermal Stability of Metal-Organic Frameworks. *Coord. Chem. Rev.* **2020**, *419*, 213388. https://doi.org/https://doi.org/10.1016/j.ccr.2020.213388.

(24) Rosen, A. S.; Iyer, S. M.; Ray, D.; Yao, Z.; Aspuru-Guzik, A.; Gagliardi, L.; Notestein, J. M.; Snurr, R. Q. Machine Learning the Quantum-Chemical Properties of Metal–Organic Frameworks for Accelerated Materials Discovery. *Matter* **2021**, *4* (5), 1578–1597. https://doi.org/10.1016/j.matt.2021.02.015.

(25) Chung, Y. G.; Camp, J.; Haranczyk, M.; Sikora, B. J.; Bury, W.; Krungleviciute, V.; Yildirim, T.; Farha, O. K.; Sholl, D. S.; Snurr, R. Q. Computation-Ready, Experimental

Metal–Organic Frameworks: A Tool To Enable High-Throughput Screening of Nanoporous Crystals. *Chem. Mater.* **2014**, *26* (21), 6185–6192. https://doi.org/10.1021/cm502594j.

(26) Moghadam, P. Z.; Fairen-Jimenez, D.; Snurr, R. Q. Efficient Identification of Hydrophobic MOFs: Application in the Capture of Toxic Industrial Chemicals. *J. Mater. Chem. A* **2016**, *4* (2), 529–536. https://doi.org/10.1039/C5TA06472D.

(27) Takaishi, S.; Hosoda, M.; Kajiwara, T.; Miyasaka, H.; Yamashita, M.; Nakanishi, Y.; Kitagawa, Y.; Yamaguchi, K.; Kobayashi, A.; Kitagawa, H. Electroconductive Porous Coordination Polymer $Cu[Cu(Pdt)_2]$ Composed of Donor and Acceptor Building Units. *Inorg. Chem.* **2009**, *48* (19), 9048–9050. https://doi.org/10.1021/ic802117q.

(28) Rad, M.; Dehghanpour, S.; Fatehfard, S.; Gholamrezazadeh, C.; Mahmoudi, A. Discrete Molecular Complex, One and Two Dimensional Coordination Polymer from Cobalt, Copper, Zinc and (E)-4-Hydroxy-3-((Quinolin-8-Ylimino)Methyl)Benzoic Acid: Synthesis, Structures and Gas Sensing Property. *Polyhedron* **2016**, *106*, 10–17. https://doi.org/10.1016/j.poly.2015.12.020.

(29) Aubrey, M. L.; Kapelewski, M. T.; Melville, J. F.; Oktawiec, J.; Presti, D.; Gagliardi, L.; Long, J. R. Chemiresistive Detection of Gaseous Hydrocarbons and Interrogation of Charge Transport in $Cu[Ni(2,3\text{-Pyrazinedithiolate})_2]$ by Gas Adsorption. *J. Am. Chem. Soc.* **2019**, *141* (12), 5005–5013. https://doi.org/10.1021/jacs.9b00654.

(30) Volkringer, C.; Loiseau, T.; Haouas, M.; Taulelle, F.; Popov, D.; Burghammer, M.; Riekel, C.; Zlotea, C.; Cuevas, F.; Latroche, M.; Phanon, D.; Knöfelv, C.; Llewellyn, P. L.; Férey, G. Occurrence of Uncommon Infinite Chains Consisting of Edge-Sharing Octahedra in a Porous Metal Organic Framework-Type Aluminum Pyromellitate $Al_4(OH)_8[C_{10}O_8H_2]$ (MIL-120): Synthesis, Structure, and Gas Sorption Properties. *Chem. Mater.* **2009**, *21* (24), 5783–5791. https://doi.org/10.1021/cm9023106.

(31) Uemura, K.; Maeda, A.; Maji, T. K.; Kanoo, P.; Kita, H. Syntheses, Crystal Structures and Adsorption Properties of Ultramicroporous Coordination Polymers Constructed from Hexafluorosilicate Ions and Pyrazine. *Eur. J. Inorg. Chem.* **2009**, *2009* (16), 2329–2337. https://doi.org/10.1002/ejic.200900144.

(32) Moghadam, P. Z.; Ivy, J. F.; Arvapally, R. K.; dos Santos, A. M.; Pearson, J. C.; Zhang, L.; Tylianakis, E.; Ghosh, P.; Oswald, I. W. H.; Kaipa, U.; Wang, X.; Wilson, A. K.; Snurr, R. Q.; Omary, M. A. Adsorption and Molecular Siting of CO_2, Water, and Other Gases in the Superhydrophobic, Flexible Pores of FMOF-1 from Experiment and Simulation. *Chem. Sci.* **2017**, *8* (5), 3989–4000. https://doi.org/10.1039/C7SC00278E.

(33) Elsaidi, S. K.; Mohamed, M. H.; Simon, C. M.; Braun, E.; Pham, T.; Forrest, K. A.; Xu, W.; Banerjee, D.; Space, B.; Zaworotko, M. J.; Thallapally, P. K. Effect of Ring Rotation upon Gas Adsorption in SIFSIX-3-M (M = Fe, Ni) Pillared Square Grid Networks. *Chem. Sci.* **2017**, *8* (3), 2373–2380. https://doi.org/10.1039/C6SC05012C.

(34) Cadiau, A.; Adil, K.; Bhatt, P. M.; Belmabkhout, Y.; Eddaoudi, M. A Metal-Organic Framework–Based Splitter for Separating Propylene from Propane. *Science.* **2016**, *353* (6295), 137–140. https://doi.org/10.1126/science.aaf6323.

(35) Antypov, D.; Shkurenko, A.; Bhatt, P. M.; Belmabkhout, Y.; Adil, K.; Cadiau, A.; Suyetin, M.; Eddaoudi, M.; Rosseinsky, M. J.; Dyer, M. S. Differential Guest Location by Host Dynamics Enhances Propylene/Propane Separation in a Metal-Organic Framework. *Nat. Commun.* **2020**, *11* (1), 6099. https://doi.org/10.1038/s41467-020-19207-9.

(36) Mayo, S. L.; Olafson, B. D.; Goddard, W. A. DREIDING: A Generic Force Field for Molecular Simulations. *J. Phys. Chem.* **1990**, *94* (26), 8897–8909. https://doi.org/10.1021/j100389a010.

(37) Potoff, J. J.; Siepmann, J. I. Vapor–Liquid Equilibria of Mixtures Containing Alkanes, Carbon Dioxide, and Nitrogen. *AIChE J.* **2001**, *47* (7), 1676–1682. https://doi.org/10.1002/aic.690470719.

(38) Vega, C.; Abascal, J. L. F.; Nezbeda, I. Vapor-Liquid Equilibria from the Triple Point up to the Critical Point for the New Generation of TIP4P-like Models: TIP4P/Ew, TIP4P/2005, and TIP4P/Ice. *J. Chem. Phys.* **2006**, *125* (3), 34503. https://doi.org/10.1063/1.2215612.

(39) Dubbeldam, D.; Calero, S.; Ellis, D. E.; Snurr, R. Q. RASPA: Molecular Simulation Software for Adsorption and Diffusion in Flexible Nanoporous Materials. *Mol. Simul.* **2016**, *42* (2), 81–101. https://doi.org/10.1080/08927022.2015.1010082.

6. Conclusion and Research Outlook

6.1. Conclusion

Metal-organic frameworks (MOFs) have emerged as a significant advancement in the field of porous materials science. They are currently gaining considerable attention due to their successful integration into industrial applications, particularly for gas storage and separation purposes, including the capture of CO_2 from flue gas. Here, we successfully perform a multi-scale computational strategy that covered density functional theory (DFT) and grand canonical Monte Carlo (GCMC) simulations to simulate CO_2 adsorption in MOFs that were already synthesised and reported in the literature. We identify top-performing structures for selective CO_2 adsorption from a wet flue gas mixture. In Chapter 3, we dedicate the first screening study to derive structure–property relationships for CO_2 adsorption in Zr-oxide MOFs. We find MOF materials with heat of adsorption values over 25 kJ/mol and cavity diameter of approximately 6-7 Å exhibit the highest CO_2 adsorption. In Chapter 4, our computational simulations are focused on understanding the gas adsorption properties and framework flexibility of CALF-20 using molecular simulation and experimental techniques. The discrepancy between the predicted and experimental value of CO_2 adsorption, particularly at a temperature of 273 K, indicates the occurrence of structural flexibility in the presence of gas molecules. Therefore, CALF-20's framework flexibility is further investigated by combining experimental gas adsorption and PXRD data with molecular dynamics simulations at the DFT level. These techniques provide evidence that the presence of adsorbed guests significantly expands the available pore space, supporting the concept that the discrepancy between the experimental results and the Monte Carlo simulations. Furthermore, with the aid of molecular simulations, supported by experimental data, the hydrophobic nature of CALF-20 is investigated showing that water molecules prefer occupying the small pores rather than directly interacting with the Zn atoms. We anticipate that this work will stimulate the advancement of further MOF materials that are beneficial for capturing CO_2 in humid environments. Chapter 5 reports screening of the the Quantum MOF (QMOF) database and the Computation-Ready, Experimental (CoRE) MOF database for selective adsorption of CO_2 from a wet flue gas mixture. Following the first screening process that relies on the geometric characteristics of MOFs, about 10,000 porous MOFs are selected for extensive simulations to study the adsorption of CO_2 and H_2O. The next step of the simulations is then focused on the single components of CO_2 and H_2O, as well as the combined CO_2-H_2O simulations. The screening

technique effectively reveals several interesting MOFs that exhibit selectivity towards CO_2 in the presence of water vapour. By establishing a close and efficient cycle of simulations and tests conducted by our industrial partner, we have been able to effectively synthesize and evaluate several MOFs in the laboratory. This process confirms the effectiveness of our strategy in selecting exceptional MOFs for the purpose of CO_2 capture process.

6.2. Research Outlook

Although significant advancements have been made, it is important to acknowledge the various constraints present in the current computational screening investigations. It is assumed that MOFs are stable under the conditions required for CO_2 capture and separation. This assumption may not hold universally, as many MOFs exhibit chemical and thermal instability, especially when exposed to moisture or subjected to high-temperature separation conditions. A thorough comprehension of the chemical and thermal stability of MOFs is essential to offer recommendations for choosing appropriate building blocks to create stable MOFs for adsorption applications. There is a lack of comprehensive research on this subject. In this thesis, the majority of the computational screening efforts has been focused on the analysis of the material properties, specifically the adsorption capacity and selectivity. To achieve energy efficiency and cost-effectiveness in separation processes, it is crucial to combine process requirements with material attributes at industrial scale. Hence, it is imperative to integrate multiscale molecular simulation and process optimisation to comprehensively evaluate and select the most suitable MOFs for achieving optimal system performance. The existing screening tests have certain constraints that need to be addressed to forward computational efforts in developing optimal MOFs for efficient CO_2 capture and separation. Finally, we believe that the evaluation of synthesisability and techno-economics should be conducted in conjunction with the screening (and design) process. Hence, by integrating the screening protocols and collaborations with experimentalist or industrialist, we can improve the speed for evaluating and testing novel materials for energy applications.